RICE UNIVERSITY

Iron Sulfide Precipitation Kinetics, Solubility, Phase Transformation, and Corrosion versus Temperature and Ionic Strength

by

Ya Liu

A THESIS SUBMITTED IN PARTIAL FULFILLMENT

OF THE REQUIREMENTS FOR THE DEGREE

Doctor of Philosophy

APPROVED, THESIS COMMITTEE

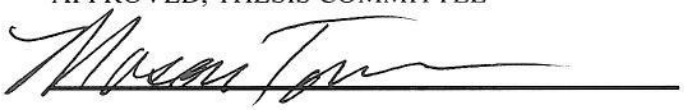

Mason B. Tomson, Chair, Professor

Civil & Environmental Engineering

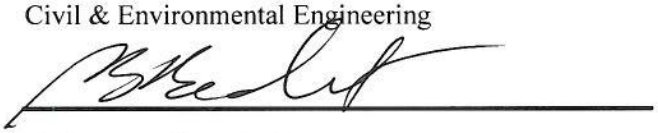

Philip B. Bedient, Professor

Civil & Environmental Engineering

Walter G. Chapman, Professor

Chemical & Biomolecular Engineering

HOUSTON, TEXAS

April 12th, 2017

Abstract

Iron Sulfide Precipitation Kinetics, Solubility, Phase Transformation, and Corrosion versus Temperature and Ionic Strength

by

Ya Liu

A reliable anoxic plug flow reactor has been developed to study iron sulfide (FeS) precipitation kinetics, solubility, phase transformation, and corrosion simultaneously. The effects of temperature (23 – 125 °C), ionic strength (0.00886 – 5.03 mol/kg), and ferrous iron (Fe(II)) to sulfide (S(-II)) concentration ratio (1:20 to 1:5) were studied. The kinetics of FeS precipitation was found to be a pseudo first order reaction with respect to Fe(II) concentration, when Fe(II) concentration is significantly lower than S(-II) concentration. FeS precipitation kinetics can be accelerated by high temperature and high ionic strength, but not be affected by Fe(II) to S(-II) concentration ratio at the tested ratio range. A model for predicting FeS solubility and precipitation was developed by using FeS solubility data measured in this study and data from literature. At temperature ≤ 100 °C, freshly precipitated FeS was found to be mackinawite. Mackinawite can transform to troilite at temperature ≥ 50 °C, and low ionic strength favors the phase transformation. Also, mackinawite formed from steel corrosion seems to be easier to transform to troilite than the mackinawite formed from precipitation. H_2S corrosion and FeS scale retention on carbon steel can be significantly accelerated by high temperature and impeded by extra high ionic strength (IS ≥ 4 mol/kg). This study presented a new approach for iron sulfide study and contributed valuable FeS thermodynamics and kinetics data for FeS prediction and control in industry.

Acknowledgments

It is with immense gratitude that I acknowledge the support and help of my adviser, friends and families during the whole research project. I wish to thank, first and foremost, Dr. Mason Tomson, my adviser, and Dr. Amy Kan for their valuable advice and support. They not only taught me rational thinking but also gave me precious advice and suggestions when I confronted troubles in research. Their help is greatly appreciated.

Second, I am indebted to my many friends in the lab. Postdocs, Dr. Fei Yan, Dr. Fangfu Zhang, Dr. Narayan Bhandari and Dr. Gedeng Ruan, and visiting scholar, Dr. Hamad Al-Saiari, gave me many helpful suggestions to overcome difficulties in both research and study. And many thanks to other lab members, Zhang Zhang, Zhaoyi Dai, Alex Lu, Guannan Deng, and Sue Wang for their constant support and encouragement.

Last but not least, I want to thank my beloved families, especially my parents, for their immeasurable support and love.

For financial support, I thank Brine Chemistry Consortium of Rice University and the China Scholarship Council.

This study would not have been possible without all the help and support from my advisor, friends, family and sponsors. Great thanks to all of you.

Contents

List of Figures

List of Tables

Nomenclature

CR: corrosion rate.

$\left[Fe(II)\right]_0$: the initial Fe(II) concentration of the influent before reacting with S(-II)

$\left[Fe(II)\right]_Q$: the remaining Fe(II) concentration in the effluent at flow rate Q

$\left[Fe(II)\right]_{eq.}$: the Fe(II) concentration of effluent that is at equilibrium with precipitated FeS solid

$\left[Fe(II)\right]_t$: the remaining Fe(II) concentration in the effluent at reaction time t

FeS: iron sulfide

GC C1018: glass column reactor with C1018 coupons inside

GC HC-276 and C1018: glass column reactor with a HC-276 coupon followed by a C1018 coupon inside

HC-276: hastelloy C-276 alloy

IS: ionic strength

k_{1st}: first order reaction rate constant

k_{2nd}: second order reaction rate constant

K_a: acid dissociation constant

k_m: mass transfer coefficient

K_{sp}: solubility product

Q: flow rate

$\left[S(-II)\right]_0$: the initial S(-II) concentration of the influent before reacting with Fe(II)

SI: saturation index

SR: scale retention rate

SSP: ScaleSoftPitzer software

TF: Troilite fraction

γ: activity coefficient

Chapter 1. Introduction

1.1 Problem statement

Iron sulfide scale is ubiquitous in many operation systems in industry, such as oil and gas production and refinery, water and wastewater treatment, sewer transportation pipes, and any metal equipment corroded by hydrogen sulfide (H_2S). Iron sulfide formation is often due to H_2S corrosion on steel or sulfide (S(-II)) reacting with ferrous ions (Fe(II)). Due to the low solubility and fast precipitation kinetics, iron sulfide forms easily. The solubility of the most soluble stable iron sulfide phase (called mackinawite) is five orders of magnitude lower than the solubility of calcite ($CaCO_3$) (Dai 2017; Rickard 2007). Iron sulfide deposition on transportation pipes can not only reduce transportation efficiency but also accelerate further corrosion to pipes and threaten asset integrity (Wylde 2014). Asset integrity failure caused by H_2S corrosion can lead to severe environmental contaminations, such as oil or gas leaking and H_2S emission. Iron sulfide formation on metal equipment (e.g. pumps and valves) can cause equipment malfunction (Wylde 2014). Also, in oil industry, iron sulfide is oil wet and can cause oil-water emulsions, leading to operational problems and severely impairing oil quality (Wylde 2014).

Furthermore, H_2S is always a safety concern. Prolonged exposure to 2 – 5 ppm H_2S could cause nausea, tearing of the eyes, headaches, or loss of sleep. 2 – 15 minutes exposure to 100 ppm H_2S can result in coughing, eye irritation, and loss of smell. Exposure to 1000 ppm H_2S can cause rapid unconsciousness or nearly instant death (OSHA 2005).

For common mineral scales, such as calcite ($CaCO_3$), barite ($BaSO_4$), gypsum ($CaSO_4$), and anhydrite ($CaSO_4$), many chemicals (called scale inhibitors) can effectively inhibit or delay scale

formation, so that scale caused problems can be relieved to some extent. However, as far as we know, no effective iron sulfide scale inhibitor has been found.

Despite so many severe problems caused by iron sulfide, it has not been well understood due to the complexity of iron sulfide chemistry and the requirement of anoxic experimental condition. To solve iron sulfide problems, first it is necessary to study the thermodynamics and kinetics of iron sulfide, and build a iron sulfide prediction model. Also, it is essential to find chemicals that can effectively inhibit iron sulfide formation and/or deposition.

1.2 Research objectives

Despite the ubiquitous existence of iron sulfide, iron sulfide has not been well understood because of its complex chemistry and the need of rigorous anoxic experimental condition. This study has the following research goals, and they can be achieved in one experiment setup. Different operational and solution conditions were tested, including temperature, ionic strength (IS), and Fe(II) to S(-II) concentration ratios.

1. Iron sulfide solubility.
2. Iron sulfide precipitation kinetics.
3. Iron sulfide phase transformation.
4. Iron sulfide scale retention on metal steels.
5. Hydrogen sulfide (H_2S) corrosion on metal steels.

Chapter 2, Background and Literature Review, introduces Fe^{2+} and H_2S chemistry, properties of different iron sulfide phases, and iron sulfide in the oil field. Chapter 3 gives a full description of experimental methods. Chapter 4 presents results and discussions. Chapter 5 concludes the results. The references and my curriculum vitae are attached at the end.

Chapter 2. Background and Literature Review

2.1. Ferrous ion and hydrogen sulfide chemistry

2.1.1. Ferrous chemistry in aqueous solution

2.1.1.1. Reduction potentials of Fe/Fe^{2+} and Fe^{2+}/Fe^{3+}

Iron is the most common element on earth in terms of mass, and the fourth most common element in the crust. Iron has several oxidation states, −2, −1, 0, +1, +2, +3, +4, +5, and +6; while in aqueous solutions, 0, +2 and +3, are most common.

Elemental iron (Fe^0) can be oxidized to ferrous ion (Fe^{2+}) by acid and produce H_2. The standard reduction potential (E^o) and the standard Gibbs free energy ($\Delta_r G_m^o$) of the reaction are shown in equation 2.1 (Lemire 2013).

$$Fe^{2+} + H_2 \rightarrow Fe(\alpha) + 2H^+ \qquad (2.1)$$

$$E^o = -(0.4745 \pm 0.0088)\,V$$
$$\Delta_r G_m^o = 91.56 \pm 1.70\,\mathrm{kJ/mol}$$

"Fe^{2+}" is the conventional way of writing the ferrous ion, but it is actually a shorthand notation of $[Fe(H_2O)_6]^{2+}$. Based on the octahedral geometry of $[Fe(H_2O)_6]^{2+}$, it is known that ferrous ion has coordination number of 6. Ferrous ions can be coordinated by other molecules, if enough space is provided for Fe-OH_2 bonding or similar bonding interaction. For example, EDTA can chelate Fe^{2+} through this mechanism.

Fe^{2+} can be further oxidized to ferric iron (Fe^{3+}) by oxidants, e.g. O_2. equation 2.2 displays this reaction and the corresponding E_0^o and $\Delta_r G_m^o$ (Lemire 2013).

$$Fe^{3+} + 1/2\,H_2 \rightarrow Fe^{2+} + H^+$$
$$E^o = 0.772 \pm 0.002\,V \qquad (2.2)$$
$$\Delta_r G_m^o = -(74.49 \pm 0.19)\,\mathrm{kJ \cdot mol^{-1}}$$

The reduction potential E^o of Fe^{2+} / Fe^{3+} increases linearly with temperature (T (K)), and the slope ($\Delta dE^o/dT$) is about (1.21 ± 0.09) × 10^{-3} V/K (Lemire 2013). The higher the temperature, the easier the oxidation becomes.

Given the above reduction potentials and the anoxic condition in the oil field, dissolved iron in oil produced water is most likely to be in the form of Fe^{2+}.

2.1.1.2. Ferrous hydroxide species

In aqueous solutions, Fe^{2+} can form the following complexes with hydroxide, $Fe(OH)^+$, $Fe(OH)_2^0$, $Fe(OH)_3^-$. The dominate species mainly depends on solution pH and temperature.

$$Fe^{2+} + H_2O \rightarrow Fe(OH)^+ + H^+,\ \beta_1 = \frac{\{Fe(OH)^+\}\{H^+\}}{\{Fe^{2+}\}} \tag{2.3}$$

$$Fe^{2+} + 2H_2O \rightarrow Fe(OH)_{2(aq)} + 2H^+,\ \beta_2 = \frac{\{Fe(OH)_2\}\{H^+\}^2}{\{Fe^{2+}\}} \tag{2.4}$$

$$Fe^{2+} + 3H_2O \rightarrow Fe(OH)_3^- + 3H^+,\ \beta_3 = \frac{\{Fe(OH)_3^-\}\{H^+\}^3}{\{Fe^{2+}\}} \tag{2.5}$$

The stability constants, ß$_1$, ß$_2$ and ß$_3$, have been measured by several studies, but the values vary significantly on different references due to the difficulty in its measurement. In this study, the used stability constants are from Visual Minteq software (version 3.1). The logarithm of ß$_1$, ß$_2$ and ß$_3$ are respectively -9.397, -20.494, and -30.991 at 25°C. These stability constants increase with temperature.

Figure 2.1 shows how ferrous hydroxide species change with pH. The calculation is based on a solution originally containing 0.001 M $FeCl_2$ and 0.001 M HCl, and then it was titrated by 2 M NaOH at 25°C. At low pH, Fe^{2+} is the dominant species. As pH increases to 9.5, $FeOH^+$ becomes dominant, and shortly after that, $Fe(OH)_3^-$ takes over as the dominant species. Note that $Fe(OH)_2^0$ is never the dominant species.

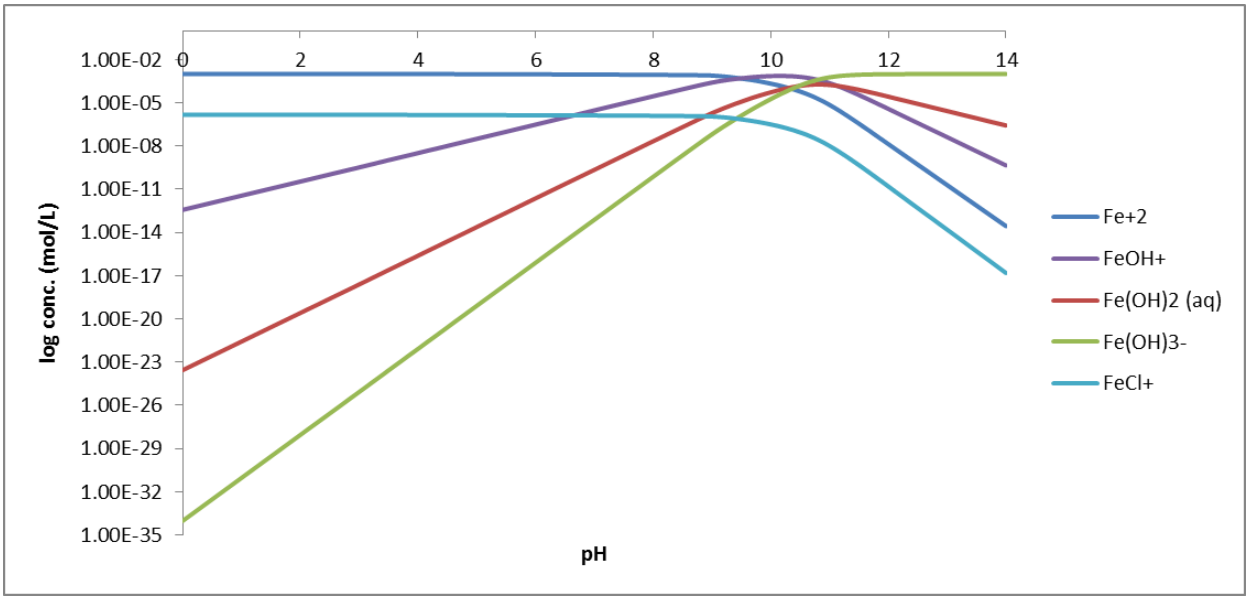

Figure 2.1. Ferrous iron species change with solution pH at T = 25 °C.

2.1.1.3. Ferrous sulfide complexes

Ferrous sulfide complexes are important parts of ferrous complexes in water. There are several proposed ferrous sulfide complexes, including $FeSH^+$, $Fe(SH)_2$, $Fe(SH)_3^-$, and $FeS_{(aq)}$, but their existences are still in debate (Rickard 2007). Based on previous researches and common chemical software, it seems that the existence of $FeSH^+$ is incompatible with $Fe(SH)_2$ and $Fe(SH)_3^-$. For example, software Visual Minteq only considers $FeSH^+$ in ferrous sulfide complexes, while software PHREEQC only considers $Fe(SH)_2$ and $Fe(SH)_3^-$. $FeS_{(aq)}$ was recently

proposed by Rickard (Rickard 2006), and most chemical software have not included this complex yet.

The stability constant of $FeSH^+$ (equation 2.6) at ambient temperature has been measured by several studies.

$$Fe^{2+} + HS^- \rightarrow FeSH^+, \beta = \frac{\{FeSH^+\}}{\{Fe^{2+}\}\{HS^-\}} \quad (2.6)$$

The measured values varied from $10^{4.34}$ to $10^{5.94}$ (Al-Farawati 1999; Luther 1996; Luther III 1993; Wei 1995; Zhang 1994), and their average value is about $10^{5.2}$. In Visual Minteq, $\beta = 10^{5.62}$. However, such high stability constant ($10^{5.2}$) of $FeSH^+$ is inconsistent with mackinawite solubility measurement data (Davison 1999; Rickard 2006). In another words, if $\beta = 10^{5.2}$ for $FeSH^+$, measured mackinawite solubility should be two orders magnitude of higher than experiment observed values. Davison used mackinawite solubility measurement data to calculate $FeSH^+$ stability constant and the result is $10^{3.758\pm0.111}$ (Davison 1999), which is also supported by Rickard's observation (Rickard 2006). The inconsistence of β value determined by direct measurement and mackinawite solubility data calculation are still unknown.

Olshanskii determined the stability constants of $Fe(SH)_2$ and $Fe(SH)_3^-$ during iron sulfide solubility measurement, and their β values are $10^{6.0}$ and $10^{9.28}$ respectively (Olshanskii 1958). Later, Davison obtained a similar value of the stability constant of $Fe(SH)_2$ during iron sulfide solubility measurement, $10^{6.45}$, although Davison suggested that the ferrous sulfide complex could be polymeric $Fe_x(SH)_{2x}$ ($x \geq 2$). However, in PHREEQC, the stability constant of $Fe(SH)_2$ and $Fe(SH)_3^-$ are $10^{8.95}$ and $10^{10.987}$, respectively. Furthermore, Rickard did not find the evidence of $Fe(SH)_2$ and $Fe(SH)_3^-$ existences during mackinawite solubility measurement.

$FeS_{(aq)}$ is dissolved FeS cluster and has 1:1 stoichiometry, as defined by Rickard (Rickard 2006). Based on Luther and Rickard calculation with the HYPERCHEM program, the formula of $FeS_{(aq)}$ can vary from Fe_2S_2 to $Fe_{150}S_{150}$. Iron sulfide starts to condense at $Fe_{150}S_{150}$ (Rickard 2007). The Fe_2S_2 real formula is $Fe_2S_2 \cdot 4H_2O$, with a size of about 0.5 nm and volume of about 0.125 nm^3. The first condensed iron sulfide (assuming as $Fe_{150}S_{150}$) has a size of about 2 nm and volume of about 10 nm^3. The size and volume differences between these two species indicate that the condensed iron sulfide has orders of magnitude higher density than Fe_2S_2. By using the density discontinuity, it should be able to distinguish dissolved $FeS_{(aq)}$ and condensed iron sulfide, but more efforts are required to achieve this goal (Ohfuji 2006; Rickard 2007). According to Rickard (Rickard 2006), $FeS_{(aq)}$ mainly exists in neutral-alkaline system and has stability constant of $10^{-2.2}$ (equation 2.7),

$$Fe^{2+} + HS^- \rightarrow FeS_{(aq)} + \mathrm{H}^+,\ \beta = \frac{\{FeS_{(aq)}\}\{\mathrm{H}^+\}}{\{Fe^{2+}\}\{HS^-\}} = 10^{-2.2} \qquad (2.7)$$

If only consider $FeSH^+$ and $FeS_{(aq)}$, according to their stability constants, $FeSH^+$ dominates at pH < 6, and $FeS_{(aq)}$ dominates at pH > 6. Figure 2.2 displays the relative stability of iron complexes in an average seawater composition with total $\{Fe^{2+}\} = 10^{-9}$ (Rickard 2007).

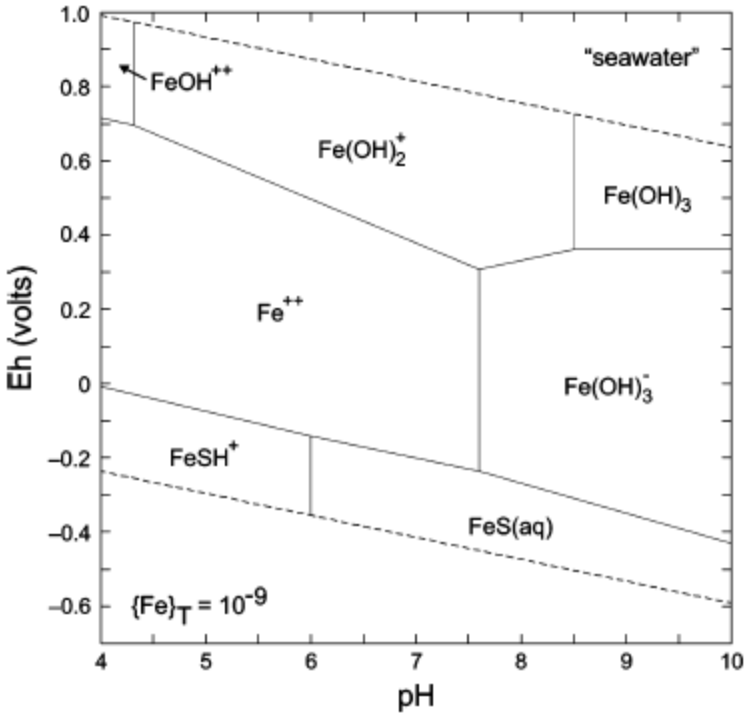

Figure 2.2. pH-Eh diagram of the relative stability of iron species in an average seawater composition and a total dissolved Fe(II) activity of 10^{-9} (Rickard 2007).

Based on the above statement, it seems that the chemical formulas of ferrous sulfide complexes and their stability constants are still not well known. More investigation is needed.

2.1.1.4. Other ferrous complexes in water

Besides ferrous hydroxide and ferrous sulfide complexes, ferrous ion can also form complex with many other anions in aqueous solution, such as Cl^-, SO_4^{2-}, CH_3COO^- (abbreviated as Ac^- hereafter), and CO_3^{2-}. These anions are fairly common in oil field produced water.

$FeCl^+$ is the most common ferrous chloride complex. Its stability increases with temperature. Several studies measured the stability constant of $FeCl^+$ at room temperature, but the results varied from $10^{-0.16}$ to $10^{-2.05}$ depending on the measurement methods (Heinrich 1990; Moog 2004). Benjamin recommended $10^{-0.2}$ as the stability constant of $FeCl^+$ in his book (Benjamin

2014). $FeAc^+$ complex has slightly higher stability constant, $10^{1.4}$. Fe^{2+} can also form complexes with SO_4^{2-} and CO_3^{2-} ions, and their complex forms could be $FeSO_{4(aq)}$, $FeHSO_4^+$, $FeHCO_3^+$, $FeCO_{3(aq)}$, and $Fe(CO_3)_2^{2-}$.Nordstrom et al. recommended some complexes' stability constants (Langmuir 1997; Nordstrom 1990), as shown in Table 2.1.

Table 2.1. Stability constants of ferrous complexes at 25 ℃ and zero ionic strength (Langmuir 1997; Nordstrom 1990).

Complex	Log ß
$FeCO_{3(aq)}$	5.1
$FeHCO_3^+$	2.0
$FeSO_{4(aq)}$	2.25
$FeHSO_4^+$	1.08

2.1.2. Sulfide chemistry in aqueous solution

In aqueous solution, S(-II) have three major species, H_2S, HS^-, and S^{2-}. The ratio of the three species depends on pH. Generally, H_2S is the dominate species when pH < 7; HS^- is the dominate species when pH > 7.

2.1.2.1. H_2S solubility in water and its dissociation constants

At room temperature, H_2S is in gas phase, but it can dissolve in water. H_2S gas is colorless but with characteristic rotten egg odor. It is poisonous, corrosive, flammable, and explosive. The solubility of H_2S in water is often expressed in the form of gas-liquid equilibrium constant, noted as K_{H_2S} (equation 2.8).

$$H_2S_{(g)} \rightarrow H_2S_{(aq)}, K_{H_2S} = \frac{\{H_2S_{(aq)}\}}{\{H_2S_{(g)}\}} \quad (2.8)$$

K_{H_2S} is a function of temperature and pressure. Many researches have been done on K_{H_2S} measurement and prediction at different temperature and pressure. Table 2.2 displayed several K_{H_2S} prediction models, and they generally agree well with each other. The model in software ScaleSoftPitzer (SSP), a mineral prediction software developed by my research group, include both temperature and pressure impacts on K_{H_2S}, and it is used for calculation in this thesis.

Table 2.2. K_{H_2S} prediction models as a function of temperature and pressure

Equation (the unit is mol/(L*bar), if not specifically noted)	Reference
$K_{H_2S}(molality/bar) = \begin{cases} \left(H_{H_2S} \cdot \exp\left(dV \cdot (P-1)/(0.083144 * \mathrm{T})\right)\right)^{-1}, if\ T \le 373.15\ K \\ \left(H_{H_2S} \cdot \exp\left(dV \cdot (P-P_{sat})/(0.083144 * \mathrm{T})\right)\right)^{-1}, if\ T > 373.15\ K \end{cases}$ $H_{H_2S} = \exp\left(13788/\mathrm{T} - 185.19 + 29.087 * \ln(\mathrm{T}) - 0.027637 * \mathrm{T} - 1445200/\mathrm{T}^2\right)$ $dV = \begin{pmatrix} 33.18 + 0.092661 * (T-273.15) - 0.00054853 * (T-273.15)^2 \\ + 0.0000015354 * (T-273.15)^3 - 0.0000000015459 * (T-273.15)^4 \end{pmatrix} * 0.001$ *, where the units of P and T are bar and K.*	SSP
$K_{H_2S} = \exp\left[-41.0563 + 66.4005\left(\frac{100}{T_K}\right) + 15.1060 \ln\left(\frac{T_K}{100}\right)\right]$	(Weiss 1970)
$K_{H_2S} = 10^{-[634.27+0.2709T_K-(0.11132 \times 10^{-3}T_K{}^2)-(16719/T_K)-(261.9 \log T_K)]}$	(Suleimenov 1994)
$K_{H_2S} = 10^{-0.71742672-(0.012145427T_C)+(5.6659982\times10^{-5})T_C{}^2-(8.1902716\times10^{-8})T_C{}^3}$	(Nordsveen 2003)

Dissolved H_2S acts as a weak dibasic acid, as shown in equation 2.9 and equation 2.10.

$$H_2S_{(aq)} \rightarrow HS^- + H^+, K_{a1} = \frac{\{HS^-\}\{H^+\}}{\{H_2S_{(aq)}\}} \quad (2.9)$$

$$HS^- \rightarrow S^{2-} + H^+, K_{a2} = \frac{\{S^{2-}\}\{H^+\}}{\{HS^-\}} \quad (2.10)$$

After years of study on H_2S dissociation, researchers generally agree pK_{a1} = 7.00 ± 0.02 (Sun 2008), but disagree on pK_{a2} value. The measured pK_{a2} can vary from 12.00 to 17.20 (Su 1997; Sun 2008; Yagil 1967), which is probably due to the difficulty of S^{2-} measurement. K_{a1} is a function of temperature and pressure, and many K_{a1} prediction models generally agree with each other. In this thesis, the model for K_{a1} calculation (equation 2.11) is from SSP.

$$pK_{a1} = -12.41 + 3539.1/T + 0.02522 * T \quad (2.11)$$

In this equation, T is in the unit of K. R is gas constant, 8.314 J/(K·mol). At 25 °C, this model gives a pK_{a1} value of 6.98. In the oil and gas produced water and natural water system, pH are normally in the range 4 – 8, in which the concentration of the S^{2-} species is extremely small and the use of K_{a2} can be avoided (see equation 2.16 below).

2.1.2.2. Sulfide oxidation

In order for sulfide with an oxidation number of minus two, S(-II), to be stable in solution, the solution must be anoxic. An H_2S solution is very clear when the solution is O_2-free. Once H_2S gets oxidized by O_2, the solution will become whitish with colloidal suspensions when pH < 6, or the solution will become straw or greenish when pH = 6 – 9 (Morse 1987). As explained by the redox potentials of H_2S and O_2 (equations 2.12, 2.13) (Stumm 1995). O_2 can easily oxidize

H_2S, especially in acidic condition. Since H_2S and HS^- have similar redox potential, only H_2S is taken as an example here.

$$\frac{1}{2}S_{(s)} + H^+ + e^- \rightarrow \frac{1}{2}H_2S_{(aq)},\ E^o = +0.14V$$

(2.12)

$$\begin{aligned}&\frac{1}{4}O_{2(g)} + H^+ + e^- \rightarrow \frac{1}{2}H_2O,\ E^o = +1.23V, or\\ &\frac{1}{4}O_{2(g)} + \frac{1}{2}H_2O + e^- \rightarrow OH^-,\ E^o = +0.4V\end{aligned} \qquad (2.13)$$

The first oxidation product of S(-II) is polysulfide, S_n(-II), where $n \geq 2$. For example, S_2(-II) is incorporated in the formation of pyrite (FeS_2), and pyrite is usually transformed from iron mono-sulfide (e.g. mackinawite) by oxidation (Rickard 2007). S_n(-II) can exist in three forms, H_2S_n, HS_n^-, and S_n^{2-}. The stability constants of S_n(-II) are difficult to determine due to the difficulty in S_n(-II) measurement. Instead, S_n(-II) stability constants are calculated based on free energy. However, S_n(-II) is metastable species and can be further oxidized to element sulfur (S^0) or even to sulfate (SO_4^{2-}) by O_2 or other oxidants, if it didn't react with other ions to form stable compounds. Figure 2.3 and 2.4 are the pH-Eh diagrams for stable sulfur species in aqueous solution and for polysulfide species with stable species removed, respectively. From Figure 2.4, H_2S_2 and HS_2^- species have broader Eh range than other S_n(-II), which may help explaining the natural abundant existence of iron disulfide (e.g. pyrite (FeS_2)), instead of FeS_n ($n>2$).

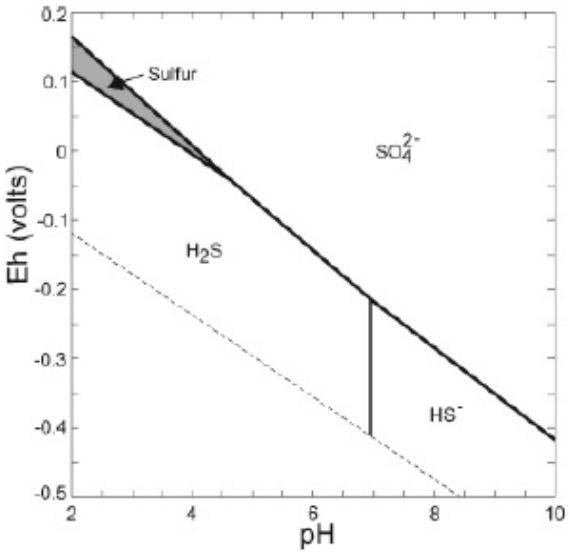

Figure 2.3. "pH-Eh diagram for stable sulfur species in aqueous solution at 25 °C, 1 bar total pressure, and $\sum\{S\} = 10^{-3}\ M$." (Rickard 2007)

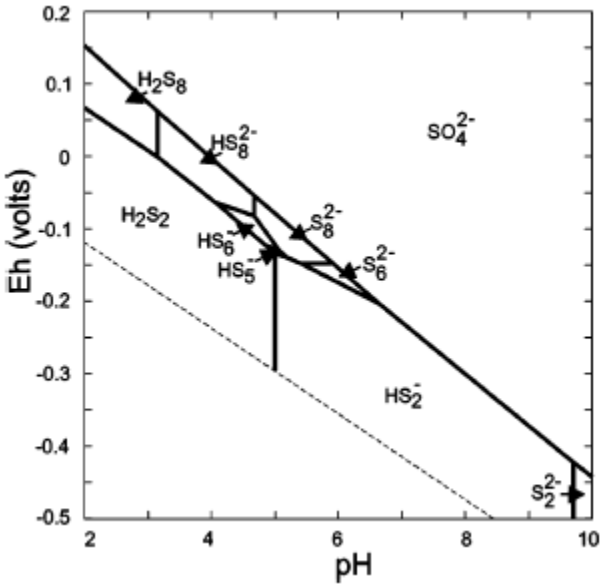

Figure 2.4. pH-Eh diagram for polysulfide species (with stable phases removed) (Rickard 2007)

As to the kinetics of H_2S oxidation by O_2 in aqueous solution, the overall oxidation rate can be given as equation 2.14.

$$\frac{d[H_2S]}{dt} = k_n \{H_2S\}^a \{O_2\}^b \quad (2.14)$$

When $\{O_2\} >> \{H_2S\}$, the oxidation becomes pseudo 1st-order reaction, and the reaction rate can be written as equation 2.15.

$$\frac{d[H_2S]}{dt} = k_1 \{H_2S\} \quad (2.15)$$

However, the rate constant measured by different workers differ so much that the calculated half life of H_2S can vary from 0.4 to 65 h, which is largely due to different experimental conditions (Morse 1987). H_2S oxidation rate can be affected by many factors, including pH, temperature, metal ions, and organic compounds. Figure 2.5 shows how the pseudo 1st-order rate constant (k_1) changes with pH. When pH < 6, the oxidation is very slowly; when 6 < pH < 8.5, the oxidation rate increases rapidly, mainly because H_2S dissociates into HS^- and HS^- oxidation rate is much quicker than H_2S. When pH > 8.5, the trend of the oxidation rate becomes complicated, which may be related to polysulfide formation (Morse 1987). The oxidation rate increases with temperature. Some metal ions, such as Ni^{2+}, Co^{2+}, Mn^{2+}, Cu^{2+}, Fe^{2+}, Ca^{2+}, and Mg^{2+}, can accelerate H_2S oxidation. Fe^{2+}, Ca^{2+}, and Mg^{2+} are very common metal ions in the oil produced water. Some organic compounds, such as phenols, aldehydes, aniline, urea, and vanillin, will also speed up H_2S oxidation; while some other organic compounds, like EDTA, cyanide, citrate, peptone, and glycerol, will slow down H_2S oxidation (Morse 1987).

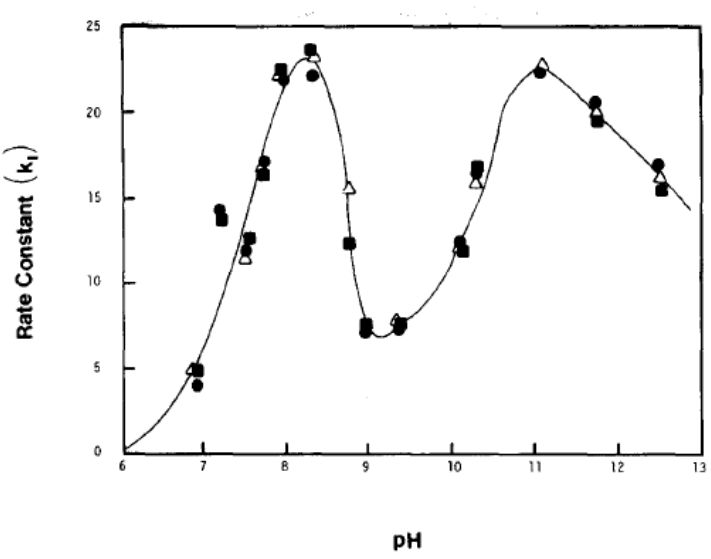

Figure 2.5. The pseudo first order rate constant of H_2S oxidation in water as a function of pH at 25 °C (Morse 1987).

2.2. Iron sulfide

Iron sulfide is a widespread mineral on earth. It is also ubiquitous in the oil field, especially in produced water injection and handling systems (Wylde 2014). Iron sulfide has many different solid phases, and Table 2.3 displays several typical phases and the related information. Mackinawite, cubic iron sulfide, troilite, and pyrrhotite are classified as iron monosulfide, although their stoichiometry is not necessarily 1:1. Pyrite and marcasite are iron disulfide, and their stoichiometry is strictly 1:2. These different phases can transform from one to another in certain conditions, and their relative stability depends on many factors, such as temperature, Eh, and pH. Lower Eh favors the formation of iron monosulfide, and higher Eh favors the formation of iron disulfide. In fact, iron disulfide is usually transformed from iron monosulfide through slight oxidation, instead of forming directly from aqueous solution. Figure 2.6 displays how iron,

sulfide and iron sulfide species change with pH and Eh (Kocabag 1990). The details of each phase and their inner transformation will be illustrated at sections below.

Table 2.3. "The solid phases in the Fe-S system" (Rickard 2007)

material	composition	structure	properties	natural abundance
mackinawite	FeS_m	tetragonal *P*4/*nmm*	metastable material that is the major constituent of the FeS precipitated from aqueous solutions	widespread mineral in low-temperature aqueous environments
cubic FeS	FeS_c	cubic $F\bar{4}3m$	highly unstable phase formed before FeS_m	not found naturally
troilite	FeS_t	hexagonal $P\bar{6}2c$	stoichiometric end member of the $Fe_{1-x}S$ group	mainly found in meteorites
pyrrhotite	$Fe_{1-x}S$	monoclinic, for example, *A*2/*a*; hexagonal *P*6/*mmc*	nonstoichiometric stable group where $x > 0.2$; monoclinic form is approximately Fe_7S_8; hexagonal form is approximately $Fe_{10}S_{11}$	most abundant iron sulfides in the Earth and solar system; rare in marine systems
smythite	Fe_9S_{11s}	hexagonal *R*3*m*	metastable phase related to the $Fe_{1-x}S$ group	rare mineral mainly found in hydrothermal systems usually associated with carbonates
greigite	Fe_3S_{4g}	cubic *Fd*3*m*	metastable $Fe^{II}Fe^{III}$ sulfide; the thiospinel of iron	fairly widespread mineral particularly associated with fresh water systems
pyrite	FeS_{2p}	cubic *Pa*3	stable iron(II) disulfide known as "fool's gold"	the most abundant mineral on the Earth's surface
marcasite	FeS_{2m}	orthorhombic *Pnnm*	metastable iron(II) disulfide	locally common mineral in hydrothermal systems and in sedimentary rocks

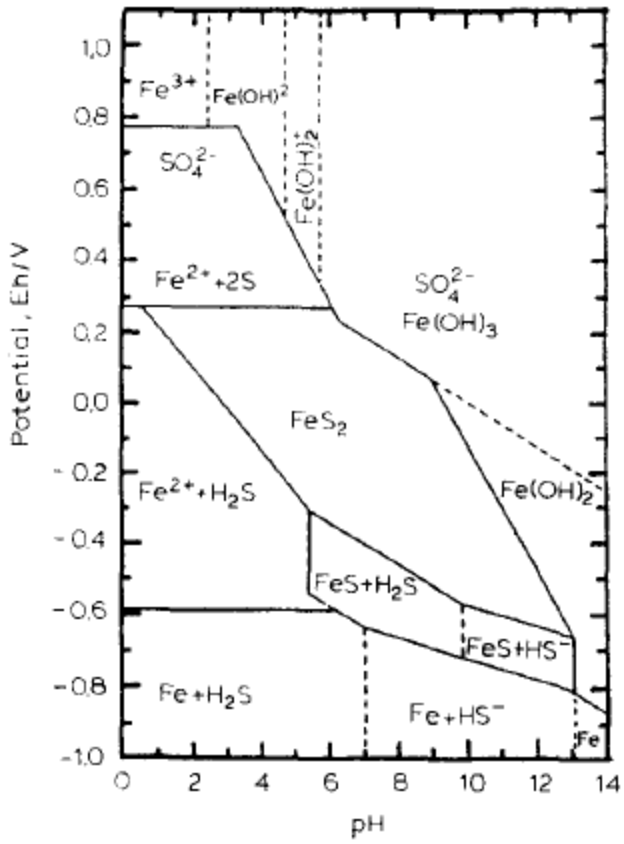

Figure 2.6. Eh-pH diagram of Fe-S-H_2O system at 25 °C and 10^{-5} mol/L Fe^{2+} and 10^{-5} mol/L S(-II) (Kocabag 1990).

2.2.1. Mackinawite

2.2.1.1. Mackinawite structure and composition

Mackinawite is a black opaque mineral, with calculated density of 4.17 g/cm^3 (Database 2016). It can occur as black sedimentary iron sulfide at ambient temperature and as sulfide deposits at high temperature (Morse 1987). It has tetragonal structure, as shown in Figure 2.7. The cell parameters are $a = b$ = 3.6735 Å and c = 5.0329 Å, and the unit cell volume = 68 Å^3. The Fe atoms form sheets with Fe in square planar coordination. The Fe-Fe distance is 2.5967 Å, which is the similar distance of Fe-Fe in α-iron (Database 2016). The Scanning electron microscope

(SEM) micrographs of mackinawite are shown in Figure 2.8, and different synthesize conditions show different morphologies. X-ray Powder Diffraction (XRD), one of the primary techniques for unknown material determination and examination, is often used to identify iron sulfide phases. In XRD detection, mackinawite three most intense interplanar spacings (D) are 5.030, 2.310, and 2.970 (Mineralogy 2016).

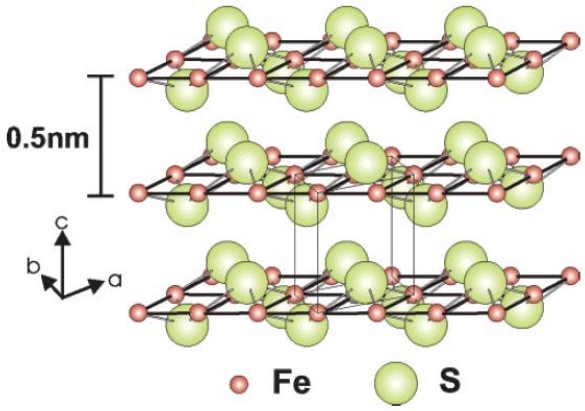

Figure 2.7. The structure of mackinawite

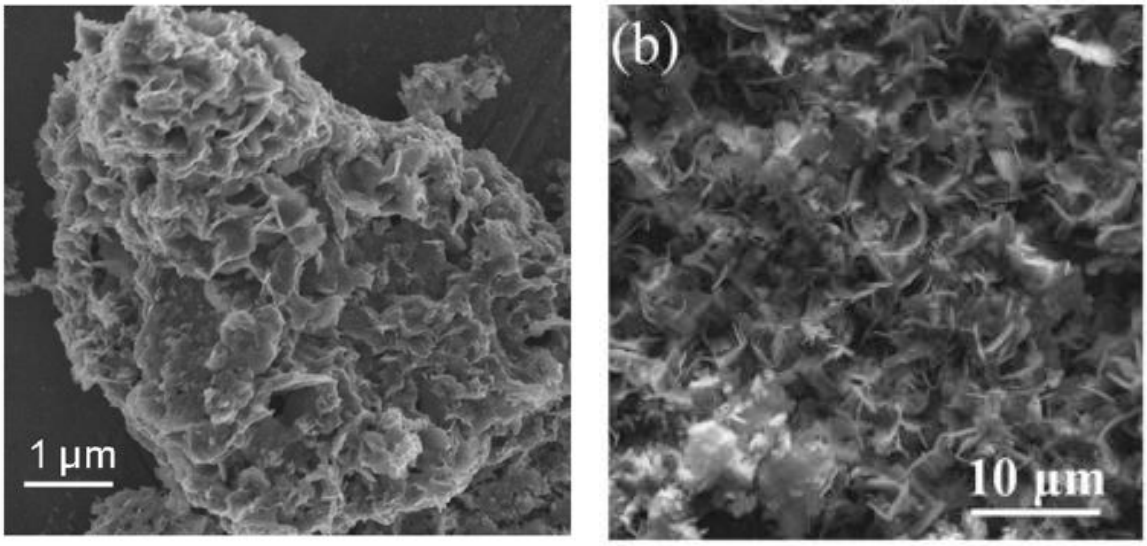

Figure 2.8. Mackinawite SEM pictures (The left one is synthesized by mixing Fe(II) and S(-II) solutions (Csákberényi-Malasics 2012); the right one is synthesized by H_2S corrosion on steel (Bai 2015).)

In mackinawite composition analysis, the most common way is to dissolve mackinawite in mineral acid and measure dissolved Fe^{2+} and S(-II) concentrations. During dissolution, small amount of S(-II) is often oxidized to element sulfur (S^0), and S^0 is not soluble in mineral acid, which mistakenly makes people believe that mackinawite is nonstoichiometric sulfur deficient iron sulfide with a formula of $Fe_{1+x}S$. $Fe_{1+x}S$ was used as mackinawite formula for a long time until Rickard discovered the S(-II) oxidation problem. To avoid S(-II) oxidation, he added a reducing reagent, Ti(III) citrate, into mineral acid. Finally, Rickard proved that mackinawite is actually stoichiometric iron sulfide with a formula of FeS (Rickard 2006), which is now generally accepted.

2.2.1.2. Mackinawite solubility

Numerous researches have been done on mackinawite solubility measurement. In general, there are two ways to measure. One is that mackinawite first precipitated from solution and then dissolved in acid (Davison 1999); the other one is that mackinawite is dissolved first and then re-precipitated (Benning 2000). The solubility product constant is usually expressed as in equation 2.16 or equation 2.17. S^{2-} based expression is usually not used because of the difficulty of S^{2-} measurement and the uncertainty of K_{a2} value. This thesis uses $K_{sp(HS^-)}$ form for iron sulfide solubility product and abbreviate it as K_{sp} below.

$$FeS + H^+ \rightarrow Fe^{2+} + HS^-,\ K_{sp(HS^-)} = \frac{\{Fe^{2+}\}\{HS^-\}}{\{H^+\}} \tag{2.16}$$

$$FeS + 2H^+ \rightarrow Fe^{2+} + H_2S,\ K_{sp(H_2S)} = \frac{\{Fe^{2+}\}\{H_2S\}}{\{H^+\}^2} \tag{2.17}$$

$$K_{sp(HS^-)} = K_{sp(H_2S)} \cdot K_{a1} \tag{2.18}$$

The measured log K_{sp} value (at ambient temperature) varied significantly and below are a few examples, -2.95 (Berner 1967), -3.5 ± 0.25 (Rickard 2006), -3.6 ± 0.20 (Davison 1991), and -3.90 ± 0.10 (Benning 2000). Such difference may be related to mackinawite preparation conditions. Different researchers recommended different K_{sp} values, and the exact value is still in debate. K_{sp} is also a function of temperature and pressure. In this thesis, K_{sp} is calculated based on equation 2.19, modified from a K_{sp} equation in literature (Naumov 1974).

$$pK_{sp} = -131.7569 + 6433.6172/T + 19.9617 * \ln(T) \tag{2.19}$$

where T and P are in the units of K and bar, respectively. At 25 °C, 1.01325 bar condition, the calculated pK_{sp} = 3.54, which is in the reasonable range of reported values.

From equation 2.16 and 2.17, it can be seen that mackinawite solubility highly depends on pH, which is true at certain pH range (pH < about 6). When pH is above a certain value, mackinawite solubility may become a constant and be independent from pH, according to Rickard (Rickard 2006). As shown in Figure 2.9, at pH < about 6, $\log K_{sp(H_2S)} = 3.5$ (log K_{sp} = -3.5); at pH > about 6, dissolved mackinawite exists as aqueous FeS cluster complex ($FeS_{(aq)}^{0}$), with $\log K_{sp(FeS^0)} = -5.7$ (Rickard 2006). The exact pH boundary depends on total S(-II) concentration. In this thesis, $\log K_{sp(FeS^0)} = -5.7$ is adopted when mackinawite solubility becomes lower than $10^{-5.7}$.

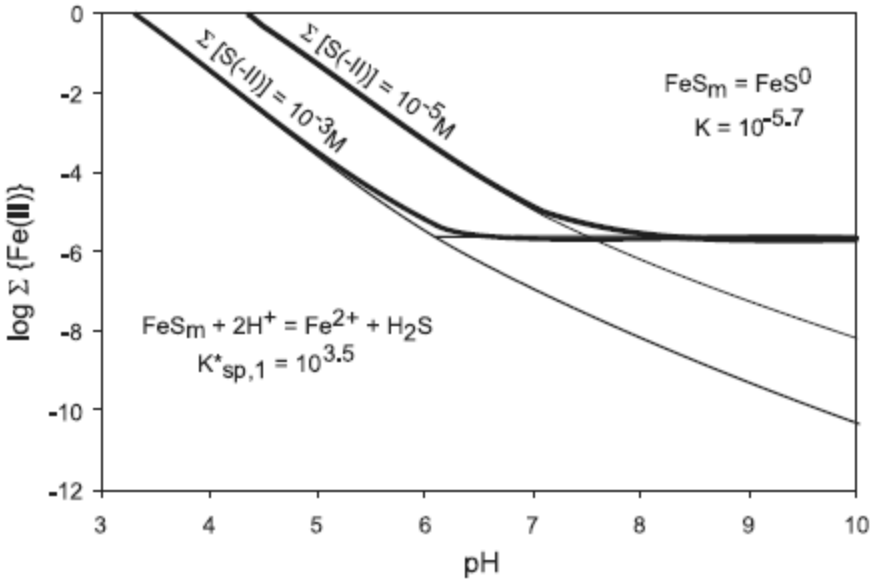

Figure 2.9. "Total activity of dissolved Fe(II) in equilibrium with mackinawite (bold lines) at 25 ºC and total dissolved S(-II) concentrations, $\sum\left[S\left(-II\right)\right]$, of 10^{-3} and 10^{-5} mol/L resulting from the Fe(II) activities of the pH-dependent and pH-independent reactions (fine lines)." (Rickard 2006)

2.2.1.3. Mackinawite formation kinetics and mechanism

As mentioned above, mackinawite can be synthesized by mixing Fe^{2+} and S(-II) aqueous solutions, or by H_2S corrosion on steel. The mechanism behind mackinawite formation involves two competing pathways, according to Rickard (Rickard 1995). One is H_2S pathway, as displayed in Eq 2.20. Fe^{2+} reacts with H_2S to form mackinawite directly. The other one is HS^- pathway, as shown in equation 2.21. It contains two steps. First Fe^{2+} reacts with HS^- to form $Fe(HS)_2$ complex, and then $Fe(HS)_2$ complex condense to mackinawite (Rickard 1995). $Fe(HS)_2$ complex is thermodynamically unstable.

$$Fe^{2+} + H_2S \rightarrow FeS + 2H^+ \qquad (2.20)$$

$$Fe^{2+} + 2HS^- \rightarrow Fe(HS)_2,\ Fe(HS)_2 \rightarrow FeS + H^+ + HS^- \quad (2.21)$$

The rate controlling step behind these two reactions is the exchange of water molecules inside hexa-aqua iron sulfide outer sphere complexes and inner sphere complexes, as illustrated in equation 2.22 and equation 2.23.

$$Fe(H_2O)_6^{2+} \cdot H_2S \rightarrow FeH_2S \cdot (H_2O)_6^{2+} \quad (2.22)$$

$$Fe(H_2O)_6^{2+} \cdot HS^- \rightarrow FeHS \cdot (H_2O)_6^{+} \quad (2.23)$$

The overall mackinawite formation rate is expressed as equation 2.24 in case of H_2S pathway, and as equation 2.25 in case of HS^- pathway.

$$d[FeS]/dt = k_1 \{Fe^{2+}\}\{H_2S\} \quad (2.24)$$

$$d[FeS]/dt = k_2 \{Fe^{2+}\}\{HS^-\} \quad (2.25)$$

Rickard measured mackinawite formation kinetics and its second order reaction rate is 1.5 – 15 L/(mol·sec) (Rickard 1995), which is considerably fast. However, mackinawite formation kinetics study is still rather rare due to the experimental difficulty, and more relative study is desired for comparison, especially at different temperature and water composition.

H_2S and HS^- pathways are in competition in mackinawite formation, and which pathway dominates depends on pH and total S(-II) concentration. When total S(-II) concentration $\geq 10^{-3}$ mol/L, H_2S pathway dominates only at acidic condition, and mostly HS^- pathway dominates. When total S(-II) concentration $< 10^{-3}$ mol/L, H_2S pathway dominates at pH < 8. Besides,

regardless of total S(-II) concentration, the formation rate at neutral to alkaline conditions is always higher than in acidic condition (Rickard 1995).

2.2.1.4. Mackinawite transformation

Mackinawite is usually the first iron sulfide to form in Fe^{2+} and S(-II) aqueous solutions and in H_2S corrosion on steel. One possible reason for this phenomenon is the rapid formation kinetics of mackinawite. In the view of thermodynamics, mackinawite is not as stable as some other iron sulfide phases like pyrite. The relative instability will make mackinawite eventually transform into thermodynamically favored phases. Mackinawite has been observed to transform to troilite, pyrrhotite, gregite, and pyrite (Benning 2000; Hunger 2007; Ma 2000; Rickard 2007).

2.2.1.5. Amorphous FeS and mackinawite

There is an iron sulfide that shows no pattern or only one broad peak at 5.4 Å in XRD examination, and it is named amorphous FeS (Rickard 2007). Amorphous FeS has been observed in many iron sulfide studies. It can be produced by mixing Fe^{2+} and S(-II) aqueous solutions. However, whether amorphous FeS is a specific iron sulfide phase or it is a colloidal form of mackinawite is still debated.

Some researchers consider amorphous FeS as fine grained nanocrystalline mackinawite. Amorphous FeS has same tetragonal structure and same chemical composition as mackinawite (Rickard 2007).

Some other researchers believe that amorphous FeS is different from mackinawite and may be a precursor to mackinawite. Firstly, amorphous FeS and mackinawite show different patterns or images in XRD, SEM and transmission electron microscopy (TEM) (Csákberényi-Malasics 2012). As mentioned previously, amorphous FeS shows either no pattern or a broad peak at 5.4

Å; while, mackinawite has three most intense interplanar spacings (D) at 5.030, 2.310, and 2.970 Å. Figure 2.10 shows the SEM micrograph of amorphous FeS, which is different from Figure 2.8, SEM micrograph of mackinawite. Mackinawite is more crystalline ordered than amorphous FeS. In TEM measurements, the interlayer and intralayer spacings of amorphous FeS (5.3 - 6.3 and 3.0 – 3.1 Å, respectively) are larger than the corresponding spacings of mackinawite (5.03 and 2.6 Å, respectively) (Lemire 2013).

Secondly, amorphous FeS is distinctly more soluble than mackinawite. Several studies measured amorphous FeS solubility and gave $\log K_{sp(HS^-)}$ value of -2.95 (Davison 1991), -2.99 (Schoonen 1991), and -3.15 (Bågander 1994). Mackinawite solubility is generally lower than this, even though the wide variety of measured values (-3.00 to -4.00).

Thirdly, amorphous FeS will eventually transform to mackinawite. Rickard observed that amorphous FeS transforms to mackinawite within one hour (Rickard 1969). In Csákberényi-Malasics' observation, amorphous FeS didn't transform within 4 days, and it completely transformed to mackinawite and gregite after 2 months (Csákberényi-Malasics 2012). The environment conditions can significantly impact the transformation kinetics. Still, amorphous FeS is proposed to be a precursor of mackinawite.

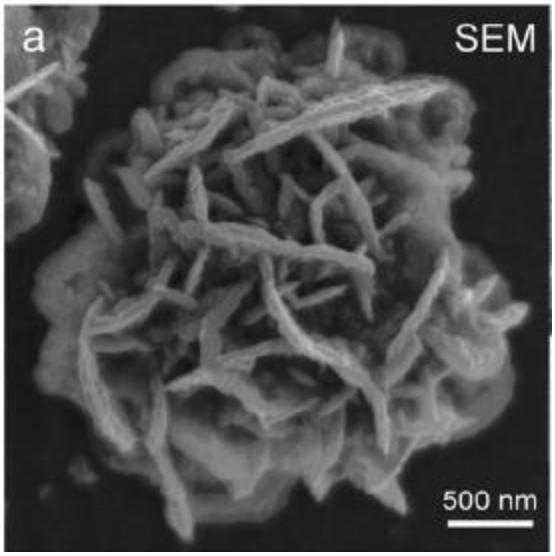

Figure 2.10. the SEM micrograph of amorphous FeS (Csákberényi-Malasics 2012).

2.2.2. Pyrrhotite group

2.2.2.1. Pyrrhotite and troilite structures and compositions

Pyrrhotite group includes pyrrhotite, troilite, and smythite.

Pyrrhotite is a bronze brown, bronze red, or dark brown opaque mineral, with measured density of 4.58 - 4.65 g/cm^3 (Database 2016). It is the most abundant iron sulfides in the Earth and solar system (Rickard 2007). The common formula is $Fe_{1-x}S$ ($0 < x < 0.2$). Pyrrhotite is based on NiAs structure (Figure 2.11) and has several poly-types, including pyrrhotite-4M (Fe_7S_8), pyrrhotite-5C (Fe_9S_{10}), pyrrhotite-6C ($Fe_{11}S_{12}$), pyrrhotite-7H (Fe_9S_{10}), pyrrhotite-11C ($Fe_{10}S_{11}$), and pyrrhotite-11H ($Fe_{10}S_{11}$) (Database 2016). Pyrrhotite-4M and pyrrhotite-11H are most common, and they can represent monoclinic and hexagonal pyrrhotite subgroups, respectively. Monoclinic pyrrhotite is more stable than hexagonal at T < 200 °C (Rickard 2007). Figure 2.12 displays the SEM micrograph of pyrrhotite-11H. In XRD detection, pyrrhotite three most intense interplanar spacings are 2.057, 2.635, and 2.966 (Mineralogy 2016).

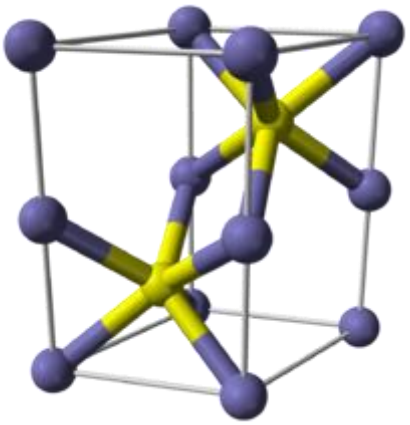

Figure 2.11. NiAs structure. (Yellow spheres are Fe atoms and blue spheres are S atoms)

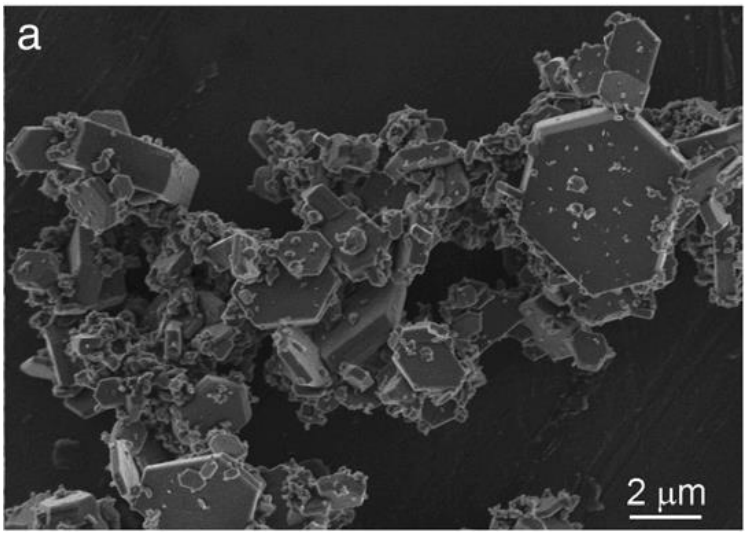

Figure 2.12. The SEM micrograph of pyrrhotite-11H (Csákberényi-Malasics 2012).

Troilite is the stoichiometric end-member of pyrrhotite group, with the formula of FeS. It is an opaque mineral, with gray brown, bronze brown or yellow brown color, and is mainly found in meteorites. The measured density is 4.67 - 4.79 g/cm^3. Troilite is hexagonal crystal, with cell parameters a = 5.958Å, c = 11.74Å, and unit cell volume = 361.7 Å^3 (Database 2016). Figure 2.13 shows two troilite SEM micrographs with different morphologies. The left one is quite similar to pyrrhotite-11H's (Lind 2010). The right one is needle-like and is a H_2S corrosion

product (Smith 2011). In XRD detection, troilite three most intense interplanar spacings are 2.09, 2.66, and 1.72 (Mineralogy 2016).

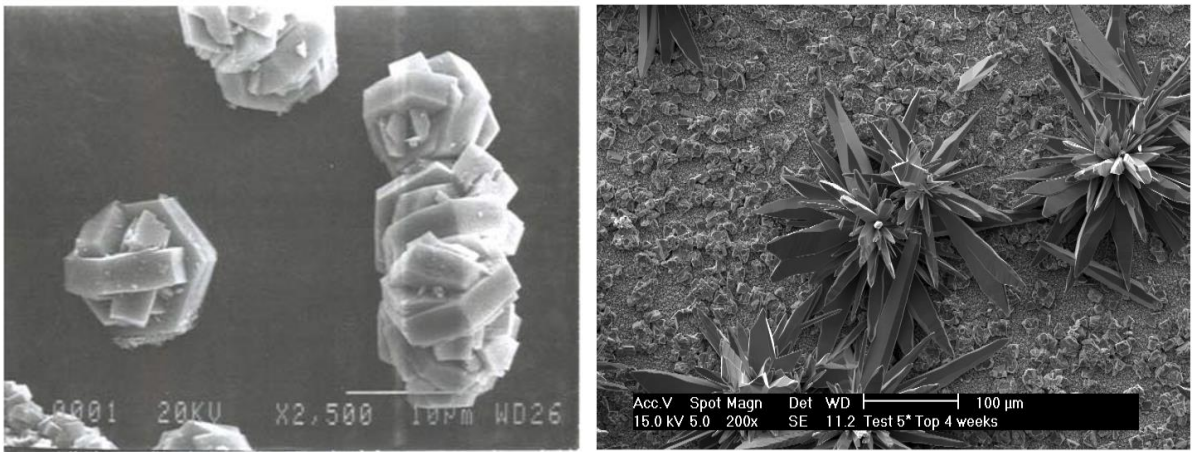

Figure 2.13. The SEM micrographs of troilite (Lind 2010; Smith 2011).

Smythite, Fe_9S_{11}, is also a member of pyrrhotite group, but it is metastable and rarely occurred on earth or in oil field.

2.2.2.2. Pyrrhotite and troilite solubility

The solubility of pyrrhotite and troilite have not been well studied, because it is very difficult or may be impossible to directly synthesize pyrrhotite or troilite at room temperature. The solubility shown in the literature is mostly calculated. For convenience, pyrrhotite and troilite solubility product constants are expressed the same way as mackinawite, shown in equation 2.16. In Davison's calculation (Davison 1991), at ambient temperature, log K_{sp} = -5.1 ± 0.1 for pyrrhotite, and log K_{sp} = -5.25 ± 0.2 for troilite. However, another literature report shows different values (Kharaka 1988). At 25 °C, pyrrhotite log K_{sp} = -3.76, and troilite log K_{sp} = -3.87. This literature also provides pyrrhotite and troilite K_{sp} values from 0 °C to 350 °C, as shown in Figure 2.14. More studies are needed to confirm the solubilities of pyrrhotite and troilite.

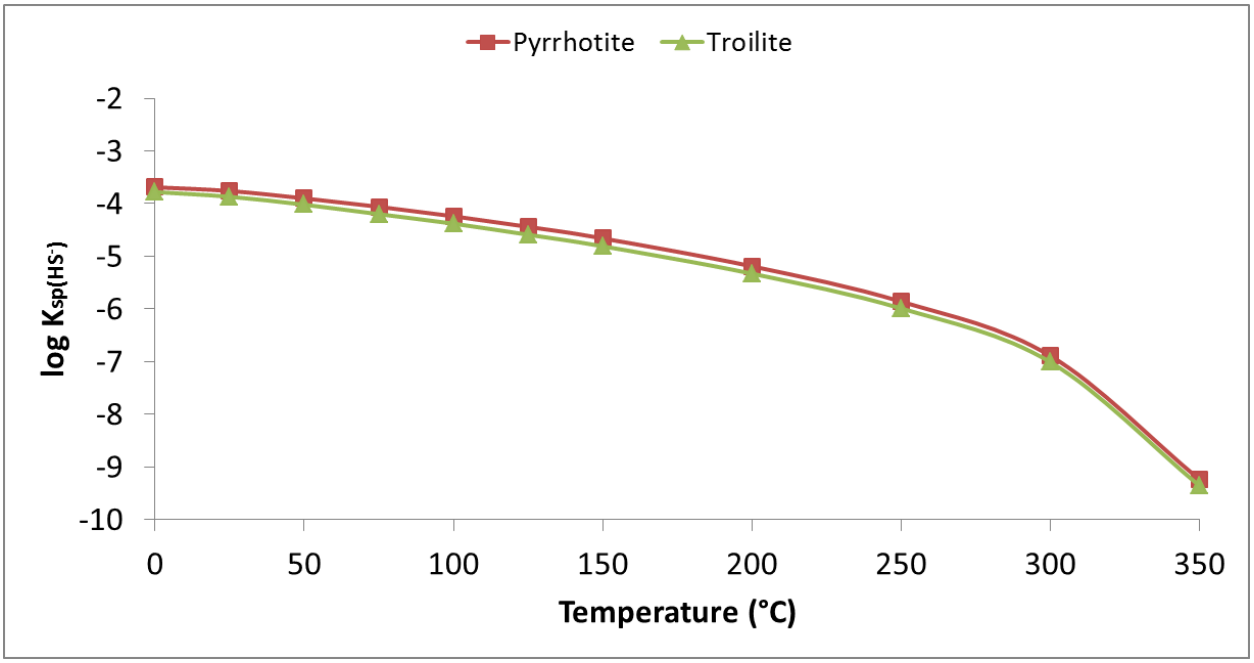

Figure 2.14. The solubility of pyrrhotite and troilite as a function of temperature (Kharaka 1988).

2.2.2.3. Pyrrhotite and troilite formation

Pyrrhotite and troilite formations are still mysteries. They may be able to be synthesized directly at high temperature, or be transformed from other phases, like mackinawite and cubic iron sulfide (Rickard 2007). It was observed that mackinawite can gradually transform to hexagonal pyrrhotite at 150 ℃ in aqueous solution (Csákberényi-Malasics 2012). In Murowchick's observation, troilite is formed when S(-II) solution reacts with metal iron at pH = 2 – 6 and T > 92 ℃. When T < 92 ℃, cubic iron sulfide is firstly formed and then transform to troilite and mackinawite (Murowchick 1986). More researches are required in pyrrhotite and troilite formation mechanisms.

2.2.3. Greigite

2.2.3.1. Greigite structure and composition

Greigite is thiospinel of iron, Fe_3S_4, an opaque mineral, with measured density of 4.049 g/cm^3 (Database 2016). It shows highly ferromagnetic and semiconducting properties (Morse 1987). Greigite has a similar inverse spinel structure, containing tetrahedral A-site and octahedral B-site, as displayed in Figure 2.15. The structures of greigite and mackinawite show high homology. They are both cubic, close-packed array of S atoms linked by Fe atoms, as shown in Figure 2.16. Greigite has unit cell parameter a = 9.876 Å and cell volume of 963.26 Å^3. One unit cell consists of eight Fe_3S_4 moieties (Database 2016; Rickard 2007). The morphology of greigite can be spheres of intergrown octahedra, cubes, or granular (Database 2016).

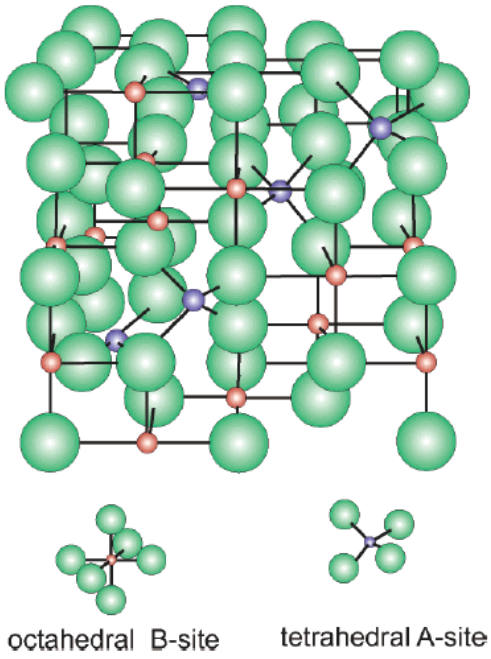

Figure 2.15. Greigite structure. (Big green sphere represents S atom; small blue and orange spheres represents Fe atoms.) (Rickard 2007)

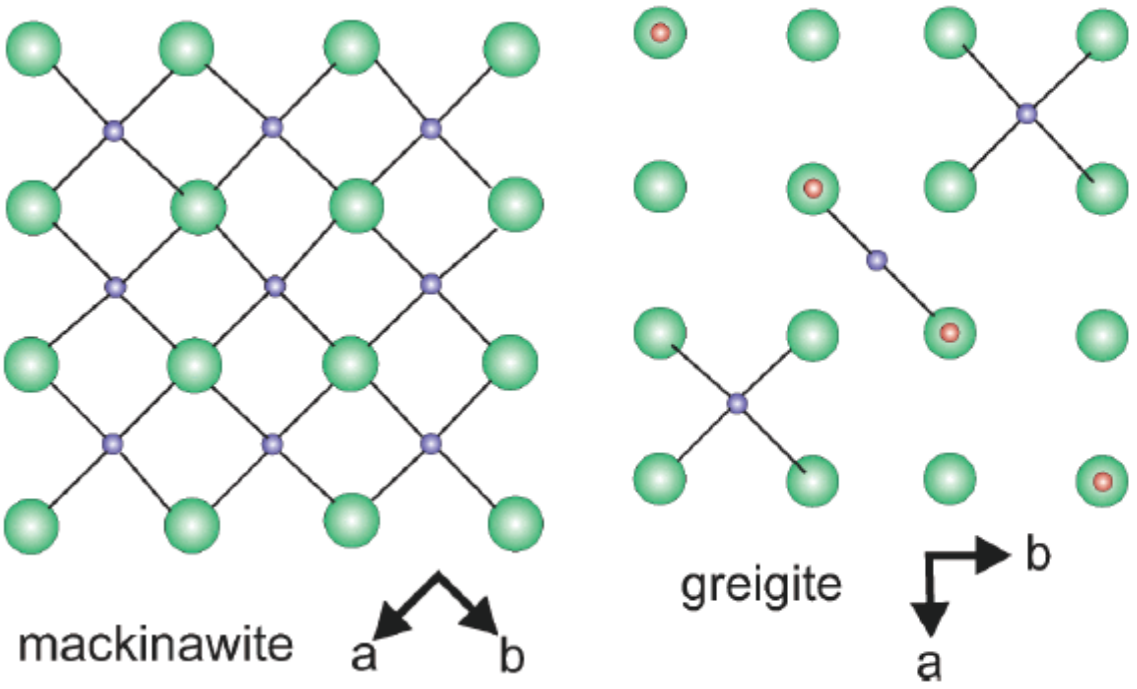

Figure 2.16. Homology of the structures of mackinawite and greigite. (Big green sphere represents S atom; small blue and orange spheres represents Fe atoms.) (Rickard 2007)

There is a controversy about the exact composition of greigite, which specifically refer to Fe^{II} and Fe^{III} arrangement in greigite. Three possibilities have been proposed. Firstly, Fe^{II} is in tetrahedral A-site and Fe^{III} is in octahedral B-site, which will give a spinel structure and a stoichiometric formula, $Fe^{II}(Fe^{III})_2S_4$. Nonetheless, the structure of greigite is inverse spinel. Secondly, Mossbauer spectrum suggests that Fe^{II} is in octahedral B-site and Fe^{III} is in both octahedral B-site and tetrahedral A-site, which gives the stoichiometric formula, $Fe^{II}(Fe^{III})_2S_4$ (Morse 1987; Vaughan 1970). Lastly, according to molecular orbital calculation (Rickard 2007), octahedral B-sites should contain both Fe^{II} and Fe^{III}, and this gives a nonstoichiometric formula, $Fe^{II}(Fe^{II}\ Fe^{III})S_4$. The uncertainty in greigite composition analysis could not preclude the possibility of nonstoichiometry. Therefore, the composition of greigite is still not for sure.

The SEM micrograph of greigite is shown in Figure 2.17. In XRD detection, greigite three most intense interplanar spacings are 2.980, 2.469, and 1.746 (Mineralogy 2016).

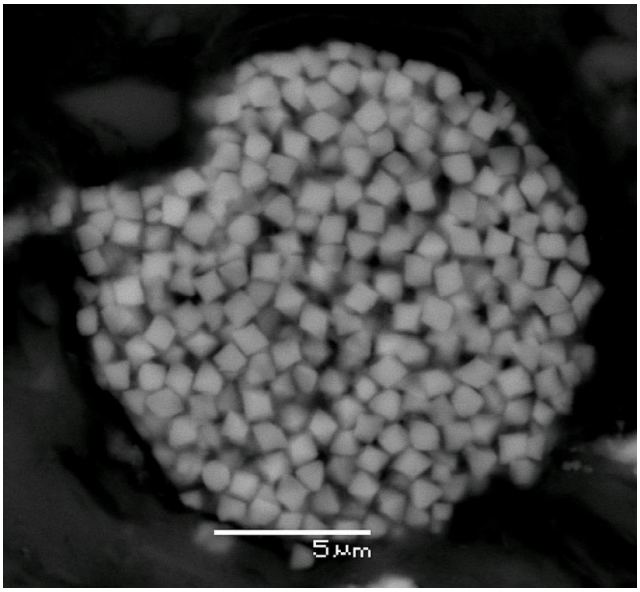

Figure 2.17. The SEM micrograph of greigite (Database 2016).

2.2.3.2. Greigite solubility

Few studies have been done on greigite solubility measurement, because of the big difficulty in pure greigite synthesis. Greigite is usually synthesized by aging mackinawite, but it is difficult to separate greigite from mackinawite (under aging) and pyrite (over aging). Given such difficulty, the solubility of gregite was measured only once by Berner (Rickard 2007). Berner used K_{a2} value of H_2S in greigite solubility calculation, but the exact value of K_{a2} is still not sure, which makes the calculated result not convincing. Rickard and Luther, by using Berner's original measurement data, recalculated greigite solubility with K_{a1} value of H_2S. The calculation is based on reaction in equation 2. 26. The solubility product constant is expressed as equation 2.27. $\log K_{sp(greigite)} = -12.84$ (Berner 1967; Rickard 2007).

$$Fe_3S_4 + 3H^+ \rightarrow 3Fe^{2+} + 3HS^- + S^0 \quad (2.26)$$

$$K_{sp(greigite)} = \frac{\left\{Fe^{2+}\right\}^3 \left\{HS^-\right\}^3}{\left\{H^+\right\}^3} \quad (2.27)$$

Note that Greigite originally doesn't contain element sulfur (S^0), but S^0 is produced during greigite digestion by mineral acids.

However, there is still a concern about the purity of Berner synthesized greigite. A certain amount of mackinawite was detected by XRD in the synthesized greigite (Rickard 2007). In this way, the measured apparent greigite solubility is actually higher than the real value. More accurate and well controlled measurement is required for greigite solubility.

2.2.3.3. Greigite formation mechanisms

There are many recipes of greigite synthesis, and all of them share one common thing, transformation from mackinawite. Even though some recipes start at mixing Fe^{2+} and S(-II) aqueous solutions, mackinawite is always formed first and then transform to greigite. Based on successful recipes, there are three proposed mechanisms.

Table 2.4. "Greigite recipes" (Rickard 2007).

reactants	T (°C)[a]	comments
FeS_m	25+	under TEM beam
FeS_m	200	anhydrous
$FeS_m + H_2S(g)$ + aldehydic carbonyl	40	aldehydic carbonyl recovered after reaction
$Fe(NH_4)_2(SO4)_2 + Na_2S + S(0)$	140	$Fe(NH_4)_2(SO_4)_2$ injected into Na_2S + S(0) mixture at 140 °C
$Fe(NH_4)_2(SO_4)_2 + Na_2S$ + sodium polysulfide	100	pH = 5.8−6.1
$Fe(NH_4)_2(SO_4)_2 + Na_2S$	190	FeS_m precipitated
$Fe(NH_4)_2(SO_4)_2 + Na_2S$ (pH = 5)	150	FeS_m precipitated
$Fe(NH_4)_2(SO_4)_2 + Na_2S$ (pH = 3)	100	FeS_m precipitated; H_2SO_4 added and product reheated to 80 °C
$FeSO_4 + H_2S(g)$	80	aerated $FeSO_4$ at pH = 3
$FeS_m \pm H_2S$ (g)	35−160	FeS_m freeze-dried and exposed to air
$FeSO_4 \pm Na_2S$	25	pH > 3.4−6.5

[a] Unless otherwise stated, the reactants were mixed at room temperature and heated to around the listed temperature for various periods.

The first one is solid state transformation. The reaction is equation 2.28.

$$4FeS + \frac{1}{2}O_{2(g)} \rightarrow Fe_3S_4 + FeO^*_{(s)} \qquad (2.28)$$

where FeO* represents an unspecified (oxyhydr)oxide of iron (e.g. FeO, Fe_2O_3). This reaction is thermodynamically favored, if the standard formation free energy of FeO* ($\mathbf{\Delta}G_f^0$(FeO*)) < -84.5 kJ/mol. The $\mathbf{\Delta}G_f^0$(FeO) = -244.3 kJ/mol and $\mathbf{\Delta}G_f^0(Fe_2O_3)$ = -741 kJ/mol, so the reaction can naturally happen. This reaction indicates that O_2 directly reacts with Fe^{II} to form Fe^{III}. Given the homology of the structures of greigite and mackinawite, mackinawite may rearrange Fe atoms in the cubic close-packed array of S atoms to transform to greigite in solid state (Rickard 2007).

The second one is autoxidation of mackinawite in water. The reaction is equation 2.29.

$$4FeS + 2H_2O \rightarrow Fe_3S_4 + Fe(OH)_2 + H_2 \qquad (2.29)$$

This reaction is not thermodynamically favored at 25 °C. Nevertheless, the reaction becomes possible when T > 70 °C, given the success of some greigite recipes (Table 2.4). It is likely that

the enthalpy of this reaction is not linear to temperature. Besides, lower pH and higher Eh condition can also promote greigite formation (Rickard 2007; Yamaguchi 1972).

Third one is mackinawite reacts with S^0. The reaction is equation 2.30.

$$3FeS + S^0 \rightarrow Fe_3S_4 \quad (2.30)$$

The reaction has standard reaction free energy $\mathbf{\Delta}G_r^0$ = -13.7 kJ/mol, so the reaction is thermodynamically favored. This reaction has been observed and proved by different researchers (Dekkers 2000; Hunger 2007; Rickard 2007).

Based on the above recipes and proposed mechanisms, it can be concluded that greigite is transformed from mackinawite and the transformation needs either oxidants, like O_2 and S^0, or water at high temperature. Certainly, greigite formation may not be limited to the above recipes and mechanisms.

2.2.4. Pyrite

2.2.4.1. Pyrite structure and composition

Pyrite is a pale brass to yellow opaque mineral, with measured density of 4.8 – 5.0 g/cm^3. It wide spreads on Earth, and has been found in sedimentary deposits, hydrothermal veins, and metamorphic rocks (Database 2016). Pyrite is a stoichiometric iron disulfide ($Fe^{II}S_2$) with a cubic structure similar to sodium chloride (NaCl), as displayed in Figure 2.18, except pyrite has relatively lower symmetry than NaCl (Rickard 2007). The cell parameter is a= 5.417 Å, and the unit cell volume = 158.96 Å^3. The morphology of pyrite is typically cubic or pyritohedral (pentagonal dodecahedral), or their combinations. Octahedral pyrite is less common (Database 2016). Figure 2.19 shows cubic, pyritohedral, and octahedral pyrite from left to right. In XRD

detection, greigite three most intense interplanar spacings are 1.633, 2.423, and 2.709 (Mineralogy 2016).

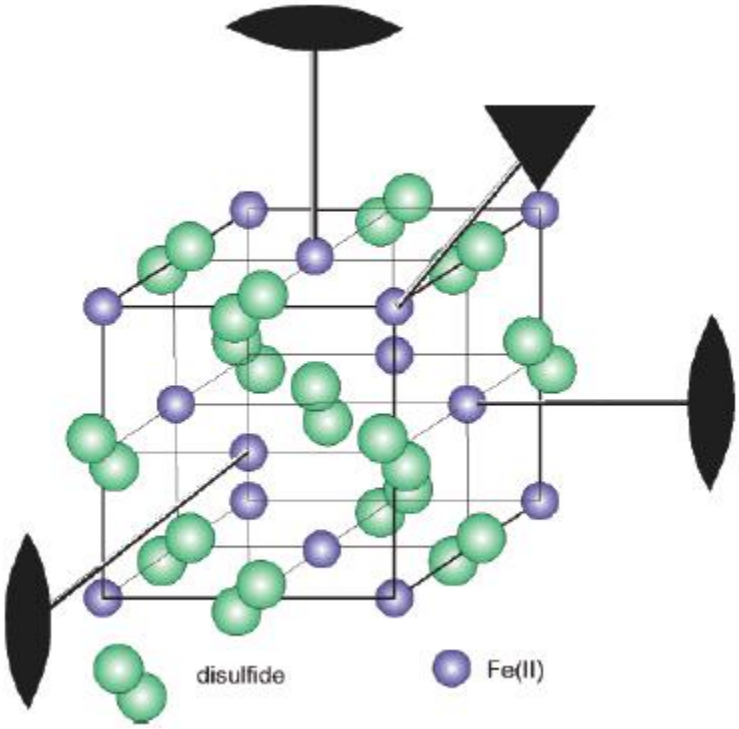

Figure 2.18. Pyrite structure (Rickard 2007).

Figure 2.19. Cubic (left), pyritohedral (middle), and octahedral (right) pyrite (Database 2016).

2.2.4.2. Pyrite solubility

Pyrite has such a low solubility that it can not be measured at ambient temperature. Instead, the solubility is calculated based on the heat capacity measurements of pyrite formation from its elements. The reaction for solubility calculation is shown in equation 2.31, and the solubility product constant is expressed as equation 2.32. Here, log $K_{sp(pyrite)}$ = -14.2 (Rickard 2007).

$$FeS_2 + H^+ \rightarrow Fe^{2+} + HS^- + S^0 \tag{2.31}$$

$$K_{sp(pyrite)} = \frac{\{Fe^{2+}\}\{HS^-\}}{\{H^+\}} \tag{2.32}$$

2.2.4.3. Pyrite transformation from other phases

Pyrite can not be directly synthesized by mixing aqueous Fe^{2+} and S(-II) solutions. It is often transformed from other iron sulfide phases, such as mackinawite, pyrrhotite, and greigite, because pyrite is thermodynamically more stable than other phases. Figure 2.20 shows typically observed phase transformation routes (Bai 2014; Benning 2000; Csákberényi-Malasics 2012; Hunger 2007; Jeong 2008; Smith 2006; Sun 2006). The transformation kinetics depends highly on oxidants and environmental conditions. Oxidants in pyrite formation can be S^0, S_n^{2-}, air, and even H_2S.

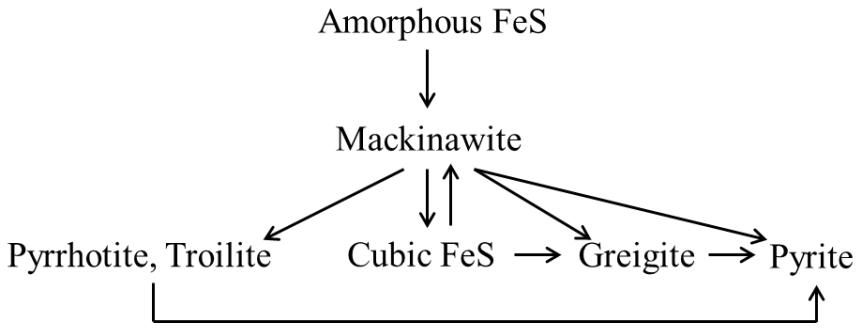

Figure 2.20. Iron sulfide phase transformation (Bai 2014; Benning 2000; Csákberényi-Malasics 2012; Hunger 2007; Jeong 2008; Smith 2006; Sun 2006).

Rickard and Luther looked into the transformation processes, and surprisingly concluded that pyrite is technically not solid-state transformed from other iron sulfide phases. Instead, pyrite is formed by firstly dissolving other iron sulfide phases and then re-precipitating as pyrite (Rickard 2007). Previously observed phase transformations to pyrite always involve aqueous solution (Rickard 2007). Moreover, there are several reasons why solid state transformation from mackinawite or greigite to pyrite is improbable.

First, in terms of structure, mackinawite and greigite have cubic, close-packed array of S atoms, but the structure of pyrite is the rationalized arrangement of the center points of S_2^{2-} molecules. The S lattice of pyrite is totally different from mackinawite and greigite. It would be difficult for mackinawite or greigite transform from its original structure to pyrite structure in solid state (Rickard 2007).

Second, in terms of particulate size, pyrite particulate is usually micro-sized, but mackinawite particulate precipitated from aqueous solution is only nano-sized. There is about 1000 times difference in their sizes (Rickard 2007).

Third, in terms of chemical composition, the valences of Fe and S atoms in greigite and pyrite are quite different. Greigite has Fe(II) and Fe(III) atoms and S(-II) atoms, while pyrite has only Fe(II) atoms and S_2(-II) atoms. Mackinawite solid state transformation to greigite only involves partial Fe(II) atoms transform to Fe(III) atoms. Greigite transformation to pyrite will involve more atom valence changes, making the process more complex and more difficult (Rickard 2007).

Given the above differences in structure, particulate size, and chemical composition, solid state transformation from mackinawite or greigite to pyrite is highly unlikely. Instead, Rickard and Luther proposed two formation mechanisms with aqueous solution involved, which will be illustrated in the below section.

2.2.4.4. Pyrite formation mechanisms and kinetics

Similar to typical mineral (e.g. barite and calcite) formation, pyrite formation consists of two processes, nucleation and crystal growth (Rickard 2007). The nucleation rate depends on pyrite supersaturation ratio and substrate. At low supersaturation ratio, nucleation rate is rate limiting step. When supersaturation ratio increases to a certain value (called supersaturation limit), nucleation rate will become greater than crystal growth rate and no longer be the rate limiting step (Rickard 2007). The substrate also affect nucleation rate. Rickard observed that organic substrate can lower supersaturation limit 3 magnitude orders (Rickard 2007). Mackinawite presence may also be able to accelerate pyrite nucleation rate so much that pyrite can nucleate spontaneously. Once pyrite nucleation finished, crystal growth is relatively rapid and its rate can be assumed to be reactant diffusion controlled. The overall pyrite formation rate will be discussed below.

There are two proposed mechanisms about pyrite formation (Rickard 2007). One is called Bunsen reaction and also called polysulfide controlled pyrite reaction. In this reaction, pyrite is formed through aqueous hexaqua Fe^{2+} reacting with sulfide and polysulfide sequentially, as shown in equation 2.33 and equation 2.34 (Rickard 2007; Rickard 1975).

$$Fe^{2+} + S(-II) \rightarrow [FeS] \tag{2.33}$$

$$[FeS] + S_n^{2-} \rightarrow FeS_2 + S_{n-1}^{2-} \tag{2.34}$$

In equation 2.33, [FeS] is an aqueous iron sulfide reaction intermediate, and the real formula should be $FeH_2S\cdot(H_2O)_5^{2+}$ or $FeSH\cdot(H_2O)_5^{+}$. The reaction rate is controlled by water molecules exchange from inside hexaqua iron sulfide outer sphere complexes to iron sulfide inner sphere complexes, similar to mackinawite formation situation. In equation 2.34, S_n^{2-} is polysulfide. The S_n^{2-} with higher nucleophilicity can react with [FeS] faster. Longer chain S_n^{2-} are usually more nucleophilic than shorter chain S_n^{2-}. There is a sequence of nucleophilicity of several commonly existed S_n^{2-}, $S_5^{2-} > S_4^{2-} > HS^- > HS_2^{2-} > S_3^{2-} > H_2S$. Consequently, the rate of reaction 2.34 largely depends on S_n^{2-} types and concentrations (Rickard 2007). As mentioned in sulfide chemistry section, S_n^{2-} is formed through S(-II) oxidation, and adding S^0 into S(-II) solution can promote S_n^{2-} formation. Therefore, S^0 is often added in pyrite synthesis.

Based on pyrite formation experiment data, the overall pyrite formation rate can be calculated as equation 2.35 (Rickard 1975).

$$\frac{\partial[FeS_2]}{\partial t} = k_{S_n^{2-}} A_{FeS}^2 A_{S^0} \{S(-II)\}_T \{H^+\} \tag{2.35}$$

Where A_{FeS} and A_{S^0} are the surface areas of iron monosulfide FeS (e.g. mackinawite) and S^0, which are assumed to be proportional to FeS and S^0 concentrations, respectively. The second order dependence on FeS is unusual. It could mean that FeS involves in two reaction steps, or FeS involves a rate limiting step. FeS for sure serves as Fe^{2+} source by dissolving FeS with H^+, so dissolving FeS may be the rate limiting step. Another possibility is that FeS also serves as S(-II) source during dissolution. S^0 is involved in S_n^{2-} formation, and S(-II) is directly involved in [FeS] formation (Rickard 2007; Rickard 1975).

Moreover, the S atoms in pyrite should all come from S_n^{2-}, as displayed in Figure 2.21. S_5^{2-} is taken as an example here. This mechanism has been isotopically confirmed by Butler (Butler 2004).

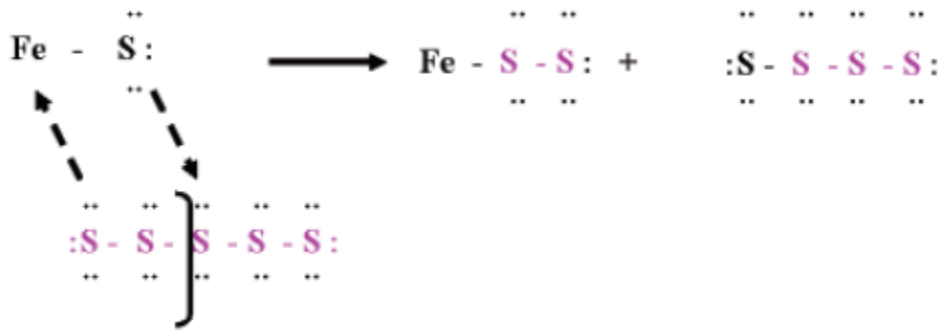

Figure 2.21. Proposed pyrite formation mechanism through Bunsen reaction (Rickard 2007).

The other proposed pyrite formation mechanism is Berzelius reaction, also called sulfide controlled reaction (Rickard 2007). In this reaction, aqueous dissolved iron monosulfide is oxidized by H_2S to form pyrite and hydrogen gas (H_2), as shown in equation 2.36.

$$FeS_{(aq.)} + H_2S \rightarrow \left[Fe - S \rightarrow SH_2\right] \rightarrow FeS_2 + H_2 \tag{2.36}$$

Where $\left[Fe - S \rightarrow SH_2\right]$ is a reaction intermediate in which electron transfer from S(-II) to H^+ so as to form S_2(-II) and H_2.

The Berzelius reaction rate is calculated by equation 2.37. It can be treated as second order reaction.

$$\frac{\partial\left[FeS_2\right]}{\partial t} = k_{H_2S}\left[FeS\right]\left[H_2S\right] \tag{2.37}$$

Berzelius reaction rate is usually much higher than Bunsen's, when reaction conditions are the same. In Bulter's experiment (Butler 2004), at the condition of enough FeS source, H_2S pressure = 0.03 atm, pH = 7, and T = 25 °C, pyrite is formed through Berzelius reaction and the formation rate is about 2 x 10^{-8} mol/(L·sec). If adding excess S^0, pyrite is formed through Bunsen reaction and the formation rate drops to about 8 x 10^{-11} mol/(L·sec). Based this observation, it can be inferred that when FeS is insufficient and H_2S and S_n^{2-} are at equal concentration, Berzelius reaction will dominate the pyrite formation.

In Berzelius reaction, the S atoms in pyrite come from both FeS and H_2S, as shown in Figure 2.22. Bulter also confirmed this mechanism (Butler 2004).

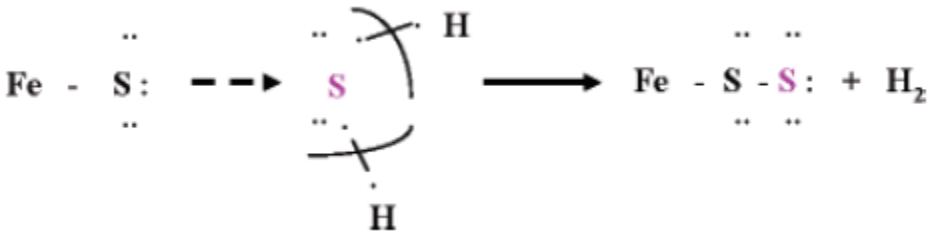

Figure 2.22. Proposed pyrite formation mechanism through Berzelius reaction.

If combing Bunsen and Berzelius reactions, the overall pyrite formation rate can be calculated by equation 2.38.

$$\frac{\partial[FeS_2]}{\partial t} = k_{H_2S}[FeS][H_2S] + k_{S_n^{2-}}[FeS]^2[S^0]\{S(-II)\}_T\{H^+\} \quad (2.38)$$

Based on the above equation, FeS, S^0, H_2S, S(-II), and H^+ concentrations will affect pyrite formation kinetics. There are also some other impact factors, such as temperature, pH, presence of organic compounds, and bacteria. Generally, high temperature accelerates pyrite formation (Rickard 2007). Trace amount of aldehydic carbonyl can inhibit pyrite formation (Rickard 2001).

Also, certain bacteria can catalyze pyrite formation and make the kinetics several orders of magnitude faster than abiologic system (Canfield 1998).

2.2.5. Other iron sulfides

Cubic iron sulfide (FeS) is a highly unstable iron sulfide phase and has never been found naturally (Rickard 2007). It can be synthesized by using S(-II) aqueous solution corrode metal iron at low temperature (T < 92 °C) (Murowchick 1986). Given its instability, cubic iron sulfide can easily transform to mackinawite. Mackinawite was also observed to transform to cubic iron sulfide (Shoesmith 1983; Shoesmith 1980).

Marcasite (FeS_2) is an orthorhombic iron disulfide. Marcasite synthesis needs pH < 6, and its occurrence is much less common than pyrite in nature (Rickard 2007). It was also observed in the oil field (Wang 2013).

2.3. Iron sulfide in oil industry

2.3.1. Iron sulfide caused challenges

Iron sulfide scale occurs frequently in the oil wells, especially in oil wells with high concentration H_2S (called sour wells). Figure 2.23 displays the scale composition in Khuff reservoir sour wells in Saudi Aramco fields. Iron sulfide scale can take up nearly half of total scales, and 80% of scales are iron related scales (Wang 2013).

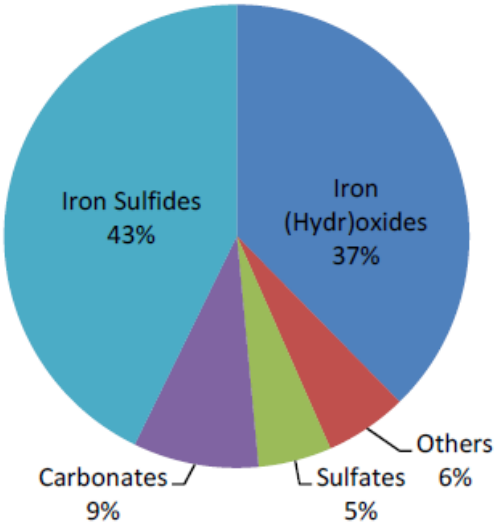

Figure 2.23. Averaged scale composition in Khuff reservoir sour gas wells in Saudi Aramco fields (Wang 2013).

The problems caused by iron sulfide scale can be very challenging. Below are several typical problems (Wylde 2014).

1. Oil well production capacity decreases, due to iron sulfide deposition in the formation, perforation, and around screens.
2. Oil well deliverability decreases, due to iron sulfide accumulation in the oil delivery tubulars.
3. Metal equipment (e.g. pumps and valves) are malfunctioned, due to iron sulfide formation on the metal surface.
4. Localized corrosion (e.g. pitting, crevice corrosion) happens, due to deposited iron sulfide.
5. Oil and produced water separation is interfered, due to that oil-wet iron sulfide particles exist in oil-water interface and stabilize emulsions.

6. Heat exchange efficacy of cooling water decreases, due to iron sulfide deposition on the inner surface of cooling water tubing.

Furthermore, iron sulfide is usually an indicator of H_2S corrosion, and aged iron sulfide, like pyrite, often indicates long term corrosion. Corrosion can cause as much problem as scale does.

Based on the above illustrated problems, iron sulfide scale can cause millions of economic loss every year. Iron sulfide scale problem needs to be faced and solved.

2.3.2. Iron sulfide formation in the oil field

2.3.2.1. Iron sources

To solve iron sulfide problem, firstly it is very necessary to know the reactant sources. There are three major iron (Fe^{2+}, or Fe^{3+}, or both) sources in the oil field.

Firstly and most importantly, corrosion can release a large amount of iron (Ramachandran 2015). Corrosion here includes H_2S and / or CO_2 caused corrosion and acid treatment caused corrosion. Acid treatment is a traditional method to remove acid dissolvable scales, such as sulfide and carbonate scales. In acid treatment, metals can be corroded and Fe^0 becomes Fe^{2+}, which makes ready for iron sulfide scale formation. Iron sulfide scale can become more severe after acid treatment (Nasr-El-Din 2001).

Secondly, iron could come from reservoir formation. Different reservoir rocks contain different iron content. Sandstone reservoir usually has high iron content (Nasr-El-Din 2001).

Thirdly, contaminated or unusual drilling fluid may contain iron (Ramachandran 2015). When contamination or corrosion happens during drilling process, iron will be introduced into drilling fluid. In some unusual drilling fluid, iron oxide or iron based hydrogen scavenger are added. Iron

oxide can be used as H_2S scavenger (Ray 1979) or as a weighing material for drilling fluid (Menzel 1973).

2.3.2.2. Sulfide sources

S(-II) in the oilfield mainly come from the following sources.

First, S(-II) can be generated by Sulfate Reducing Bacteria (SRB) through reducing sulfate or sulfite. SRB are anaerobic bacteria, and can naturally exist in the reservoir (Kelland 2014).

Second, thermal decomposition of sulfate will produce S(-II), which happens at high temperature reservoir (Kelland 2014).

Third, dissolution of sulfide minerals in the formation may release S(-II) (Wylde 2014).

Fourth, acid treatment of preexisted iron sulfide scale will release a large amount of S(-II) (Wylde 2014).

Last, H_2S can be introduced into oil wells during gas lift operations (Nasr-El-Din 2001).

2.3.2.3. Iron sulfide situation in the oil field

With enough iron and sulfide sources, iron sulfide scale is easy to form, given its extremely low solubility. In the oil field, several other impact factors, pH, temperature, pressure, and Eh, can also affect iron sulfide formation. Iron sulfide solubility is pH dependent (in certain pH range, e.g. $pH < 6$), and increasing pH can significantly reduce iron sulfide solubility. High temperature and high pressure can decrease iron sulfide solubility too (Naumov 1974), and thereby promote iron sulfide formation. High temperature can also accelerate iron sulfide formation and phase transformation kinetics (Rickard 2007). Proper Eh is required for the existence of Fe^{2+}, S(-II) and iron sulfide. Oil wells often provide ideal Eh condition for iron sulfide. When Eh is too high

(oxidized condition), Fe^{2+} and S(-II) will be oxidized to Fe^{3+} and S^0, respectively. This case may happen in some local areas when O_2 is accidently introduced into oil well. When Eh is too low (extremely reduced condition), Fe^{2+} will be reduced to Fe^0, but this case is highly unlikely to occur in the oil wells.

As to iron sulfide phases in the oil field, Pyrrhotite, troilite, mackinawite, and pyrite are most common. Figure 2.24 shows the relative abundance of different iron sulfide phases in Khuff reservoir sour wells in Saudi Aramco fields (Wang 2013), which is actually very representative.

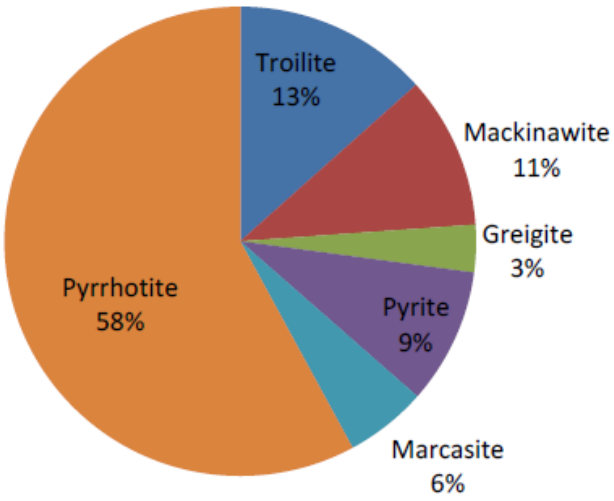

Figure 2.24. Relative abundance of different iron sulfide phases in Khuff reservoir sour wells in Saudi Aramco fields (Wang 2013).

As mentioned previously, when mixing Fe^{2+} and S(-II) solutions directly, mackinawite or amorphous FeS will be the precipitated iron sulfide phase. In the case of H_2S corroding metal steel, mackinawite is also the first appeared iron sulfide phase (Bai 2015; Ma 2000; Sun 2006). However, in the oilfield, pyrrhotite is usually the most common phase (Smith 2011; Wang 2013). It is believed that pyrrhotite is transformed from mackinawite, and the transformation process is related to pH, temperature, and time length (Smith 2011). Pyrite is also transformed from other

phases which can be mackinawite, pyrrhotite, or troilite. More researches are needed to investigate the real transformation processes and the transformation impact factors.

2.3.3. Iron sulfide control in the oil field

Scale control in the oil field usually means scale prevention and scale removal. Scale prevention also has two meanings. One is to prevent scale formation; the other is to prevent scale deposition by keeping scale particles dispersed in aqueous solution. The same rule is applied to iron sulfide control.

2.3.3.1. Iron sulfide prevention

Below are three typical approaches to prevent iron sulfide formation.

First, control iron sources with corrosion inhibitors and iron sequestration reagents. Corrosion inhibitors can prevent or alleviate metal corrosion to reduce released Fe^{2+}. Iron sequestration reagents are used to chelate Fe^{2+} and Fe^{3+} released from reservoir formation and drilling fluid. Nitrilotriacetic acid was reported to be an effective iron sequestration reagent, but it would decompose at T > 149°C (Kelland 2014). Another type of iron sequestration reagent is organic acids, such as Ethylenediaminetetraacetic acid (EDTA), citric acid, and glycolic acid (Kelland 2014; Wylde 2014). However, organic acids need stoichiometric amounts and could be corrosive (Kelland 2014). Besides, they are not Fe^{2+} and Fe^{3+} specific chelate reagents, and other high concentration cations (e.g. Ca^{2+}, Ba^{2+}, Sr^{2+}) can easily interfere their chelating efficacy.

Second, control S(-II) source with biocide and H_2S scavenger. Biocide can control SRB growth rate, so as to reduce H_2S production. THPS, Glutaraldehyde, and quaternary ammonium compounds are commonly employed biocides. THPS is easy to be oxidized in air and becomes an ineffective biocide (Nasr-El-Din 2000). Also, high concentration THPS can damage

sandstone reservoir formation (Talbot 2000). H_2S scavenger (e.g. aldehydes) can decrease H_2S concentration directly. However, H_2S scavenger can increase solution pH and cause severe carbonate scale (Sumestry 2012). Also, if H_2S scavenger is over reacted with H_2S, polymeric sulfur can happen and deposit in oil wells (Schieman 1999).

Third, prevent or retard iron sulfide formation with threshold inhibitors. Threshold inhibitors for common scales, such as calcite, barite, and gypsum, have been applied in the oil field for many years, but effective threshold inhibitors for iron sulfide have not been found yet. Since iron sulfide is an exotic scale to common ones, it probably needs totally different type of threshold inhibitors to work.

If iron sulfide is failed to be prevented, dispersants can be used to prevent iron sulfide particles from deposition. Several successful iron sulfide dispersants have been reported in the literature. 3-methacrylamido-propyl tri-methyl chloride was successfully applied in the oil wells in North Dakota (Smith 2010). Another polymeric compound with amine group was reported to be able to disperse iron sulfide particles into sub-micro size and keep them in the solution for more than 12 hours without any deposition (Bhandari 2016). In terms of flow assurance, keeping iron sulfide particles in the solution is probably enough to ensure oil well deliverability. However, in terms of produced water treatment, dispersed iron sulfide will be difficult to remove.

Furthermore, in iron sulfide prevention, it is very important to accurately calculate iron sulfide supersaturation in gas, aqueous and oil phases and to predict when and how much iron sulfide scale will form. However, software for such calculation is very rare, considering the complex chemistry of iron sulfide and lack of experiment data.

Therefore, more researches are definitely required to achieve better iron sulfide prevention strategies.

2.3.3.2. Iron sulfide removal

If iron sulfide scale unfortunately forms, it is essential to remove it so as to restore oil production. There are two ways, mechanical removal and chemical dissolution.

For mechanical removal, a fluidic oscillation technology cleaning device (Ramachandran 2015; Webb 2006) and a high pressure jetting tool with a down hole motor or turbine with mills (Bolarinwa 2012; Ramachandran 2015) have been testified to be able to remove iron sulfide scales.

For chemical dissolution, three reagents have been reported to be effective to a certain degree. Firstly, strong mineral acid (e.g. hydrochloric acid (HCl)), is a traditional chemical to dissolve iron sulfide scale, which is often called acid treatment. HCl can easily dissolve most forms of iron sulfide, except pyrite, but HCl can also bring severe troubles to oil wells. HCl can cause high yield of H_2S in a short term, which may cause safety problem and environmental issues. HCl is also very corrosive, so H_2S scavengers and iron control agents are suggested to add into HCl. However, iron control agents and H_2S scavengers will interfere HCl dissolving iron sulfide (Ramachandran 2015).

Secondly, tetrakis(hydroxymethyl) phosphonium sulfate (THPS) has been reported as an iron sulfide dissolver (Kelland 2014). A mixture of THPS and tris(hydroxymethyl) phosphine (THP) can achieve a higher dissolve efficacy, but THPS and THP have polymerization side reactions at low pH. To avoid the side reactions, ammonia or a small primary amine (e.g. methylamine) can

be added (Kelland 2014). THPS blending with diethylenetriamine-phosphonate can also improve the dissolution efficacy (Wylde 2014).

Thirdly, acrolein gas can dissolve iron sulfide scale as well as scavenge H_2S. It was applied successfully for iron sulfide and H_2S removal on onshore and offshore oil wells (Salma 2000). However, acrolein is toxic and is a strong irritant for the skin, eyes, and nasal passages (Arntz 2012), which impedes the wide application of acrolein.

Chapter 3. Experimental Methods[1]

3.1. Method principle

In a typical experiment, a ferrous ion solution (Fe(II) solution) and a sulfide solution (S(-II) solution) are prepared separately, and two solutions are mixed and injected into a plug flow reactor where iron sulfide (abbreviated as FeS hereafter) can precipitate and deposit on the reactor. With Fe(II) concentration significantly lower than S(-II) concentration, FeS precipitation has been found to be pseudo first order in Fe(II) concentration. Fe(II) and S(-II) reaction time is controlled by solution flow rate (Q, ml/min). FeS precipitation kinetics is obtained by measuring the remaining Fe(II) concentration in the effluent at different Q values. When Q is very low and further slowing does not change the effluent concentration, it is assumed that the effluent is at equilibrium with precipitated FeS solid.

There are three reasons for choosing plug flow reactor, instead of bottles, for this study. First, plug flow reactor can avoid gas phase, and all S(-II) are in the aqueous phase. Second, plug flow reactor can easily change solution residence time by altering solution flow rate. Third, plug flow reactor is more similar to oil pipelines than bottle reactor.

3.2. Apparatus and chemicals

The experimental apparatus is shown in Figure 3.1. Argon (Ar) gas was used to sparge dissolved oxygen from solutions and remove air from the apparatus. The Ar is ultra-high purity argon (Matheson). An oxygen trap (Supelco, model 503088) with indicator (Grace indicating oxy-trap 4004) was used to remove residual oxygen in Ar and ensure the final oxygen content is less than 1 ppb (μg/L). S(-II) solution was prepared with sodium sulfide ($Na_2S{\cdot}9H_2O$) (Sigma Aldrich, >

[1] This chapter is modified from paper, "A new approach to study iron sulfide precipitation kinetics, solubility and phase transformation", and the paper has been submitted.

99.99% trace metals basis) and sodium chloride (NaCl) (Sigma Aldrich, ACS reagent grade). Fe(II) solution was prepared with ferrous ammonium sulfate ($Fe(NH_4)_2(SO_4)_2 \cdot 6H_2O$) (Fisher, ACS reagent grade), acetic acid (Sigma Aldrich, > 99%), and NaCl. Acetic acid was used to neutralize Na_2S to H_2S, after the two feed solutions are mixed. Mixed solution pH was controlled by acetic acid and acetate. The acetic acid amount in Fe(II) solution depends on the designed Na_2S concentration and pH. NaCl was used for solution IS adjustment. Two syringe pumps (Teledyne ISCO 500D) (Figure 3.2) with flow rate accuracy of ± 0.01ml/min were used to deliver Fe(II) and S(-II) solutions separately.

Two types of plug flow reactors were used. One reactor was a glass column (0.66 cm ID, 1.13 cm OD) with either two C1018 carbon steel coupons, or a hastelloy C-276 alloy (HC-276) coupon and a C1018 carbon steel coupon sequentially placed inside the glass column, as shown in Figure 2. Coupon size was 2.54 cm long, 0.16 cm thick, and 0.50 – 0.55 cm wide. Table 3.1 displays the compositions of C1018 carbon steel and HC-276. The glass column length was adjusted to the length of two coupons (5.08 cm). Coupons were polished with 220, 400 and 800 grit SiC papers. By following NACE standard operation (RP 2005), coupons were cleaned by using toluene to remove residual oil in an ultrasonic cleaner and then using ethanol to wash out toluene. The second reactor was HC-276 tubing (0.076 cm ID, 0.16 cm OD, 17.78 cm length).

For temperature control, a water bath was used at $T < 100$ °C and a silicone oil bath was used at $T \geq 100$ °C. The accuracy of temperature control was ± 0.1 °C. A back-pressure regulator, set at $5.17*10^5$ Pa (75 psi), was used for pressure control. The connecting tubing was either HC-276 or polyetheretherketone (PEEK) tubing (0.076 cm ID, 0.16 cm OD), and both materials have low oxygen permeability. The effluent was collected for Fe(II) and S(-II) concentration measurement.

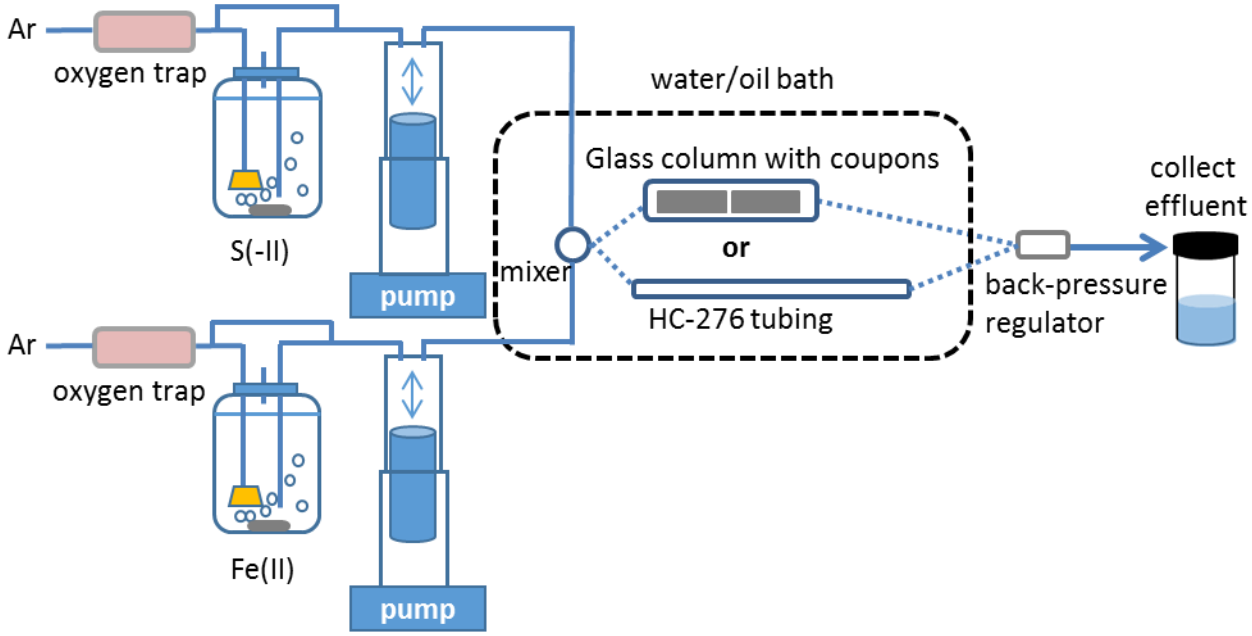

Figure 3.1. The experimental apparatus.

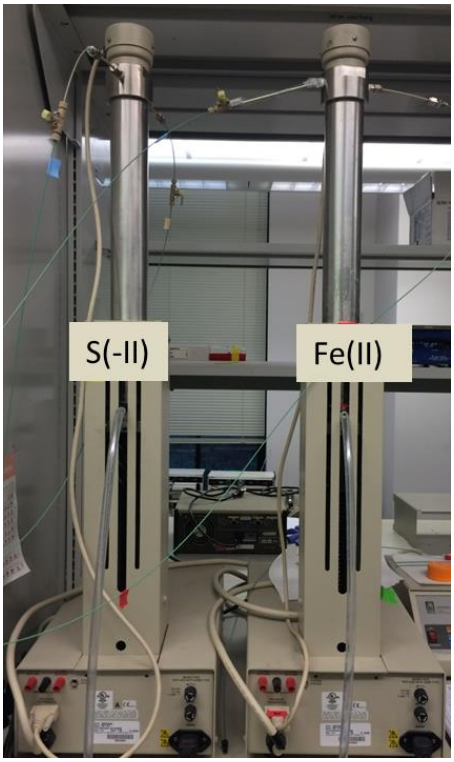

Figure 3.2. Two air tight syringe pumps.

Table 3.1. Compositions of C1018 carbon steel and Hastelloy C-276 alloy

C1018 carbon steel		Hastelloy C-276 alloy	
Element	Content	Element	Content
Carbon, C	0.14 - 0.20 %	Nickel, Ni	55%
Iron, Fe	98.81 - 99.26 %	Molybdenum, Mo	15 - 17 %
Manganese, Mn	0.60 - 0.90 %	Chromium, Cr	14.5 - 16.5 %
Phosphorous, P	≤ 0.040 %	Iron, Fe	4 - 7 %
Sulfur, S	≤ 0.050 %	Tungsten, W	3.0 - 4.5 %

3.3. Experimental procedure

3.3.1. Solution preparation and iron sulfide precipitation

There are several steps for a typical FeS experiment. First, 500 ml Fe(II) solution and 500 ml S(-II) solutions were freshly prepared to avoid oxidation, and then sparged with Ar (oxygen content < 1 ppb) for 40 min to remove the any dissolved oxygen. Previous tests (CHEMets dissolved oxygen R-7518) showed that this procedure produced solution has less than 1 ppb dissolved oxygen. Furthermore, Hach colorimetric measurement of Fe(II) and S(-II) after the sparging procedure confirmed their concentrations to be within about ±2% or better of the expected values. Meanwhile, Ar was blown through the apparatus for 1 h to remove air. Once the apparatus and the Fe(II) and S(-II) solutions were oxygen free, the Fe(II) and S(-II) solutions were separately pulled into their respective syringe pumps. After filling the two pumps, the solutions were pumped into the reactor and mixed in the mixer. The mixed solution is referred to as "influent." The reaction time was controlled by the flow rate, Q.

Before FeS precipitation kinetic measurements, the reactor was pre-coated with an FeS film by pumping the influent through the reactor for 12 h at Q = 0.1 ml/min. After finishing the coating, FeS precipitation kinetic measurements were conducted by measuring the remaining Fe(II)

concentration in the effluent at different flow rates, 0.1, 0.2, 0.5, 1, 2, 5, and 10 ml/min. S(-II) concentration in the effluent at low Q values (i.e. 0.1, 0.2, and 0.5 ml/min) were also measured for iron sulfide solubility calculation. Meanwhile, the effluent pH is measured by Accumet XL15 pH meter to be used in FeS solubility calculations.

3.3.2. Effluent collection and measurements

3.3.2.1. Fe(II) measurement

To measure Fe(II) concentration, 0.2 – 0.6 ml effluent is collected and immediately filtered to remove the suspended FeS particles. Two types of filters are used in effluent filtration. When effluent IS > 0.12 mol/kg, formed FeS particles is large and 0.45 μm cellulose acetate filters can filter out all FeS particles. When effluent IS ≤ 0.12 mol/kg, formed FeS particles size are very small and only 0.22 μm polyethersulfone millipore filters can filter them out. The filtrate is immediately diluted with 10 ml 0.001 mol/L hydrochloric acid (HCl) to quench any further reaction. Three effluent samples are collected at each flow rate. The 1,10-phenanthroline method is used for Fe(II) measurement, with detection range of 0.02 – 3 mg/L Fe(II). This method is based on the principle that 1, 10 phenanthroline reacts with Fe(II) to form an orange color in proportion to Fe(II) concentration (Hach 2002). A standard curve has been made to test the accuracy of this method (Figure 3.3). From test results, this method is acceptable for Fe(II) measurement in this study.

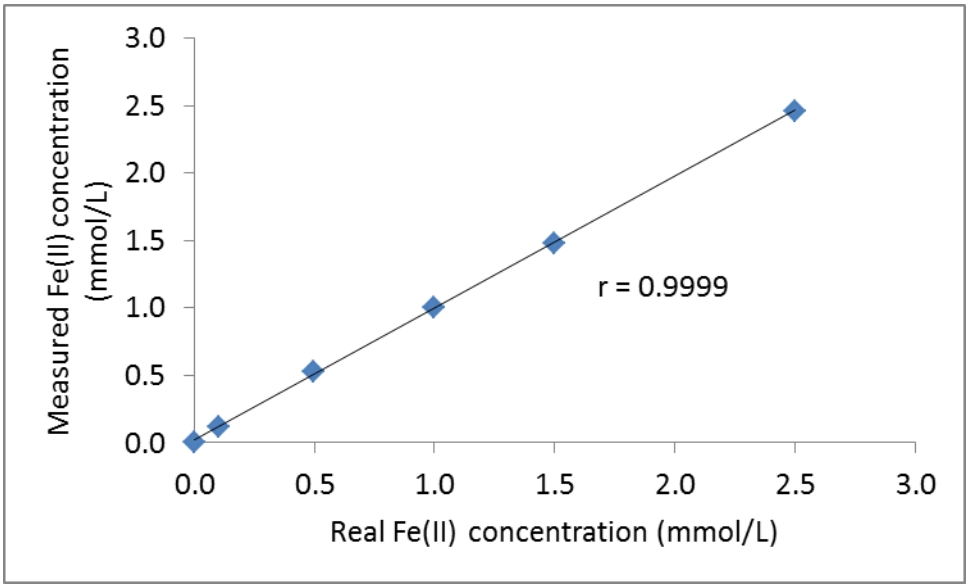

Figure 3.3. Standard curve of Fe(II) measurement by1,10-phenanthroline method.

3.3.2.2. S(-II) measurement

To measure S(-II) concentration in the effluent, the effluent is diluted with 0.004 mol/L EDTA solution at pH = 10, in which Fe(II) is chelated by EDTA and the S(-II) is converted to predominantly HS^-. Methylene blue method is used for S(-II) measurement, with detection range of 5 – 800 µg/L. Usually 0.02 – 0.04 ml effluent is diluted with 25 ml EDTA solution. In methylene blue method, all S(-II) are firstly converted to H_2S by strong acid, and then H_2S reacts with N,N-dimethyle-p-phenylenediamine sulfate to form methylene blue (equation 3.1). MB^+ is the dominant formed methylene blue species and has peak adsorption at 664 nm. S(-II) concentration is calculated based on the adsorption of MB^+ at 664 nm in spectrophotometer (Hach 2002).

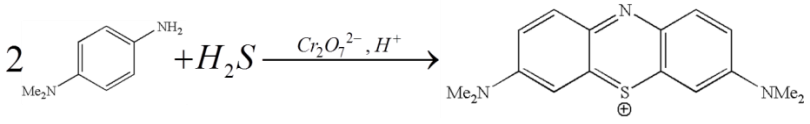

(3.1)

It should be noted that the methylene blue method is very sensitive to solution IS, which is found by this study. Methylene blue method was used to measure the S(-II) concentrations of several solutions which contains same amount of S(-II), 420 μg/L, but these solutions have different IS. As shown in Figure 3.4, the higher the IS, the lower the measured S(-II) concentration is. The mechanism behind this phenomenon is that IS can alter formed methylene blue species. At high IS, a significant portion of MB^+ becomes MBH_2^+, and MBH_2^+ has peak adsorption at 741 nm, not 664 nm. As the adsorption at 664 nm decreases, the calculated S(-II) concentration will correspondingly decrease. Therefore, in order to measure S(-II) accurately, effluent must be diluted with DI water to IS < 0.1 mol/L.

A standard curve was made to test the accuracy of methylene blue method (Figure 3.5), and this method turned out to be acceptable for S(-II) measurement.

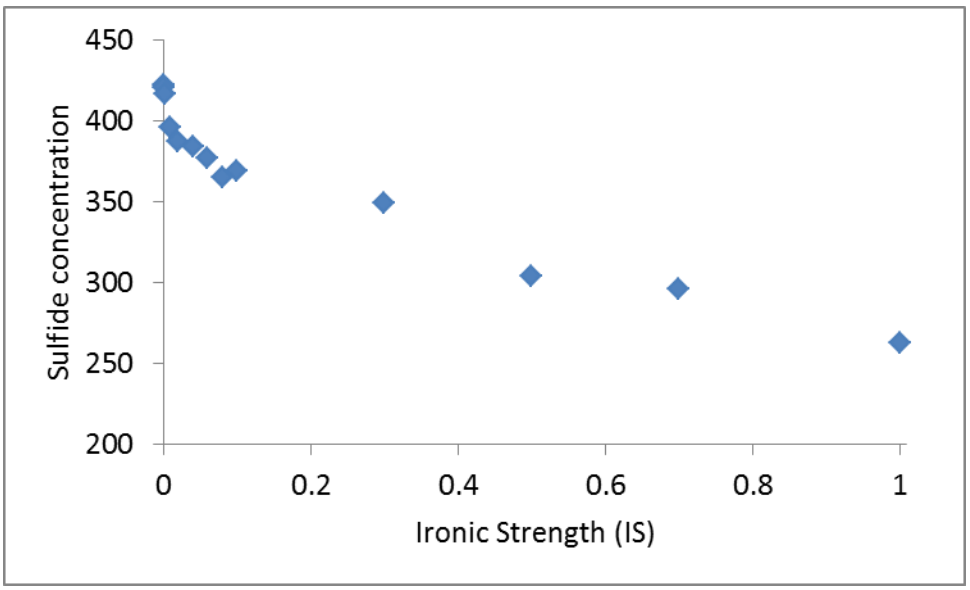

Figure 3.4. Ionic strength effect on S(-II) measurement by methylene blue method.

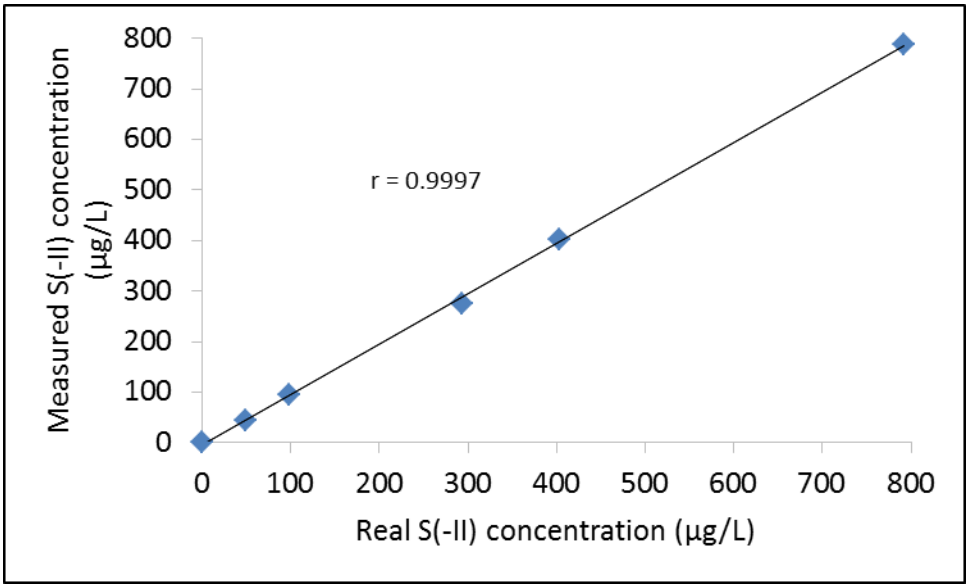

Figure 3.5. S(-II) standard curve measured by methylene blue method.

3.3.3. Iron sulfide characterization

The freshly precipitated FeS in the effluent and the deposited FeS retained on coupons in the reactor were analyzed by X-ray Diffraction (XRD) and Scanning Electron Microscope with Energy-dispersive X-ray spectroscopy (SEM / EDX).

To obtain freshly precipitated FeS, 20 ml effluent was collected in an oxygen free glass bottle under anoxic conditions, leaving minimal head space. The collection bottle was then allowed to stand in the water / oil bath where the reactor was placed, and the suspended FeS particles in the collected effluent settled down. After the FeS particles settled, the supernatant was removed with a syringe and the settled FeS particles were dried in a liquid nitrogen freeze drier. Powder X-ray diffraction was used to determine the phase of the FeS particles.

For the FeS retained on the coupons, after a FeS precipitation experiment was finished, Ar was blown through the glass column reactor for 12 – 24 h to dry the coupons. After the coupons were completely dry, the glass column reactor with both ends sealed was taken into a glove box and

then the coupons were removed. The coupons were placed in an oxygen-free bottle and kept in the glove box until XRD and SEM examination. Grazing Incidence X-ray diffraction was used to determine the phase of the FeS retained on the coupons.

3.3.4. H_2S corrosion and FeS scale retention evaluation

For experiments conducted in GC C1018 reactor, H_2S corrosion and FeS scale retention on C1018 coupons were evaluated. H_2S corrosion is evaluated by corrosion rate (CR) (equation 3.2). FeS scale retained on the coupon is evaluated by scale retention rate (SR) (equation 3.3). In order to determine CR and SR values, the FeS scale retained on C1018 coupon surface was removed by Clarke's solution, which is recommended by ASTM G1-03 standard (Standard 2004). Clarke's solution is made of 1000 mL hydrochloric acid (specific gravity 1.19), 20 g antinomy trioxide (Sb_2O_3) and 50 g stannous chloride ($SnCl_2$). Coupon mass are measured when coupon are completely dried.

$$CR\left(mm/year\right)=\frac{\left(W1-W3\right)\times 8.76\times 10^4}{\rho_{coupon}\cdot S\cdot t} \tag{3.2}$$

$$SR\left(mm/year\right)=\frac{\left(W2-W3\right)\times 8.76\times 10^4}{\rho_{FeS}\cdot S\cdot t} \tag{3.3}$$

$W1\,(g)$: *coupon mass before experiment*
$W2\,(g)$: *coupon mass after experiment with FeS scale on the surface*
$W3\,(g)$: *coupon mass after its surface FeS is removed by Clarke's solution*
$\rho_{coupon}(g/cm^3)$: *coupon density*, 7.87 g/cm^3
$\rho_{FeS}(g/cm^3)$: *mackinawite density*, 4.17 g/cm^3
$S\ (cm^2)$: *coupon surface area*
$t\ (h)$: *experimental time*

3.3.5. Experimental condition summary

Table 3.2 summarizes the experimental conditions of all experiments. "Initial SI" refers to the calculated (by our software ScaleSoftPitzer (SSP), see below for details) saturation index (SI) of FeS in the influent before FeS precipitation. SI is the decimal logarithm of the ratio of ion activity product to the solubility product (equation 3.4). In this study, the SI of FeS generally refers to the SI of mackinawite, unless stated otherwise. In equation 3.4, the units of $\left[Fe^{2+}\right]$, $\left[HS^{-}\right]$, and a_{H^+} are molality. Other concentration and activity units (e.g. mg/L or mol/L) will be converted to molality using solution density in SI calculation and this conversion is done internally in SSP. As shown in Table 3.2, the tested temperature ranges from 23 to 125 °C; IS ranges from 0.00886 to 5.03 mol/kg; pH ranges from 4.27 to 5.05; three Fe(II) to S(-II) concentration ratios were tested.

$$SI = \log_{10}\left(\frac{\left[Fe^{2+}\right]\left[HS^{-}\right]\gamma_{Fe^{2+}}\gamma_{HS^{-}}}{a_{H^+}K_{sp}}\right) \tag{3.4}$$

Table 3.2. Summary of experimental conditions.

Experiment number	Reactor[1,2,3]	T (°C)	IS (molality)	Initial pH[4]	$\left[Fe(II)\right]_0$ [5] (mmol/L)	$\left[S(-II)\right]_0$ [6] (mmol/L)	[Fe(II)] / [S(-II)] ratio[7]	Initial SI
1	GC C1018[1]	23	2.05	4.40	1.05	21.00	1:20	0.32
2	GC C1018	23	0.0193	4.80	0.41	8.20	1:20	0.30
3	GC C1018	50	0.0141	4.81	0.30	6.00	1:20	0.30
4	GC C1018	60	0.0118	4.82	0.25	5.00	1:20	0.29
5	GC C1018	70	0.00886	4.83	0.19	3.80	1:20	0.25
6	GC C1018	70	0.118	4.72	0.38	7.60	1:20	0.29
7	GC C1018	70	2.03	4.44	0.70	14.00	1:20	0.27
8	GC C1018	70	4.03	4.36	0.70	14.00	1:20	0.44
9	GC C1018	70	5.03	4.36	0.72	14.40	1:20	0.60
10	GC C1018	70	2.03	4.27	0.78	15.50	1:20	0.04

11	GC C1018	70	2.04	4.27	1.55	15.50	1:10	0.34
12	GC C1018	70	2.05	4.27	3.10	15.50	1:5	0.64
13	GC C1018	70	2.03	4.44	0.00	14.00	0.00	0.00
14	GC HC-276 and C1018[2]	70	0.00886	4.83	0.19	3.80	1:20	0.25
15	HC-276[3]	23	2.05	4.35	1.05	21.00	1:20	0.23
16	HC-276	23	2.05	4.35	2.10	21.00	1:10	0.53
17	HC-276	23	2.07	4.35	4.20	21.00	1:5	0.83
18	HC-276	70	1.03	4.51	1.00	10.00	1:10	0.29
19	HC-276	70	2.03	4.36	0.83	15.50	1:18.6	0.24
20	HC-276	70	2.04	4.36	1.55	15.50	1:10	0.51
21	HC-276	70	2.05	4.36	3.10	15.50	1:5	0.81
22	HC-276	70	2.01	5.05	0.21	4.20	1:20	0.32
23	HC-276	100	1.02	4.46	1.00	10.00	1:10	0.50
24	HC-276	100	2.03	4.37	1.20	12.00	1:10	0.56
25	HC-276	125	2.03	4.34	1.00	10.00	1:10	0.57
26	GC 1018	60	0.0275	4.59	1.20	12.00	1:10	0.53
27	GC 1018	60	0.0275, with 100 mg/L dispersant	4.59	1.20	12.00	1:10	0.66

[1]GC C1018: glass column reactor with two C1018 coupons inside.

[2]GC HC-276 and C1018: glass column reactor with a HC-276 coupon followed by a C1018 coupon inside.

[3]HC-276: HC-276 tubing reactor.

[4]pH: it is the pH reading that would be on a pH meter with the junction potential included.

[5]$\left[Fe(II)\right]_0$: the initial Fe(II) concentration of the influent before reacting with S(-II).

[6]$\left[S(-II)\right]_0$: the initial S(-II) concentration of the influent before reacting with Fe(II).

[7][Fe(II)] / [S(-II)] ratio: the concentration ratio of initial Fe(II) to initial S(-II).

Initial SI: the saturation index (SI) of FeS in the influent before FeS precipitation happens.

Chapter 4. Results and Discussions[2]

4.1. FeS precipitation kinetics

Freshly precipitated FeS was collected in experiments 15, 19, and 24 at 23, 70, and 100 °C, respectively. The collected FeS samples were analyzed by XRD and SEM. XRD results showed that the freshly precipitated FeS was mackinawite at these temperatures, consistent with early studies (Bai 2015; Ma 2000; Sun 2006). Figure 4.1 shows the XRD result of experiment 15, and Figure 4.2 shows the SEM image. From this, it is proposed that the freshly precipitated FeS phase is mackinawite.

[2] This chapter is modified from two papers. One is "Iron Sulfide Precipitation and Deposition under Different Impact Factors" published in SPE International Conference on Oilfield Chemistry held in Montgomery, Texas, USA, 3 - 5 Apr 2017. (paper number: SPE 184546). The other paper is "A new approach to study iron sulfide precipitation kinetics, solubility and phase transformation" and it has been submitted.

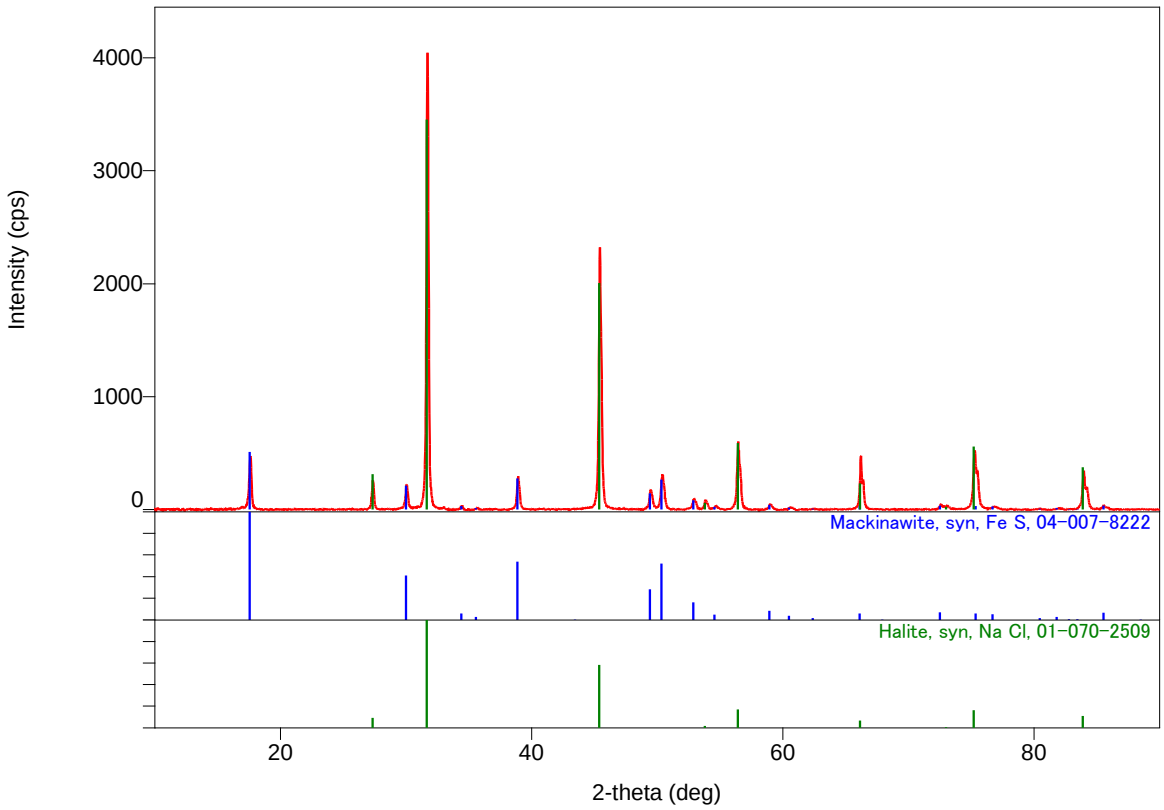

Figure 4.1. XRD pattern of freshly precipitated FeS from experiment 15.

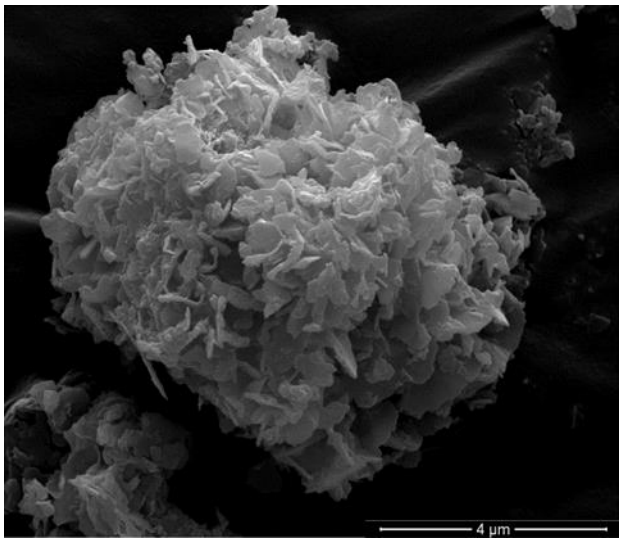

Figure 4.2. SEM image of freshly precipitated FeS from experiment 15 (identified as mackinawite by XRD).

According to Rickard (Rickard 1995), in acidic condition, Fe(II) directly reacts with H_2S to form FeS and $2H^+$. In this study, the pH is in the range of 4.27 – 5.05, such that FeS precipitation reaction might be written as equation 4.1. Also, in such acidic conditions, H_2S concentration is approximately equal to total S(-II) concentration. Since Fe(II) concentration is significantly lower than S(-II) concentration, FeS precipitation is assumed to be a pseudo first order reaction, and the precipitation rate is expressed as equation 4.2. In equation 4.2, k_{1st} is the first order reaction rate constant; $\left[Fe(II)\right]_t$ is the remaining Fe(II) concentration at time t; $\left[Fe(II)\right]_{eq.}$ is the Fe(II) concentration at equilibrium with the precipitated FeS solid.

$$Fe^{2+} + H_2S \rightarrow FeS + 2H^+ \tag{4.1}$$

$$\frac{d\left[FeS\right]}{dt} = -\frac{d\left[Fe(II)\right]}{dt} = k_{1st}\left(\left[Fe(II)\right]_t - \left[Fe(II)\right]_{eq.}\right) \tag{4.2}$$

The precipitation kinetics of FeS are generally reported to be fast (Rickard 1995). In equation 4.2, k_{1st} can be replaced by the corresponding heterogeneous mass transfer term, $k_{1st} = k_m A/V$, and reaction time t is replaced with $t = V/Q$. By Integrating equation 4.2, the equation of Fe(II) concentration as a function of Q is obtained (equation 4.3). Figure 4.3 shows an example of experimental data fitted to equation 4.3, and the correlation coefficient r = 0.9964. In equation 4.3, $\left[Fe(II)\right]_Q$ is the remaining Fe(II) concentration in the effluent at flow rate Q; $\left[Fe(II)\right]_0$ is the initial Fe(II) concentration in the inlet mixing solution before reacting with S(-II); A is coupon or tubing surface area coated with freshly precipitated FeS; V is the reactor volume. As observed in

the experiments, C1018 coupon, HC-276 coupon, and HC-276 tubing can be coated with precipitated FeS (evidence provided later), but a glass column cannot be readily coated. This is why A only counts coupon or tubing surface area depending on reactor type. The term "A/V" is the ratio of FeS contact surface area to solution volume.

$$[Fe(II)]_Q = [Fe(II)]_{eq.} + \left([Fe(II)]_0 - [Fe(II)]_{eq.}\right) \cdot e^{-k_m A/Q}$$
$$k_{1st} = k_m A/V,\ t = V/Q,\ with\ \ln k_m = \ln A' + E_a/(RT) \qquad (4.3)$$

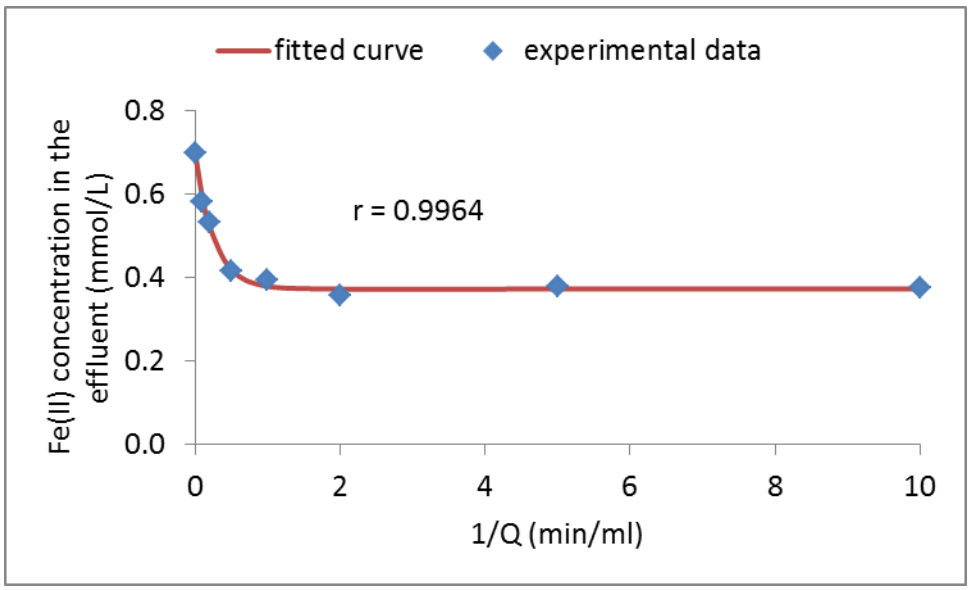

Figure 4.3. The remaining Fe(II) concentration in the effluent changes with solution flow rate (Q) in FeS precipitation experiment.

In Figure 4.3, when 1/Q is low, the time for reaction of Fe(II) and S(-II) is short, and the effluent is not at equilibrium and is still clear or only slightly grey in color. When 1/Q is high, the reaction time for Fe(II) and S(-II) is sufficient for complete FeS precipitation, and the Fe(II) concentration in the effluent is at equilibrium with precipitated FeS. In this case, the effluent is grey to dark color with noticeable FeS particles.

The influence of different reactors (i.e. glass column reactor with coupons inside and HC-276 tubing reactor), temperature, IS, and [Fe(II)] / [S(-II)] ratio on the FeS precipitation kinetics were investigated. Table 4.1 summarizes the experimental results. The correlation coefficient of experimental data and fitted curve are in the range of 0.9800 – 0.9999 for individual experiments. The covariance between the calculated $\left[Fe(II)\right]_{eq.}$ and k_m values were typically only 0.55, suggesting that these two terms are independent, as would be suggested from Figure 4.3.

Table 4.1. Summary of experimental results.

Experiment number ()	pH at equilibrium[1]	$\left[Fe(II)\right]_{eq.}$[2] (mmol/L)	SI at equilibrium[3]	k_m (m/s)
1	4.40	0.7982 ± 0.0050	0.17	3.61E-05 ± 2.82E-06
2	4.79	0.2526 ± 0.0079	0.02	1.32E-05 ± 2.27E-06
3	4.80	0.1790 ± 0.0030	0.01	2.52E-05 ± 2.00E-06
4	4.81	0.1552 ± 0.0045	-0.01	3.69E-05 ± 7.15E-06
5	4.82	0.1380 ± 0.0048	-0.03	3.44E-05 ± 9.53E-06
6	4.71	0.2474 ± 0.0015	0.02	5.12E-05 ± 2.07E-06
7	4.43	0.3734 ± 0.0070	-0.09	8.83E-05 ± 7.27E-06
8	4.34	0.2503 ± 0.0121	-0.08	1.17E-04 ± 1.18E-05
9	4.33	0.1937 ± 0.0152	-0.04	1.63E-04 ± 2.06E-05
10	4.27	0.6100 ± 0.0168	-0.13	6.46E-05 ± 6.93E-06
11	4.25	0.7594 ± 0.0258	-0.08	3.88E-05 ± 4.90E-06
12	4.22	1.4827 ± 0.0321	0.12	1.24E-04 ± 1.01E-05
13	4.43	N/A	N/A	N/A
14	4.82	0.1380 ± 0.0048	-0.03	N/A
15	4.35	0.7317 ± 0.0130	0.06	3.92E-05 ± 4.17E-06
16	4.34	1.5252 ± 0.0159	0.35	2.38E-05 ± 2.37E-06
17	4.31	2.6499 ± 0.1011	0.48	3.18E-05 ± 7.38E-06
18	4.49	0.7402 ± 0.0112	0.12	7.00E-05 ± 1.17E-05
19	4.35	0.5952 ± 0.0094	0.07	8.30E-05 ± 1.24E-05
20	4.34	1.1169 ± 0.0053	0.33	9.47E-05 ± 6.62E-06
21	4.32	2.0750 ± 0.0279	0.54	7.75E-05 ± 7.77E-06
22	5.04	0.1406 ± 0.0028	0.12	7.02E-05 ± 1.01E-05

23	4.43	0.4675 ± 0.0149	0.10	N/A
24	4.35	0.6916 ± 0.0330	0.24	1.17E-04 ± 3.08E-05
25	4.31	0.3651 ± 0.0275	0.10	1.59E-04 ± 2.72E-05
26	4.56	0.5286 ± 0.0007	0.35	3.87E-05 ± 2.12E-06
27	4.56	N/A	N/A	N/A

[1]pH at equilibrium: the pH of the effluent at equilibrium with precipitated FeS solid. pH at equilibrium is usually 0.1 – 0.3 lower than initial pH, which is due to the released proton (H^+) by FeS precipitation.

[2]$\left[Fe(II)\right]_{eq.}$: the Fe(II) concentration of the effluent at equilibrium with precipitated FeS solid.

[3]SI at equilibrium: the saturation index of FeS of the effluent at equilibrium.

4.1.1. Effect of different reactors

Two types of reactors, glass column with coupons and HC-276 tubing, were tested to determine whether the kinetics were a function of the reactor type. One comparison is with experiments 1 and 15, at 23 °C. The other is with experiments 7 and 19, at T = 70 °C. FeS precipitation kinetics is evaluated by comparing k_m (m/s) values. As shown in Table 4.1 and Figure 4.4, the k_m values of experiments 1 and 15 are $3.61\times10^{-5} \pm 2.82\times10^{-6}$ and $3.92\times10^{-5} \pm 4.17\times10^{-6}$, respectively, and these two values, and these two values do not differ significantly, same with experiments 7 and 19. Therefore, it seems that these specific reactor configurations do not significantly affect FeS precipitation kinetics.

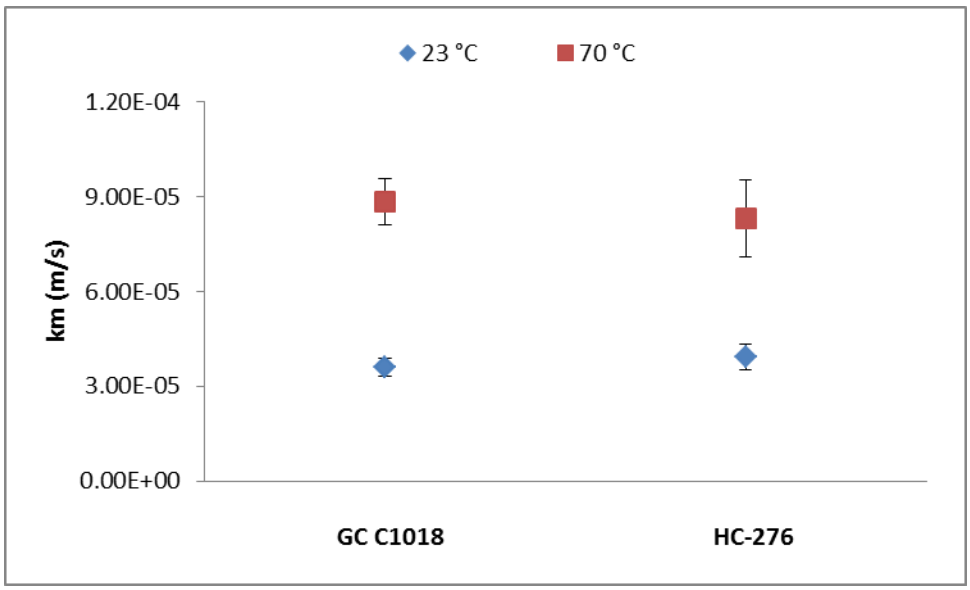

Figure 4.4. The FeS precipitation kinetics (indicated by k_m) measured in different reactors. (T = 23 or 70 °C, IS = 2.03 – 2.05 mol/kg, pH = 4.35 – 4.44)

Each reactor was coated with fresh FeS layer before the precipitation kinetics measurement. C1018 carbon steel coupon can be corroded by H_2S, and a thick FeS layer can form on the coupon surface, as shown in Figure 4.5, left. The FeS comes from both corrosion and aqueous precipitation. HC-276 is a corrosion resistant alloy, and the initial coating FeS layer on HC-276 tubing inner surface comes only from aqueous precipitation (Figure 4.5, right). The FeS layer on HC-276 tubing is thinner than the one on the C1018 coupon. Despite the differences in the source of the initial FeS coating and the thickness of the coating, at same temperature the measured k_m values in these two types of reactors are similar (Figure 4.4).

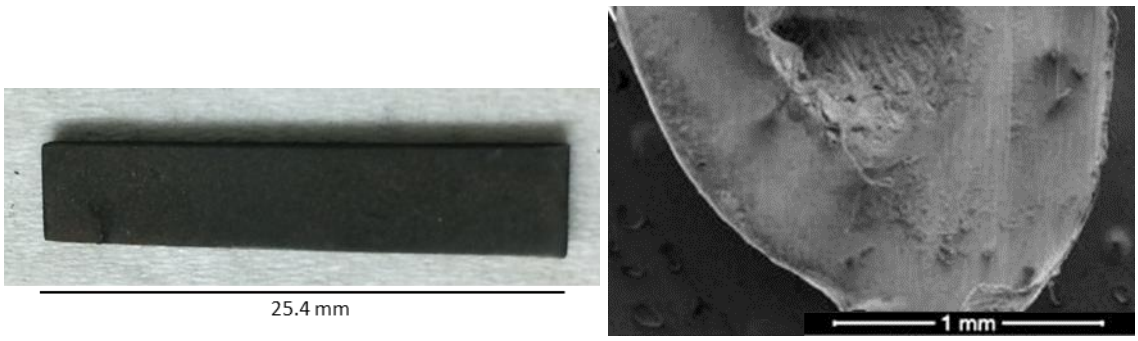

Figure 4.5. C1018 coupon (left) and HC-276 tubing (right), both coated with a FeS layer.

4.1.2. Effect of Fe(II) to S(-II) concentration ratio

The effect of [Fe(II)] / [S(-II)] concentration ratio on FeS precipitation kinetics were tested at both 23 °C (experiments 15 – 17) and 70 °C (experiments 19 – 21), with IS = 2.03 – 2.07 mol/kg and pH = 4.35 – 4.36. There were three [Fe(II)] / [S(-II)] ratios, 1:20, 1:10, and 1:5, in which only Fe(II) concentration was changed and other conditions, including S(-II) concentration, were kept constant. Based on ANOVA analysis (two-factor without replication), there is no significant difference in the k_m values at different [Fe(II)] / [S(-II)] ratios at the same temperature ($P = 0.84$) (Figure 4.6), even though the initial SI values changed from 0.23 (experiment 15) to 0.83 (experiment 17). Also, there is significant difference in the k_m values at different temperature ($P = 0.026$), as expected. Therefore, the [Fe(II)] / [S(-II)] ratio change at range of 1:20 to 1:5 does not significantly affect FeS precipitation kinetics. These observations further confirm the k_m model suggested in equation 4.3.

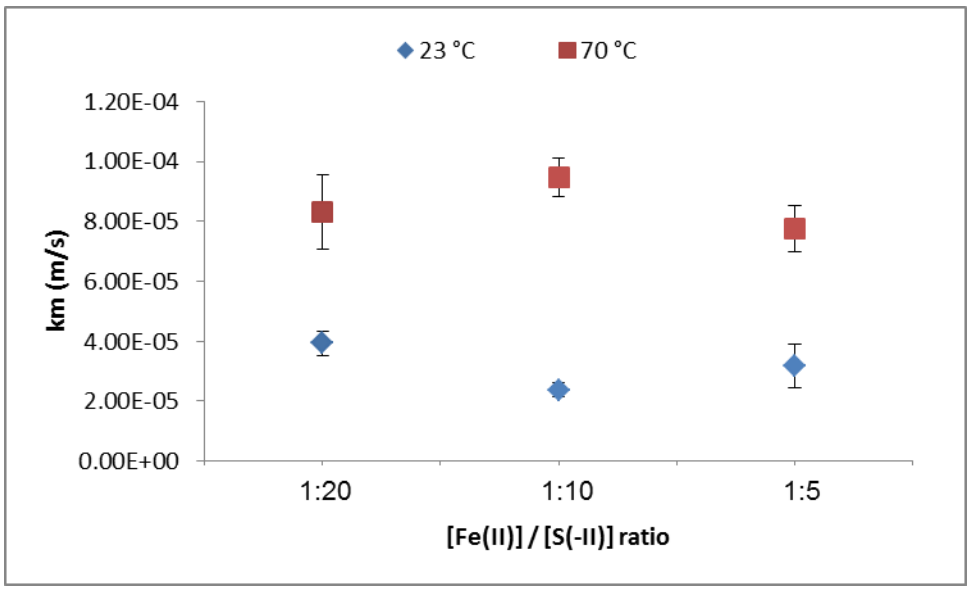

Figure 4.6. The FeS precipitation kinetics (indicated by k_m) at different [Fe(II)] / [S(-II)] ratios. (T = 23 or 70 °C, IS = 2.03 – 2.07 mol/kg, pH = 4.35 – 4.36)

4.1.3. Effect of temperature

Temperature effects on FeS precipitation kinetics were tested at temperature of 23, 70, 100, and 125 °C, IS = 2.03 – 2.07 mol/kg, and pH = 4.35 – 4.44 (experiments 1, 7, 15 - 17, 19 - 21, 24 and 25). When temperature increases from 23 °C to 125 °C, the average k_m value increases about 5 times, from 3.27×10^{-5} m/s to 1.59×10^{-4} m/s. Temperature increase can significantly accelerate FeS precipitation. This phenomenon is also typical for other mineral precipitations, such as barite ($BaSO_4$) and celestite ($SrSO_4$) (He 1995a; 1995b). Using the Arrhenius equation and the k_m at different temperatures (Figure 4.7), the calculated activation energy (E_a) is 15.12 ± 0.85 kJ/mol with a correlation coefficient r = 0.9969. The natural logarithm of the fitted pre-exponential factor is 4.15 ± 0.29. Such a low activation energy value implies that FeS precipitation is diffusion controlled (Fogler 2008). Additionally, the goodness of the fit implies that the model suggested in equation 4.3 is reasonable.

Only a few studies on the precipitation rate of FeS have been reported. Rickard measured FeS precipitation rate at 25 °C and pH from 6.4 to 9.9 (Rickard 1995). To compare the precipitation rates measured by this study and by Rickard, second order reaction rate constant (k_{2nd}) is needed. Based on Rickard's measurement, k_{2nd} is in the range of 1.5 – 15 L/(mol·s) at 25 °C. In this study, $k_{2nd} = k_m A/V[H_2S]$. Due to the differences in surface area and reactor volume of two types of reactors, the k_{2nd} in glass column reactor and HC-276 reactor at 23 °C are calculated to be 1.0 ± 0.1 and 5 ± 1 L/(mol·s), respectively, which is reasonably consistent with the rate data from Rickard at 25 °C. No other data on the temperature dependence of mackinawite, or similar FeS, is known for comparison.

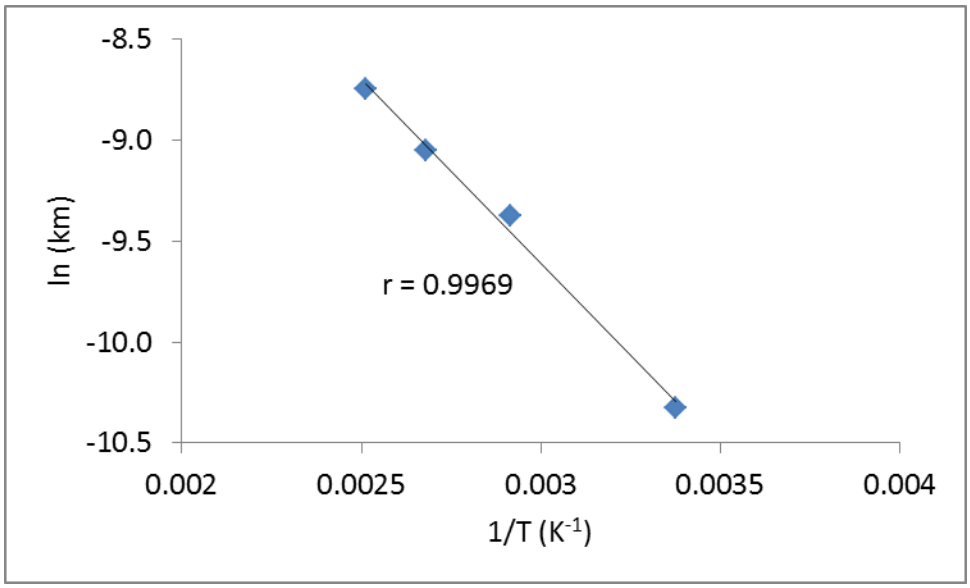

Figure 4.7. The natural logarithm of k_m at different temperature is plotted against the reverse of temperature (Arrhenius equation). (T = 23, 70, 100, and 125 °C, IS = 2.03 – 2.07 mol/kg, and pH = 4.35 – 4.44)

4.1.4. Effect of ionic strength

IS effect on FeS precipitation kinetics was tested at IS range of 0.00886 – 5.03 mol/kg, T = 70 °C and pH = 4.36 – 4.81 (experiments 5 – 9 and 18). The reported pH is due to a combination of the junction potential and activity coefficients, both caused by changes in IS, in that the ratio of Ac^-/HAc was the same in all experiments. At IS = 0.00886 mol/kg, k_m is only 3.44×10^{-5} m/s; at IS = 5.03 mol/kg, k_m rises to 1.63×10^{-4} m/s. IS increase can significantly accelerate FeS precipitation. Previous research on calcite also shows that calcite nucleation rate increases with IS (Bischoff 1968).

Primary kinetic salt effect describes that the decimal logarithm of reaction rate is proportional to the square root of IS (Bronsted 1928), $\log_{10}(k_m) \propto \sqrt{IS}$. By plotting the logarithm of k_m against the square root of IS, the correlation coefficient is 0.9843. Therefore, primary kinetic salt effect may explain the phenomenon that IS accelerates FeS precipitation kinetics.

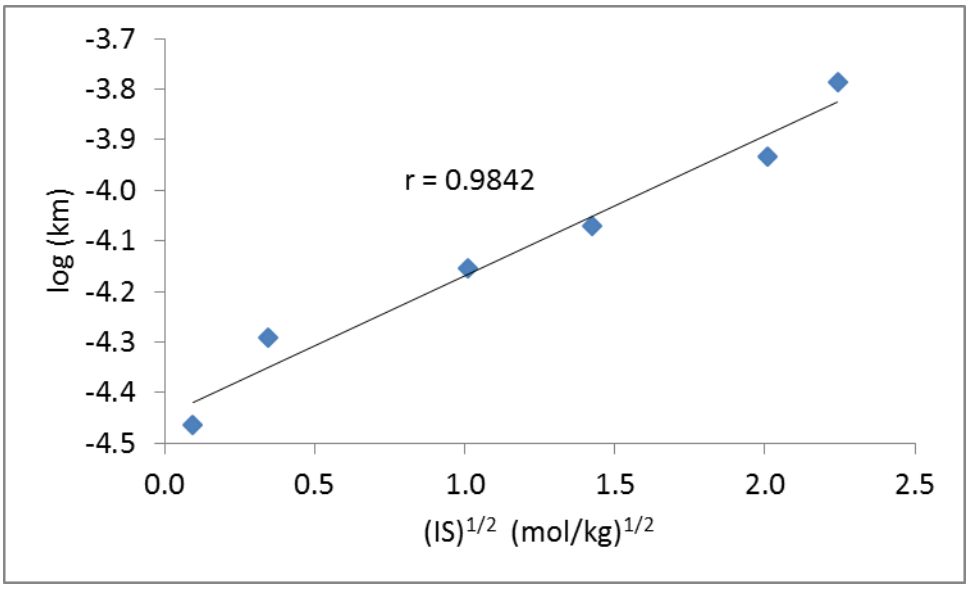

Figure 4.8. The logarithm of k_m is plotted against the square root of IS. (T = 70 °C, IS = 0.00886 – 5.03 mol/kg, pH = 4.36 – 4.81)

4.2. FeS solubility

4.2.1. Mackinawite solubility

As mentioned previously, when FeS precipitation is completed in the reactor at low Q, the Fe(II) and S(-II) concentrations in the effluent are taken to represent the solubility of FeS. Since the freshly precipitated FeS was identified to be mackinawite, the FeS solubility measured in this study is mackinawite solubility. Many previous studies showed that mackinawite is usually the first identified FeS phase to form in supersaturated Fe(II) and S(-II) aqueous solutions and in H_2S corrosion on steel under 100 °C (Benning 2000; Rickard 2006; Smith 2011). However, the pK_{sp} value for mackinawite has been reported to vary from 3.00 to 3.98 at 25 °C (Al-Farawati 1999; Davison 1999; Rickard 2007). This study measured the solubility of mackinawite at T = 23 – 125 °C, IS = 0.00886 – 5.03 mol/kg, and pH = 4.27 – 5.05. The solubility of mackinawite at the high ionic strengths used in this study, have never been reported nor modeled. With the data from this study and the solubility data from Rickard in the pH range of 3.16 to 6.13 (Rickard 2006), a model for predicting mackinawite solubility and precipitation was developed and incorporated in our software SSP.

In this model, the mackinawite K_{sp} and H_2S K_{a1} versus temperature data from Naomov were used (equations 4.4 and 4.5) (Naumov 1974). At 25 °C, equations 4.4 and 4.5 yield pK_{sp} = 3.54 and pK_{a1} = 6.98, respectively. The activity coefficients of Fe(II) and HS^- were calculated by Pitzer equations. The Pitzer coefficient β_2 values for Fe(II) interaction with Cl^- (-16.96), HS^- (-1633.4), Ac^- (-24.12), and SO_4^{2-} (-42) and the λ_{Fe,H_2S} (2.51) were determined by curve fitting the data in Table 4.1 (the data of experiments 13, 16, 17, 20, and 21 are excluded and see below for reasons) and the data from Rickard in the pH range 3.16 to 6.13 (Rickard 2006). As discussed in Dai's paper (Dai 2016), the version of Pitzer theory used in SSP does not include specific ion-pair (e.g.

$FeCl^+$, $FeHS^+$, $FeAc^+$, and $FeSO_4^0$) constants, but rather these specific-ion interactions are accounted for with the various coefficient values – note the large value for the β_2 terms. The remaining Pitzer ion interaction terms from SSP were used without modification (Dai 2016). Besides, the concentration of Fe(II) was measured in experiments, and the concentration of HS^- was calculated from the mass balance equation (equation 4.6), in which [S(-II)] represents the total sulfide concentration and its was measured in experiments.

$$pK_{sp} = -131.7569 + 6433.6172/T + 19.9617 * \ln(T) \tag{4.4}$$

$$pK_{a1} = -12.41 + 3539.1/T + 0.02522 * T \tag{4.5}$$

$$\left[HS^-\right] = \left[S(-II)\right] \Big/ \left(1 + \frac{a_{H^+}\gamma_{HS^-}}{K_{a1}\,\gamma_{H_2S}}\right) \tag{4.6}$$

The calculated SI values for the mackinawite solubility data from this study are plotted in Figure 4.9. The average SI value and the standard deviation were 0.031 ± 0.097. Similarly, the fit to the data published by Rickard in the pH range of 3.16 to 6.13 was 0.0053 ± 0.20 (Figure 4.10). These results imply that our model for mackinawite solubility prediction is reliable and can be used from 23 to 125 °C, from 0 to 5 mol/kg IS, and 3 (or lower) to 6.13 pH. At higher pH values, probably other iron species, e.g. FeS^0 and $Fe(HS)_2^0$, need to be considered to represent the solubility data of mackinawite (Davison 1999; Rickard 2006).

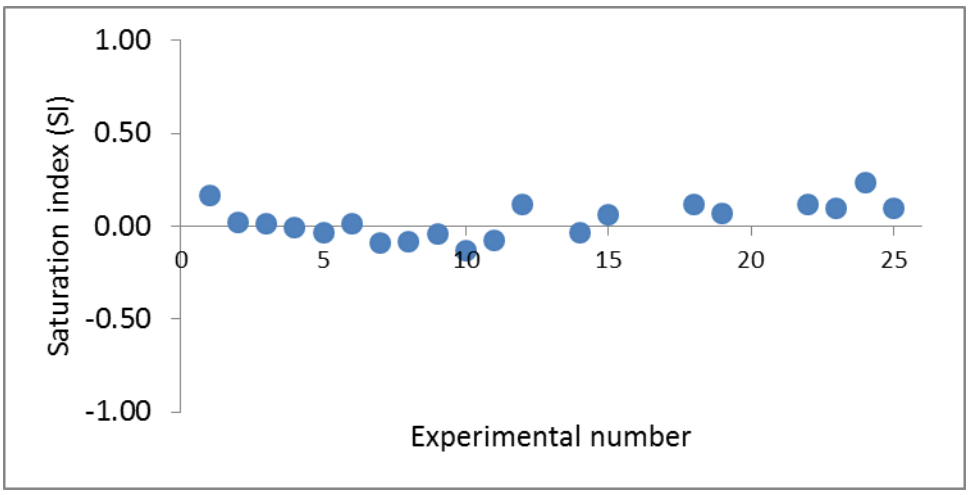

Figure 4.9. The calculated SI values of the effluents in experiments 1 – 25, except 13, 16, 17, 20, 21.

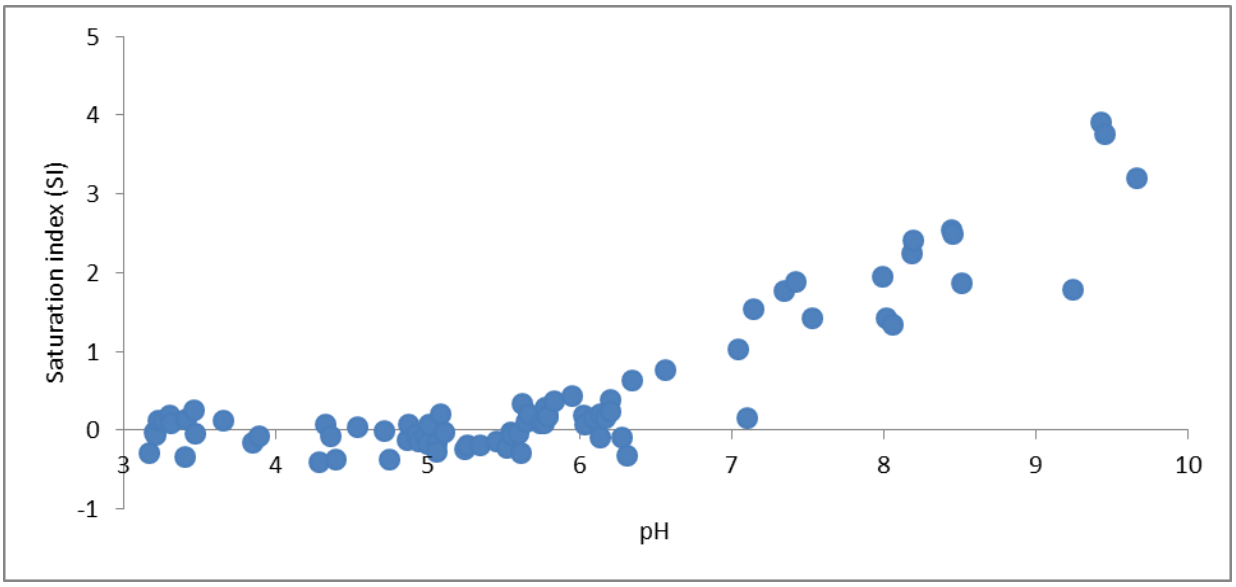

Figure 4.10. The SI values of literature mackinawite solubility data calculated by SSP.

Moreover, we used two other softwares, Visual Minteq and PHREEQC, to predict the SI of mackinawite solubility data of this study. Figure 4.11 shows a comparison of the SI values predicted by our model, Visual Minteq (version 3.1_beta), and PHREEQC. Two different databases, phreeqc.dat and minteq.v4.dat, were used in PHREEQC and they were noted as

PHREEQC(phreeqc) and PHREEQC(minteq.v4), respectively. The key parameters for SI calculation in those four models are shown in Table 4.2.

As shown in Figure 4.11, the SI predicted by PHREEQC(phreeqc) are larger than zero with an average value of 0.82, which is probably due to the low K_{sp} value (see Table 4.2). The K_{sp} in PHREEQC(phreeqc) is $10^{-4.65}$, which is one order of magnitude lower than those in the other three models ($10^{-3.55}$ – $10^{-3.60}$). According to Rickard and Luther's review on iron sulfide (Rickard 2007), the measured mackinawite pK_{sp} values in many previous researches are generally in the range of 3.0 to 3.98. It is unusual to for mackinawite $pK_{sp} = 4.65$. If the pK_{sp} in PHREEQC(phreeqc) is changed to 3.60, the value used in PHREEQC(minteq.v4), the predicted SI values will become much closer to zero with an average value of -0.23. Furthermore, according to the instruction of PHREEQC (USGS 1999), PHREEQC(phreeqc) uses Debye-Hückel expression for major ions activity coefficient calculation, which is applicable for solution with IS $\leq$ 2 mol/kg. Davis equation is used for most ion complexes, and it is applicable for solution with IS $\leq$ 0.5 mol/kg. However, most of the mackinawite solubility data of this study are measured at IS $\geq$ 2 mol/kg, and PHREEQC(phreeqc) considers a lot of Fe-complexes. This could also cause difference between the predicted SI and the ideal SI (zero).

Minteq.v4.dat in PHREEQC is a database derived from MINTEQA2 version 4, a software developed by United States Environmental Protection Agency (EPA). In PHREEQC(minteq.v4) prediction, for solubility data measured at low IS (0.00886 – 0.118 mol/kg) (i.e. experiment 2 – 6 and 14), the predicted SI are close to zero. However, for solubility data measured at high IS ($\geq$ 1 mol/kg), the predicted SI are significantly lower than zero. Interestingly, as IS increases 1 mol/kg, the predicted SI decreases about 1, as shown in Figure 4.11. This phenomenon is probably due to the activity coefficients of Fe^{2+} and HS^- are too low. For example, in experiment

1, the activity coefficient of Fe^{2+} calculated by PHREEQC(minteq.v4) ($8.41*10^{-4}$) is three orders of magnitude lower than those in the other three models (0.13 – 0.24). It seems unreasonable for Fe^{2+} to have such low activity coefficient in a solution with IS = 2.05 mol/kg. Also, the activity coefficient of HS^- (0.17) is about three times lower than the others (0.51 – 0.59). As stated in MINTEQA2 manuals (Allison 1991; HydroGeoLogic 1998), the modified Debye-Hückel equation is used to calculate activity coefficients for those species that have the necessary parameters in the database; otherwise, the Davies equation is used for activity coefficient calculation. If the user selects the Davies equation at the outset, then Davies equation will be used to calculate activity coefficients for all species. Unfortunately, we do not know which equation is used for activity coefficient calculation in PHREEQC(minteq.v4). But still, the calculated activity coefficients at high IS are significantly lower than those in the other models, leading to low SI predictions.

For Visual Minteq, the predicted SI values are generally around -1.0 with an average value of -1.14. The pK_{sp} and activity coefficients in Visual Minteq are in consistent with those in our model and PHREEQC(minteq.v4). As to considered Fe-complexes, a major difference is that Visual Minteq considers $FeHS^+$ complex, while PHREEQC(phreeqc) and PHREEQC(minteq.v4) consider $Fe(HS)_2$ and $Fe(HS)_3$ complexes. The chemical formula of the complex(es) of Fe^{2+} and HS^- is still in debate. In previous researches on $FeHS^+$ stability constant (ß) measurement, the measured log ß vary from 4.34 to 5.94 (Luther III and Ferdelman 1993; Zhang and Millero 1994; Wei and Osseo-Asare 1995; Luther, Rickard et al. 1996; Al-Farawati and van den Berg 1999), with an average of 5.2. Visual Minteq adopted 5.62 as the log ß of $FeHS^+$. However, such high stability constant ($10^{5.2}$) of $FeSH^+$ is inconsistent with mackinawite solubility measurement data, according to Rickard and Luther (Rickard 2006; A45). In details, if $FeSH^+$ exists and its log ß =

5.2, then mackinawite solubility should be two orders of magnitude higher than the experimentally measured value (pK_{sp} = 3.5). In Davison's experiment of iron sulfide solubility measurement, he assumed the existence of $FeHS^+$ and calculated the log ß of $FeSH^+$ with the solubility data, and it turns out log ß = 3.758 ± 0.111 (Davison, Phillips et al. 1999). We recalculated the log ß with Davison's data and log ß = 3.23. If we deliberately change the log ß of $FeSH^+$ to be 3.23 in Visual Minteq, then the calculated SI = -0.21 for experiment 1 of this study. Therefore, based on previous research and our observation, it is possible that the stability constant of $FeSH^+$ is lower than the directly measured values. It is also possible that $FeSH^+$ does not exist and the complex between Fe^{2+} and HS^- are $Fe(HS)_2$ and $Fe(HS)_3$. More investigation are needed to reveal the truth.

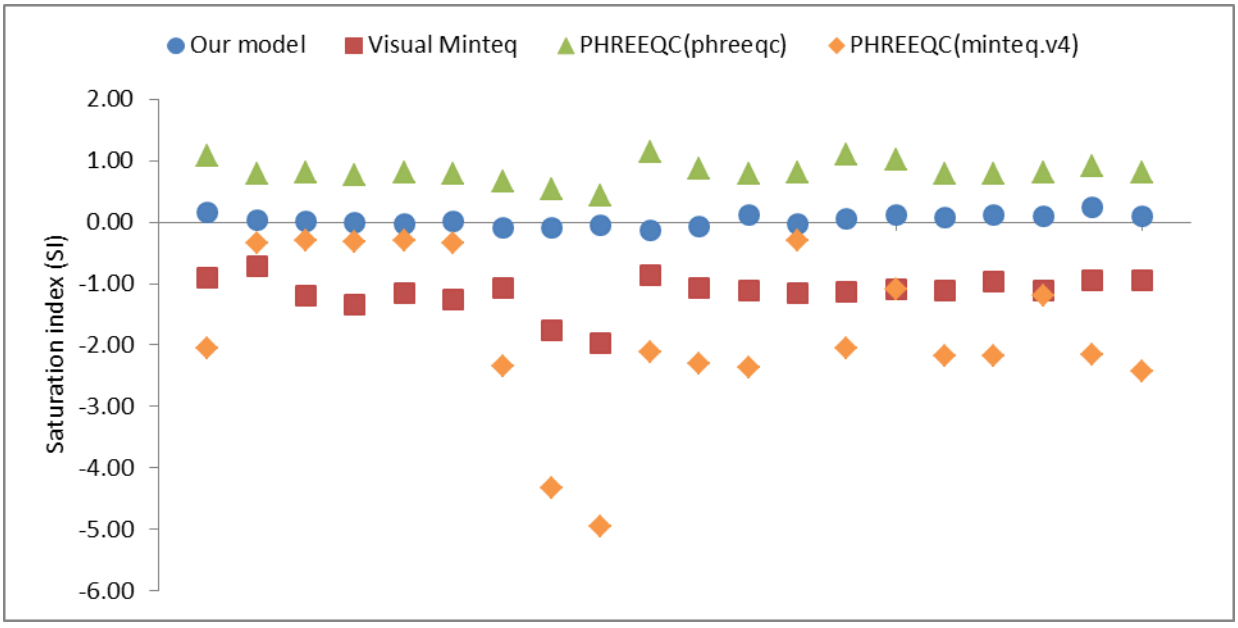

Figure 4.11. The predicted SI values of the mackinawite solubility data by different models.

Table 4.2. Key parameters for mackinawite SI calculation in different software

Software	Our model	Visual Minteq	PHREEQC(default)	PHREEQC(minteq V4)

pK_{sp} (25 °C)	3.55, a function of temperature	3.60, no temperature dependence		4.65, no temperature dependence		3.60, no temperature dependence	
Major Fe-complexes and their stability constants (log ß)	Considered as Fe^{2+}-anion interactions. Considered anions include Cl^-, $Acetate^-$, HS^-, SO_4^{2-}	$FeHS^+$	5.62	$Fe(HS)_2$	8.95	$Fe(HS)_2$	8.95
		$FeCl^+$	-0.2	$Fe(HS)_3^-$	10.987	$Fe(HS)_3^-$	10.987
		$Fe(Acetate)^+$	1.4	$FeCl^+$	0.14	$Fe(Acetate)^+$	1.4
		$FeSO_4$ (aq)	2.39	$FeSO_4$ (aq)	2.25	$FeSO_4$ (aq)	2.39
Activity coefficient model	Pitzer theory	SIT		Debye- Hückel expression is used for major ions, and it is applicable for solution with IS ≤ 2 mol/kg. Davies equation is used for most ion complexes, and it is applicable for solution with IS ≤ 0.5 mol/kg.		Modified Debye-Hückel expression is used for species that have the necessary parameters in the database; otherwise Davies equation is used.	
Activity coefficients of Fe^{2+} and HS^- in experiment 1	0.13; 0.51	0.24; 0.59		0.17; 0.52		$8.41*10^{-4}$; 0.17	

4.2.2. Amorphous FeS solubility

As mentioned previously, the experimental data of experiments 16, 17, 20, and 21 are excluded in mackinawite prediction model development, considering that the Fe(II) and S(-II) concentrations in their effluents are too high and not consistent with those in most experiments. As shown in Table 4.1, experiments 15, 16, and 17 share similar experimental conditions (i.e. same T, IS, initial pH, and initial S(-II) concentration) except initial Fe(II) concentration ($[Fe(II)]_0$), which reflect on Fe(II) / S(-II) ratio. It was expected that these three experiments would have similar Fe(II) concentration at equilibrium ($[Fe(II)]_{eq.}$) after FeS precipitation was complete. However, as shown in Table 4.2, $[Fe(II)]_{eq.}$ increases as Fe(II) / S(-II) ratio increases, and the corresponding SI values at equilibrium are significantly larger than zero. Same situation happened for experiments 19, 20, and 21.

To verify that FeS precipitation was complete and the effluent was at equilibrium with precipitated FeS in high Fe(II) / S(-II) ratio experiments, an experiment with same experimental

condition as experiment 16 but longer Fe(II) and S(-II) reaction time was conducted, and the experiment is called 16'. The reaction time was prolonged by lowering Q from the original lowest value of 0.1 ml/min to 0.02 ml/min and using a big HC-276 reactor (76.20 cm (30 in) length, 0.16 cm (0.0625 in) OD). The regular HC-276 reactor as in experiment 16 is only 17.78 cm (7 in) long with 0.076 cm (0.03 in) OD. The longest reaction time was prolonged from 2.8 min in experiment 16 to 100 min in experiment 16'. As shown in Figure 4.12, in experiment 16, $[Fe(II)]_{eq.}$ = 1.53 mol/L; in experiment 16', $[Fe(II)]_{eq.}$ = 1.56 mol/L. This indicates that FeS precipitation was complete in experiment 16 and its effluent was in equilibrium with the precipitated FeS. However, the precipitated FeS is probably not mackinawite, but a more soluble phase, amorphous FeS.

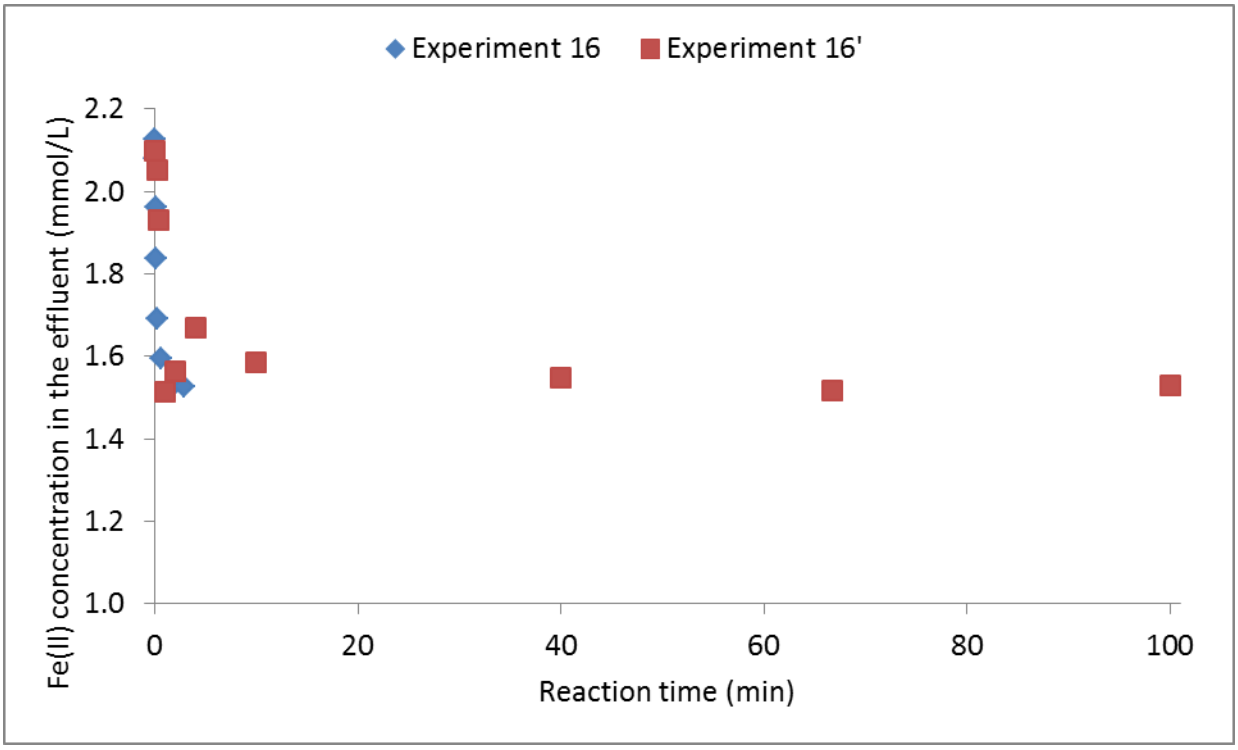

Figure 4.12. Effluent Fe(II) concentration in experiment 16 and 16'.

Amorphous FeS has been observed to precipitate from iron sulfide supersaturated aqueous solution in previous research (Csákberényi-Malasics 2012). The solubility product of amorphous FeS ($K_{sp,\ amorphous\ FeS}$) at 25 °C has been determined to be between $10^{-2.95}$ to $10^{-3.15}$, without a consensus on a recommended value (Bågander 1994; Davison 1991; Schoonen 1991). Based on the range of $K_{sp,\ amorphous\ FeS}$ and $K_{sp,\ mackinawite} = 10^{-3.54}$, when a solution is at equilibrium with amorphous FeS, its SI value with respect to mackinawite should be in the range of 0.39 – 0.59. The calculated SI values of experiments 16, 17, 20, and 21, are in the range of 0.33 – 0.54, which implies that the precipitated FeS is probably amorphous FeS.

Amorphous FeS is usually difficult to be determined by XRD, because it shows no pattern or only one broad peak at 5.4 Å (16.5°) (Rickard 2007). Amorphous FeS is not stable and will transform to mackinawite. The transformation time depends on environmental conditions (Csákberényi-Malasics 2012; Rickard 2007). Once mackinawite is formed, in XRD detection, the strongest peak of mackinawite at 5.03 Å (17.6°) can easily overlap the only possible peak of amorphous FeS at 5.4 Å (16.5°). Amorphous FeS was not identified by XRD in this study.

Furthermore, the effluent of experiment 16 was collected in several 8 ml glass bottles under anoxic condition, leaving minimal air space in the glass bottles. The suspended FeS particles gradually settled down in the glass bottles. After a certain settling time, one bottle was opened, measured the Fe(II) concentration, and then discarded. Nine (9) bottles were used and the settling time ranged from 1 h to 59 h. As shown in Figure 4.13, within 1 h of settling, the Fe(II) concentration remained about 1.53 mol/L, same Fe(II) concentration of the effluent in experiment 16. Later Fe(II) concentration gradually decreased with settling time. After about 23 h, Fe(II) concentration becomes constant, around 0.68 mol/L. As calculated by our prediction

model, 0.68 mol/L Fe(II) corresponds to mackinawite SI = 0. This implies that amorphous FeS probably transformed to mackinawite in the glass bottles, and after 23 h, the aqueous solution was at equilibrium with mackinawite. XRD detection confirmed that the precipitated FeS in glass bottles after 23 h of setting was mackinawite.

Based on the experimental data of this study and data from literature (Davison 1991; Rickard 2006), it appears that highly supersaturated FeS solution tends to form amorphous FeS, and relatively lowly supersaturated FeS solution tends to form mackinawite. Nevertheless, the precipitation kinetics of amorphous FeS and mackinawite did not show significant difference based on observations in this study.

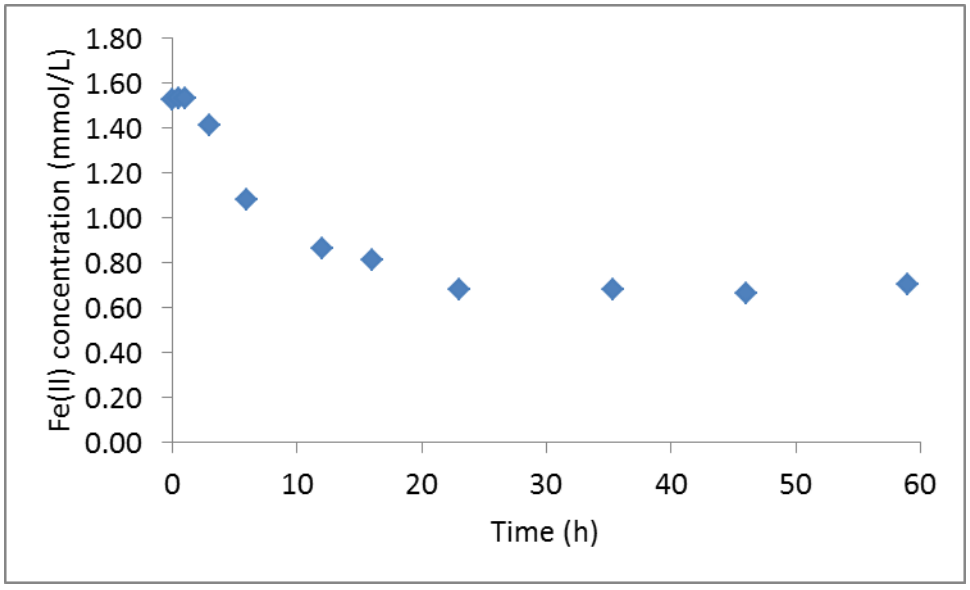

Figure 4.13. Fe(II) concentration in the collected glass bottles

4.3. FeS phase transformation

As mentioned previously, mackinawite is usually observed to be the first formed detectable FeS phase at temperature below 100 °C, no matter whether the FeS is formed through steel corrosion

or aqueous precipitation. There are two possible reasons for this phenomenon. One reason is that mackinawite formation kinetics is faster than other stable phases (Rickard 2007). The other reason is that mackinawite is the most soluble stable FeS phase. A phase with highest solubility often tends to form before the phases with lower solubility (Mullin 2001). Note that amorphous FeS is more soluble than mackinawite and can form before mackinawite, but it is an unstable phase and is difficult to be identified by XRD.

To investigate FeS phase transformation and how operation and solution conditions affect phase transformation, the FeS retained on coupons in the glass column reactor was characterized by SEM and Grazing Incidence XRD. In Grazing Incidence XRD detection, only the surface ~10 μm thick FeS layer was determined, and all parameters were always kept the same. Furthermore, the weight ratio of different FeS phases was also estimated by PDXL software based on XRD results.

4.3.1. Effect of temperature

Experiments 2 – 5 from 23 to 70 °C are used to quantify the temperature effect on phase transformation at low ionic strength. At 70 °C, four separate experiments were run with different experimental times (called aging times), 1.67, 8, 32, and 45 h, and each has the same initial conditions. At 1.67 h, the FeS solid, 100% mackinawite by XRD (Figure 4.14a), looks similar to the freshly precipitated FeS (Figure 4). As aging time increases to 8 h, troilite starts to form at the top of the mackinawite layer (Figure 4.14b), and some troilite crystals are still poorly developed. When aging time increases to 32 and 45 h, more troilite forms on the surface (Figure 4.14c and d). At 45 h, the surface is almost covered by troilite. Figure 4.15 shows a portion of Figure 4.14d that has been broken loose from the coupon surface to reveal the underlying mackinawite with a troilite layer on the top (the solution side). Mackinawite is a black mineral

and troilite is brown, and they may even be differentiated by observation. The coupon mainly covered by mackinawite (e.g. 8 h aging time coupon) has black color (Figure 4.16, left), while the coupon mainly covered by troilite on the surface (e.g. 45 h aging time coupon) has brown color (Figure 4.16, right). Based on the above observations, it is likely that troilite is gradually transformed from mackinawite, instead of directly forming from aqueous solution or corrosion. This qualitative interpretation is consistent with previous researches (Smith 2006).

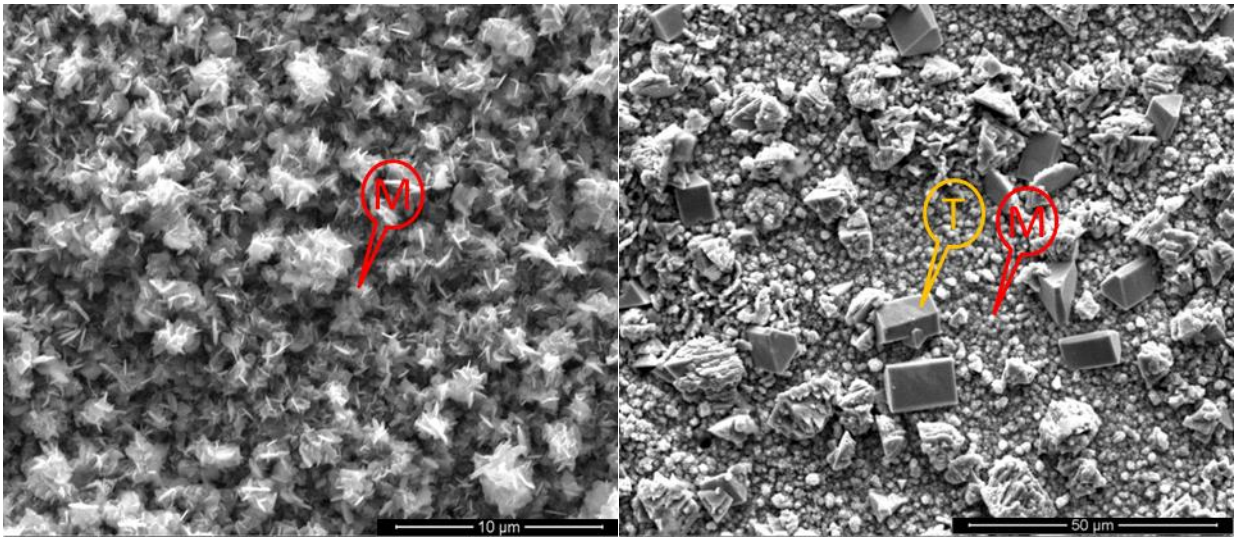

(a) (b)

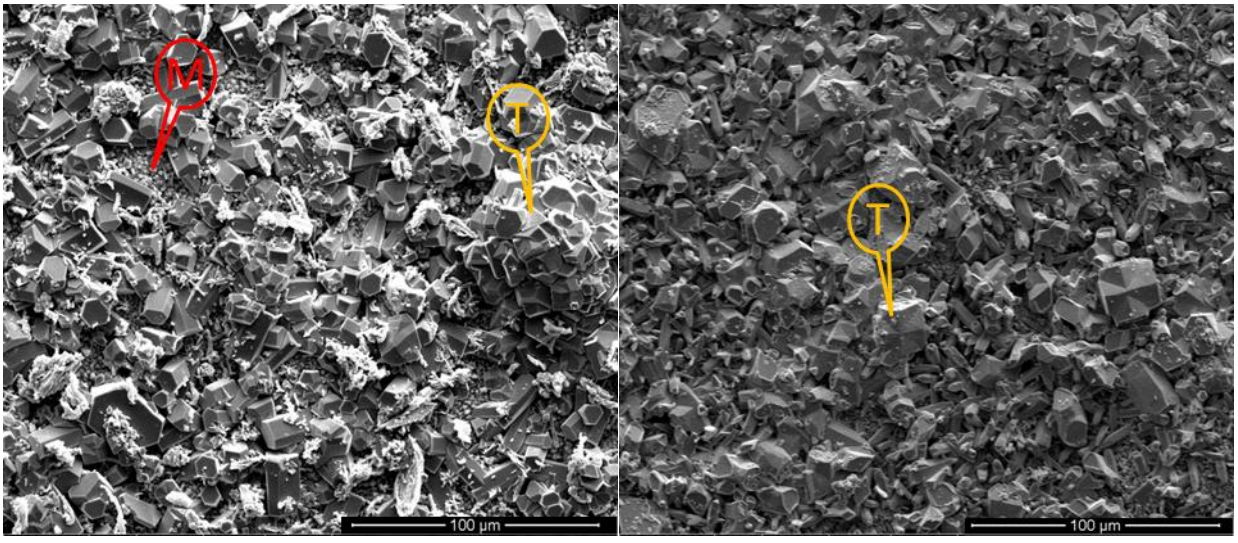

(c) (d)

Figure 4.14. The SEM images of the retained FeS on C1018 coupons formed at 70 °C, IS = 0.00886 mol/kg, and pH = 4.83, with aging times of 1.67 h (a), 8 h (b), 32 h (c), and 45 h (d), respectively. M: mackinawite; T: troilite. Same below.

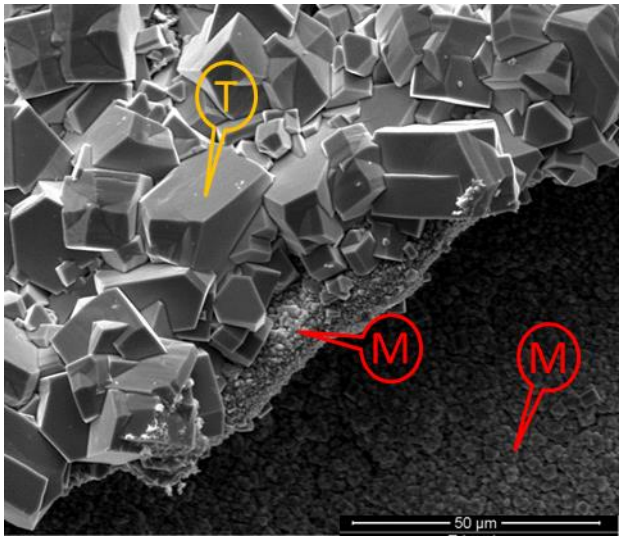

Figure 4.15. The SEM image of the retained FeS on C1018 coupons formed at 70 °C, IS = 0.00886 mol/kg, and pH = 4.83, with aging time of 45 h. The top layer is troilite and the bottom layer is mackinawite.

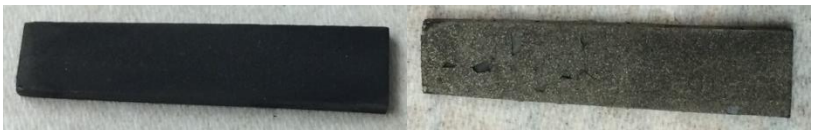

Figure 4.16. Coupons covered with retained FeS formed at 70 °C, IS = 0.00886 mol/kg, and pH = 4.83, with aging times of 8 h (left) and 45 h (right).

Moreover, XRD was used to determine the weight ratio of troilite to mackinawite, Figure 4.17. Troilite fraction (TF) refers to troilite weight to total FeS weight. At 70 °C, the TF of experiments with aging time of 1.67, 8, 32, and 45 h are 0, 0.44, 0.69, and 0.90, respectively. TF versus time can be fitted with an empirical first order equation (equation 4.7) with a correlation

coefficient of 0.9767 (Figure 4.17). In equation 4.7, t(h) is aging time and k_{TF} is the transformation rate constant (h^{-1}). At this experimental condition, $k_{TF} = 4.75 \times 10^{-2}$ h^{-1}, and the corresponding characteristic time, $\tau = 1 / k_{TF} = 21.1$ h.

$$TF_{fitted} = 1 - e^{-k_{TF} \cdot t} \tag{4.7}$$

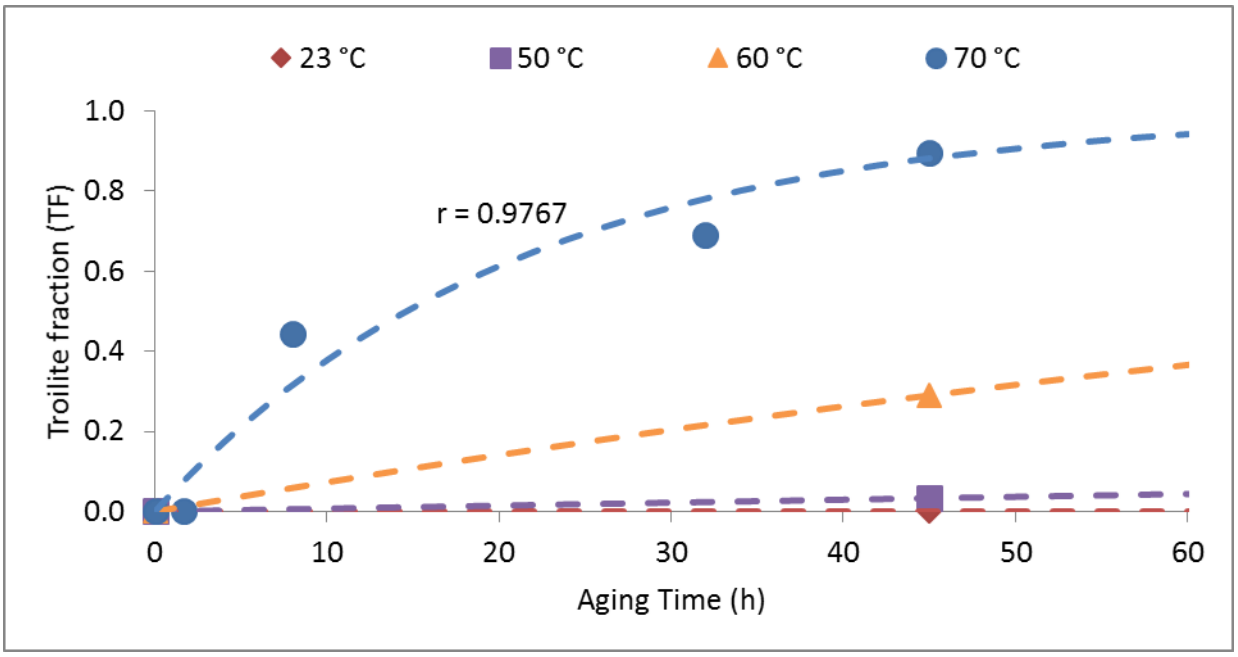

Figure 4.17. Troilite fractions (TF) at different aging times and temperatures, and their corresponding fitting curves. (T = 23 – 70 °C, IS = 0.00886 – 0.02 mol/kg, pH = 4.80 – 4.83, and aging time varies from 1.67 to 45 h)

At 60 °C, IS = 0.0118 mol/kg, and aging time of 45 h, troilite crystals were formed (Figure 4.18, left), and TF = 0.29 (Figure 4.17). At 50 °C, IS = 0.0141 mol/kg, and aging time of 45 h, only scattered troilite crystals were observed in a narrow region of the coupons (Figure 4.18, right), and the remainder of the coupon was covered by mackinawite, with TF = 0.033 (Figure 4.17). Using equation 4.7 to fit the TF at 60 °C and 50 °C, the $k_{TF} = 7.60 \times 10^{-3}$ h^{-1} and 7.46×10^{-4} h^{-1},

respectively. As temperature drops from 70 °C to 50 °C, the τ of mackinawite transformation to troilite increases from 21.1 to 1342 h (55.9 days). With the fitted k_{TF} values at 50 °C, 60 °C, and 70 °C, the activation energy (E_a) of mackinawite transformation can be estimated by Arrhenius equation ($\ln k_{TF} = 64.188 - 23050/T$, with correlation coefficient r = 0.9987), E_a = 192 ± 9.7kJ/mol. T is in unit of K.

At 23 °C with aging time of 45 h and 0.0193 mol/kg IS, only mackinawite is observed in SEM and detected by XRD, and TF ≈ 0. Furthermore, two experiments were conducted at 23 °C and 2.03 mol/kg IS (experiment 1) with aging times of 45 h and 112.5 h. In both experiments, only mackinawite was observed. This observation is consistent with the fact that pyrrhotite group (including troilite) is rarely found in marine sediments (Rickard 2007), which is probably due to the low temperature. With mackinawite transformation E_a = 192 kJ/mol, the τ of mackinawite transformation at 23 °C and 4 °C (estimated marine sediments temperature (Müller 2016)) are estimated to be 96.2 years and 19970 years, respectively.

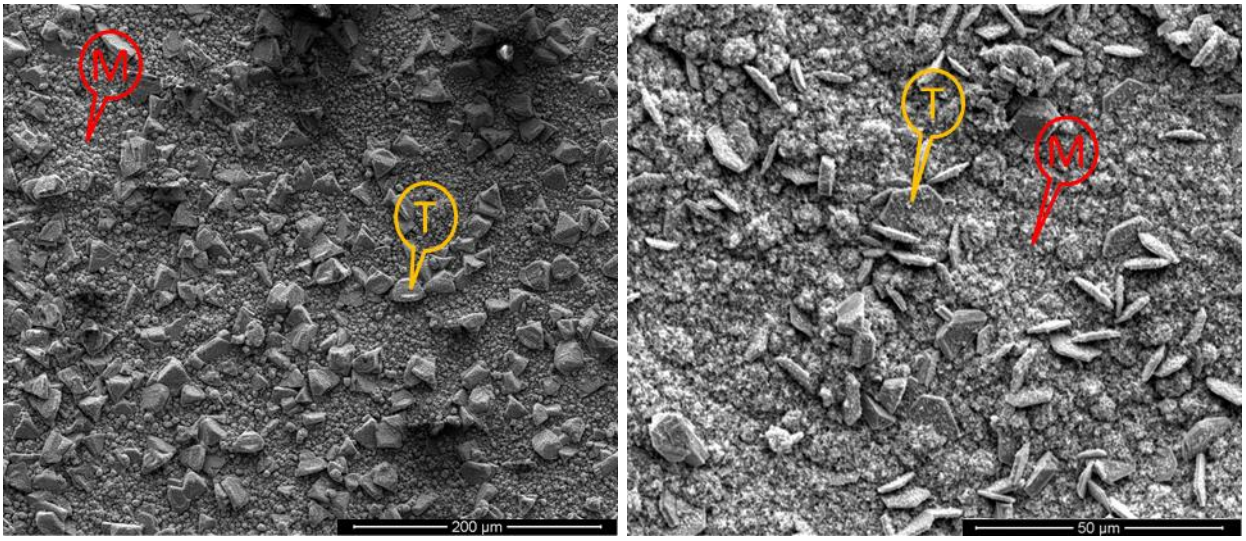

Figure 4.18. The SEM image of the retained FeS on C1018 coupons formed at 60 °C, IS = 0.0118 mol/kg, and pH = 4.82 (left), and at 50 °C, IS = 0.0141 mol/kg, and pH = 4.81 (right), with aging time of 45 h. The right figure displays the only narrow region where troilite formed.

4.3.2. Effect of ionic strength

Experiments 5 – 9 from IS 0.00886 to 5.03 mol/kg are used to investigate the IS effect on phase transformation at 70 °C, with aging time of 45 h. As shown in Figure 4.19a (same as Figure 4.14d), when IS = 0.00886 mol/kg, most mackinawite transforms to troilite, and the corresponding TF = 0.90. When IS increases to 0.118 mol/kg, troilite still forms but with much less (Figure 4.19b), and TF = 0.24. When IS = 2.03 mol/kg, only scattered troilite can be observed (Figure 4.19c) and TF = 0.062. When IS further increases to 4.03 and 5.03 mol/kg, no transformation was observed within 45 h and TF is negligible (Figure 4.19d). However, troilite has been observed in the oilfield (Wang 2013), and the IS of oil and gas produced water is typically 1 to 3 mol/kg. Based on the observations in the oilfield and in this study, high IS appears to only slow down, instead of stop, mackinawite transformation to troilite.

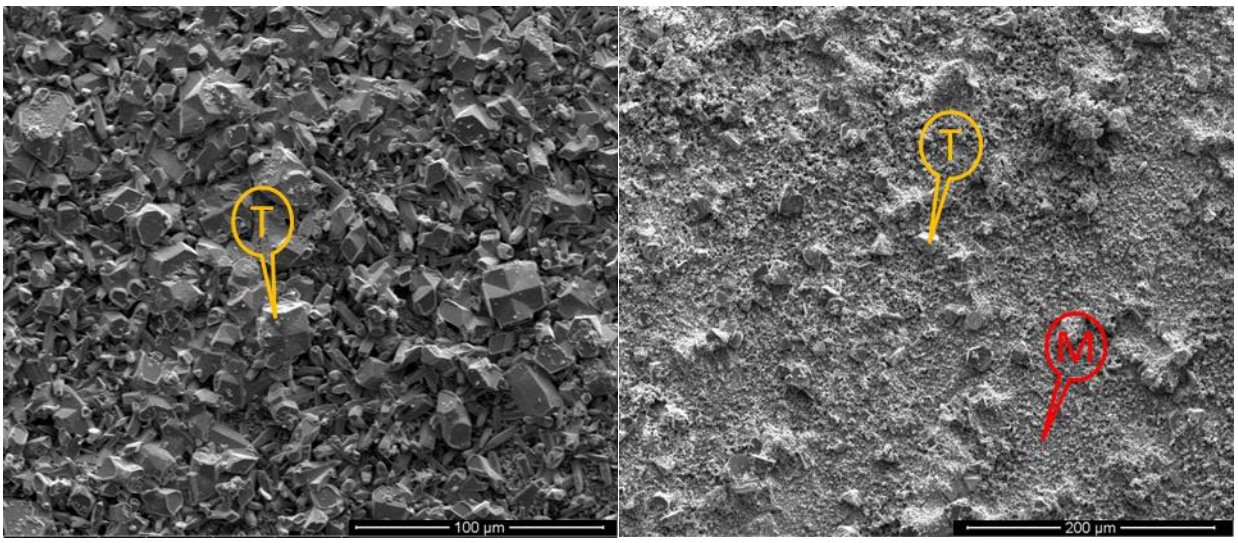

(a) (b)

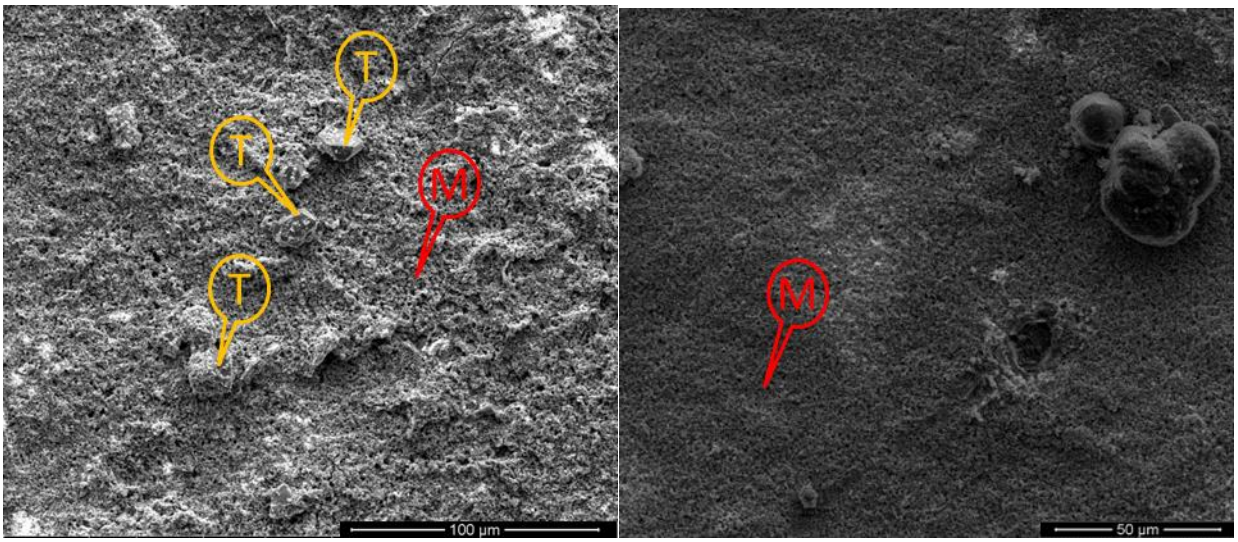

(c) (d)

Figure 4.19. The SEM images of the FeS retained on C1018 coupons at 70 °C in solution with (a) IS = 0.00886 mol/kg, pH = 4.83, (b) IS = 0.118 mol/kg, pH = 4.72, (c) IS = 2.03 mol/kg, pH = 4.44, and (d) IS = 4.03 mol/kg, pH = 4.36. (Note that the SEM image of FeS at IS = 5.03, pH = 4.36 mol/kg is similar to that at IS = 4.03 mol/kg.)

The mechanism of mackinawite transformation to troilite is still unknown, but FeS phase transformation often involves one of the following two mechanisms. One mechanism is that the precursor phase dissolves and re-precipitates as a new phase, which is believed to be the mechanism of mackinawite transformation to pyrite (Rickard 2007). The other mechanism is solid phase transformation, which is a very likely mechanism of mackinawite transformation to greigite (Rickard 2007). In these two mechanisms, small sized mackinawite particles are easier to dissolve or to undergo solid transformation than larger particles, which may explain why low IS favors mackinawite transformation.

In low IS solutions, due to the electric charge on mackinawite particle surface, the double layer of each particle is thick and particles repeal each other. In such case, mackinawite particle size is

generally small. When IS increases by adding NaCl salt, the Na^+ and Cl^- ions neutralize the surface electric charge and reduce the double layer thickness, so that small particles aggregate to form larger particle aggregates. Compared with large mackinawite aggregates formed at high IS, small particles formed at low IS are easier to dissolve and re-precipitate as another phase or to undergo solid phase transformation.

The Debye length, $\kappa^{-1} = \left(2F^2 IS \times 10^3 / \varepsilon\varepsilon_0 RT\right)^{-1/2}$, is the characteristic thickness of particle double layer, and it is proportional to $IS^{-1/2}$. After the constants are evaluated for water at 70 °C, the Debye length can be expressed as $\kappa^{-1}(nm) = 0.295 / \sqrt{IS\left(mol/kg\right)}$ (Stumm 1995). At the lowest IS = 0.008856 mol/kg, the Debye length is 3.13 nm. Since the diameter of a water molecule is about 0.275 nm, about 11 water molecules can thick around a 3.13 nm size particle before its electrostatic potential drops to 1/e of the surface value. At IS = 2.03 mol/kg, the Debye length is about 0.207 nm, less than one water molecule diameter, which implies that there is little electrostatic potential far from the particle surface and particles are easy to aggregate and grow in size. Furthermore, as shown in Figure 4.20, the measured TF values at different IS are proportional to the corresponding Debye length.

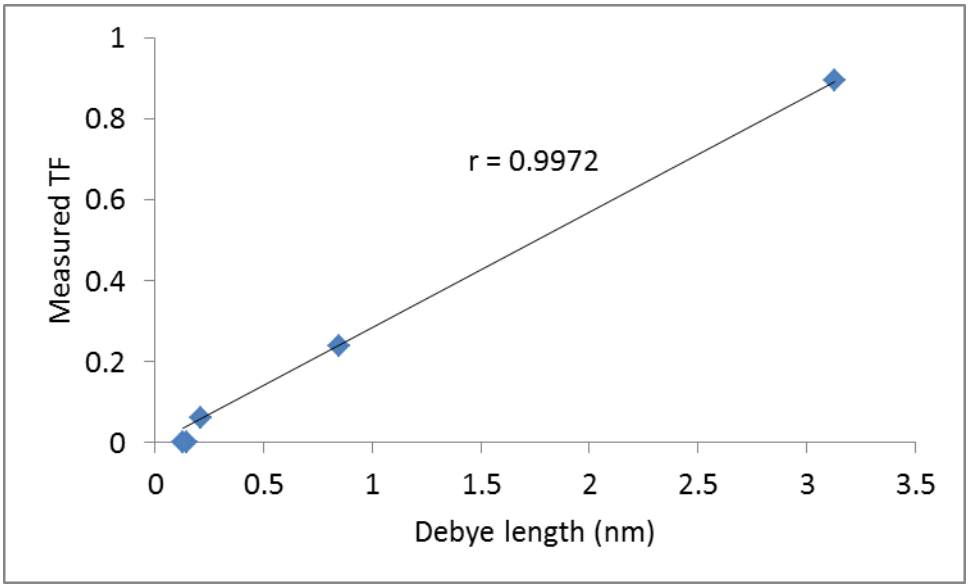

Figure 4.20. The relationship between troilite fraction (TF) and Debye length at 70 °C.

The above observations indicate that mackinawite transformation is a function of T, aging time (t), and IS. The overall formation of troilite from mackinawite can be empirically described by multiplying the transformation rate constant in equation 4.7 with an IS term, and equation 4.8 is the semi-empirical function. With B = 0.00656 and C = 0.0153, assuming that B and C are independent of temperature, the correlation coefficient is 0.9817 for the experimental data in Table 4.3. As shown in Table 4.3, the calculated TF values by equation 4.8 are comparable to the measured TF values.

$$TF_{fitted} = \left(1 - e^{-t \cdot k_{TF}}\right), \text{with } k_{TF} = \frac{C}{B + IS} \cdot e^{64.188 - 23050/T} \tag{4.8}$$

Table 4.3. Comparison of the measured TF and the calculated TF values.

T (°C)	IS (mol/kg)	t (h)	Measured TF	Calculated TF
23	0.0193	45	0	4.52E-05
23	2.05	45	0	1.42E-06
23	2.05	112.5	0	5.68E-07

50	0.0141	45	0.033	0.026
60	0.0118	45	0.29	0.22
70	0.00886	1.67	0	0.11
70	0.00886	8	0.44	0.33
70	0.00886	32	0.69	0.80
70	0.00886	45	0.90	0.90
70	0.118	45	0.24	0.24
70	2.03	45	0.062	0.017
70	4.03	45	0	0.012
70	5.03	45	0	0.010

4.3.3. Effect of FeS source

The above experimental data presented in this section were all conducted on C1018 coupons, and the FeS retained on coupons comes from two sources, coupon corrosion and FeS deposition from aqueous solution. We did two comparisons to test if FeS source affect FeS phase transformation.

First, we compared experiments 7 and 13, and they have similar experimental conditions and same aging time of 45 h. Experiment 7 has aqueous Fe(II) source, same as many previous experiments. The retained FeS comes from both corrosion and aqueous deposition, so that this experiment is named “corrosion + deposition”. Experiment 13 does not have aqueous Fe(II) source, and the retained FeS on the coupons is from corrosion. This experiment is called “only corrosion”. According XRD detection, troilite formed in both experiments. However, the TF in “only corrosion” is 0.30, much higher than the TF of “corrosion + deposition”, TF = 0.062. Also, comparing their SEM images, the troilite in “only corrosion” have both needle-like and hexagonal morphology (Figure 4.21b), while the troilite in “only deposition” and “corrosion and deposition” mainly have hexagonal morphology (Figure 4.21a).

Second, we compared experiments 5 and 14. They share same experimental conditions and same aging time of 45 h. The retained FeS in experiment 5 comes from corrosion and aqueous

deposition, and the experiment is named “corrosion + deposition (2)”. In experiment 14, the first C1018 coupon was replaced by a corrosion resistant HC-276 coupon, such that the retained FeS on the HC-276 coupon comes from only aqueous deposition. This experiment is named “only deposition”. As shown in Figure 4.22, hexagonal troilite are observed in both “corrosion + deposition (2)” and “only deposition”, but the troilite crystals in “only deposition” look much thinner. Probably for this reason, XRD could not identify the troilite in “only deposition”, and only mackinawite was detected. Therefore, we could not compare the TF values of “corrosion + deposition (2)” and “only deposition”. But according to SEM images, it seems that the TF of “only deposition” is less than that of “corrosion + deposition (2)”.

Based on the above two comparisons, it seems that the FeS from corrosion is more likely to transform to troilite than the FeS from aqueous deposition. As far as we know, the effect of FeS source on phase transformation has not been reported previously.

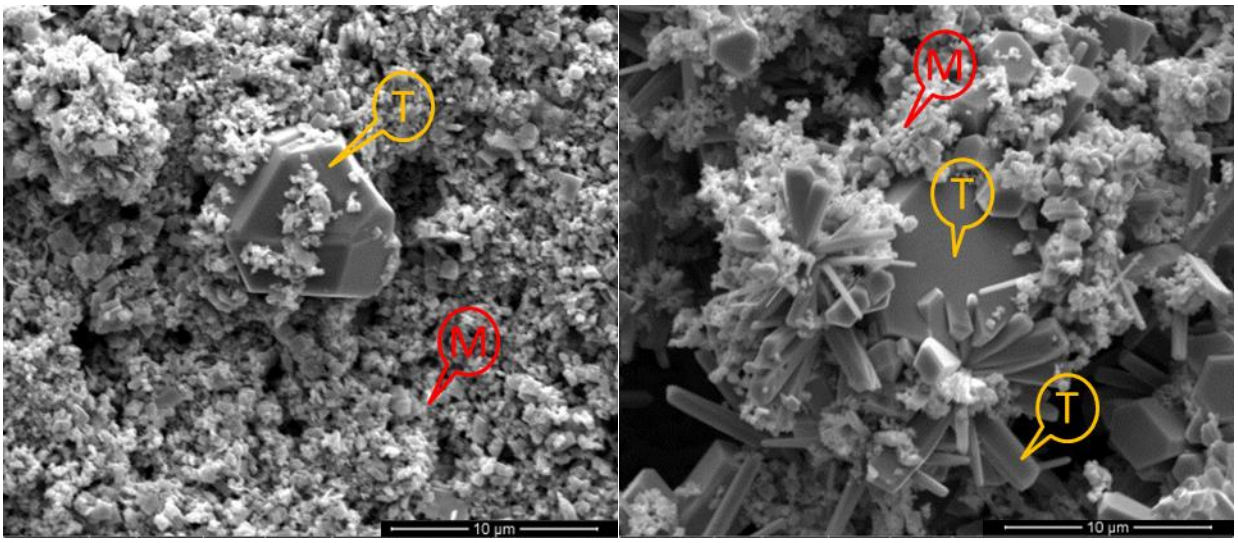

(a) (b)

Figure 4.21. The SEM images of the retained FeS on coupons in (a) “corrosion + deposition” experiment and (b) “only corrosion” experiment.

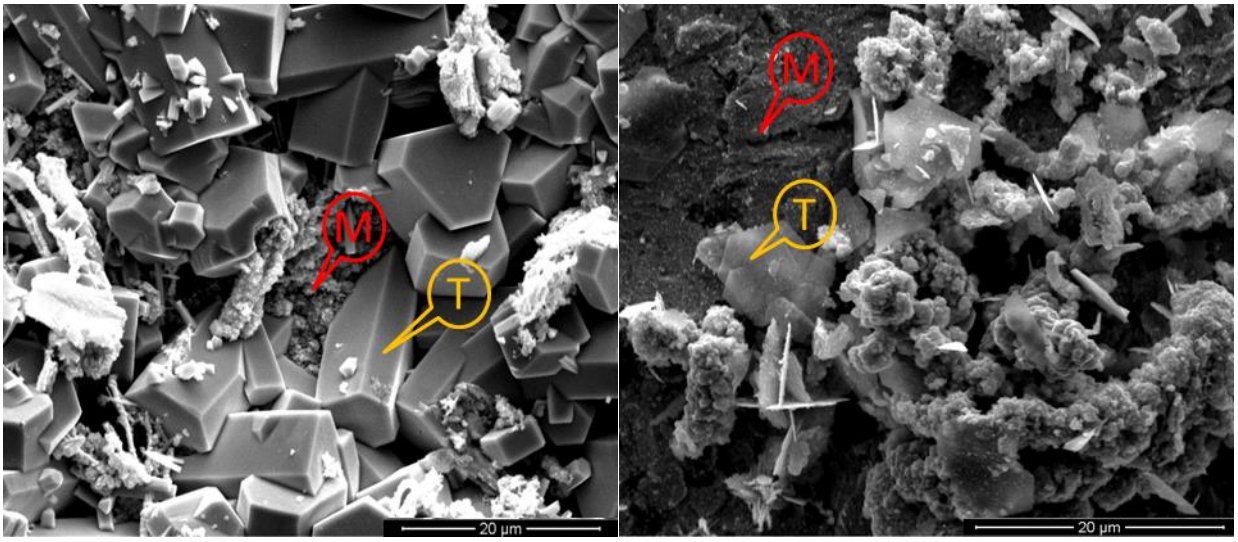

(a) (b)

Figure 4.22. The SEM images of the retained FeS on coupons from (a) “corrosion + deposition” experiment and (b) “only deposition” experiment.

4.3.4. Effect of FeS dispersant

A novel chemical for FeS growth inhibition and dispersion has been discovered by our research group (Bhandari 2016), and it is a polymer with oxazoline functional groups (Figure 4.23). This FeS dispersant was tested at experimental condition of T = 60 °C, IS = 0.0275 mol/L, and pH = 4.59, with experimental time of 30 h, which corresponds to the condition of both experiments 26 and 27. Experiment 26 is the blank experiment without dispersant. In experiment 27, the FeS dispersant was added into the Fe(II) solution during solution preparation, and the influent had 100 mg/L FeS dispersant.

For coupons in experiment 26, the FeS layer is uniform and firmly sticks to the coupon (Figure 4.24, left). Mature troilite crystals form on the surface (Figure 4.24, right), and the TF = 0.52. For coupons in experiment 27, the FeS showed two noticeable different layers under the dispersant treatment (Figure 4.25, left). The bottom layer (in grey color) sticks firmly to the

coupon and its morphology is like mackinawite. The top layer (in black color) is easy to slough off, and its morphology is modified by this dispersant and does not match with any common FeS crystal morphology (Figure 4.25, right). The XRD detection result showed 100% mackinawite (i.e. TF = 0) (Figure 4.26). This indicates that this dispersant can effectively inhibit mackinawite transformation to troilite or another phase.

A common way for FeS scale removal in the oilfield is using strong acid (e.g. hydrochloric acid, HCl) dissolving FeS. Most FeS phases can dissolve in strong acid, but pyrite is hardly dissolvable. It would be of great value if this dispersant can inhibit mackinawite or other phase transformation to pyrite.

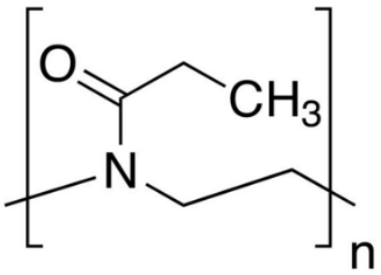

Figure 4.23. The functional group of the FeS dispersant.

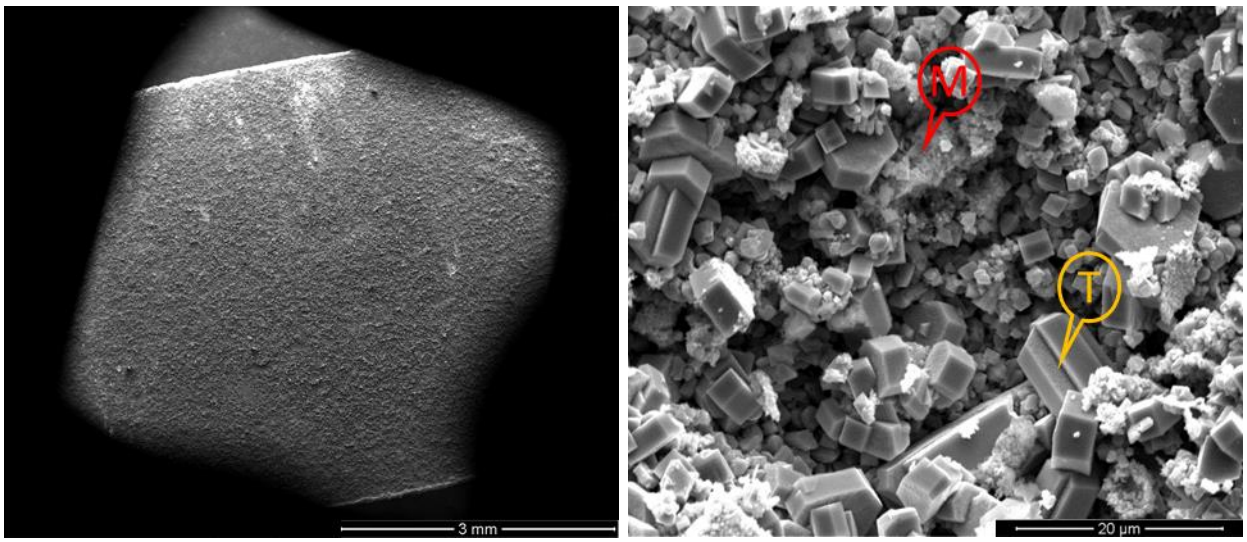

Figure 4.24. The SEM images of coupons in the blank experiment (experiment 26)

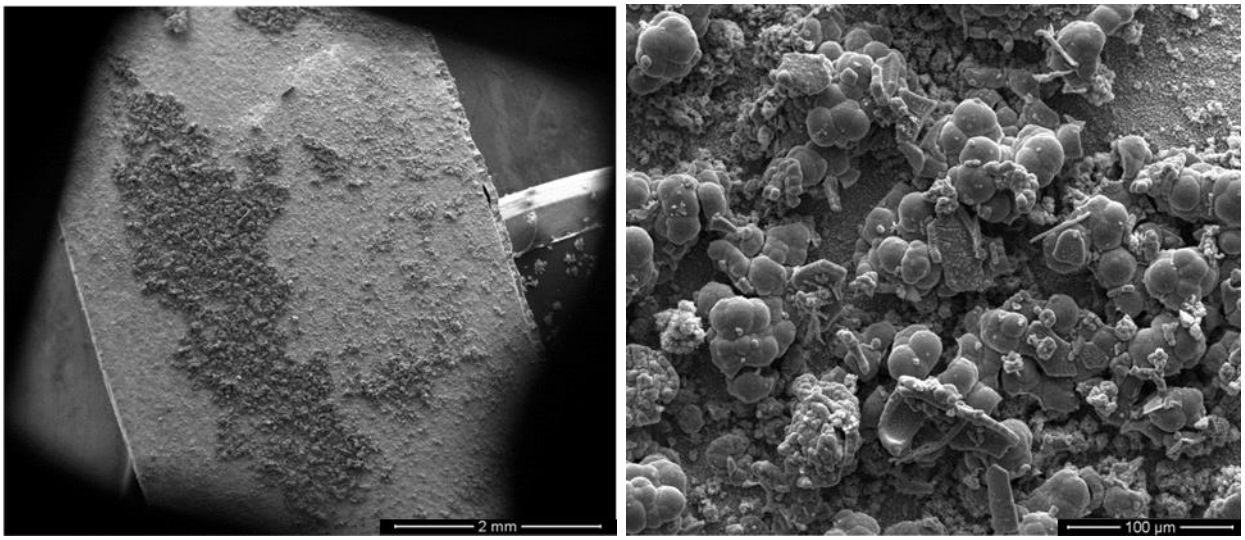

Figure 4.25. The SEM images of coupons in the experiment with 100 mg/L dispersant (experiment 27). The right one is the magnified top FeS layer.

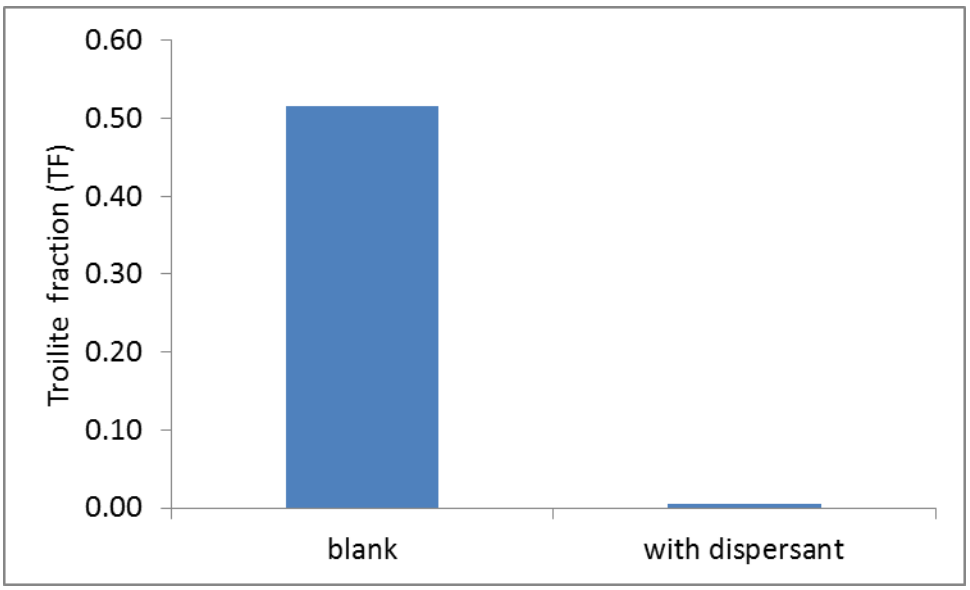

Figure 4.26. Troilite fraction (TF) values in the blank experiment (experiment 26) and the experiment with 100 mg/L FeS dispersant (experiment 27).

4.4. H_2S corrosion and FeS scale retention

Figure 4.27 (from left to right) shows a typical C1018 coupon before experiment, after experiment with retained FeS scale on the surface, and after FeS scale removal by Clarke's solution. After experiment, C1018 coupon was fully covered by a FeS scale layer which came from coupon corrosion by H_2S and FeS deposition from aqueous solution. In most cases, the FeS layer was firmly attached onto the coupon and did not slough off, except when a FeS dispersant was applied (illustrated later). As mentioned previously, H_2S corrosion on coupons was evaluated with corrosion rate (CR) (equation 3.2), and FeS scale retention on coupons was evaluated with scale retention rate (SR) (equation 3.3). In each experiment, two coupons were used and each coupon had its own CR and SR values, but their values were usually close. In below section, the presented CR and SR values are the averages of two coupons.

Figure 4.27. A typical C1018 coupon before experiment (left), after experiment with retained FeS scale on the surface (middle), and after FeS scale removal by Clarke's solution (right).

4.4.1. Effect of temperature

The effect of temperature on H_2S corrosion and FeS scale retention was tested at 23 °C, 50 °C, 60 °C, and 70 °C, IS = 0.00886 – 0.0193 mol/kg, pH = 4.80 – 4.83, and experimental time of 45 h, which refer to experiments 2 – 5. As displayed in Figure 4.28, at 23 °C, CR and SR are only 0.53 and 0.26 mm/year, respectively; at 70 °C, CR and SR increase dramatically to 1.41 and 3.61 mm/year, respectively. Although the CR and SR values at 50 °C and 60 °C are similar, CR and SR generally increase with temperature. At 23 °C, the SR value is smaller than the CR,

indicating that most precipitated FeS and even part of corrosion formed FeS were flushing out with effluent. High temperature can accelerate H_2S corrosion and encourage FeS scale retaining on coupons.

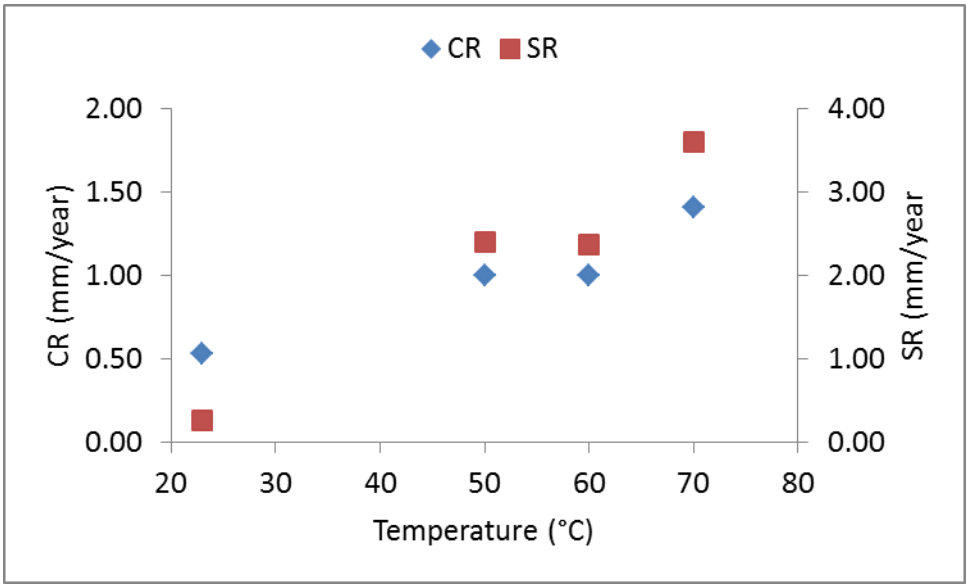

Figure 4.28. H_2S corrosion rate (CR) and FeS scale retention rate (SR) at different temperature.

The changing trend of SR with increasing temperature was also reflected by the FeS layer thickness. As shown in Figure 4.29, the FeS layer thickness increases with temperature. Due to the porosity and not entirely even distribution of the formed FeS layers, the layer thickness difference may not be proportional to the difference of their corresponding SR values, but they both show the same increasing trend.

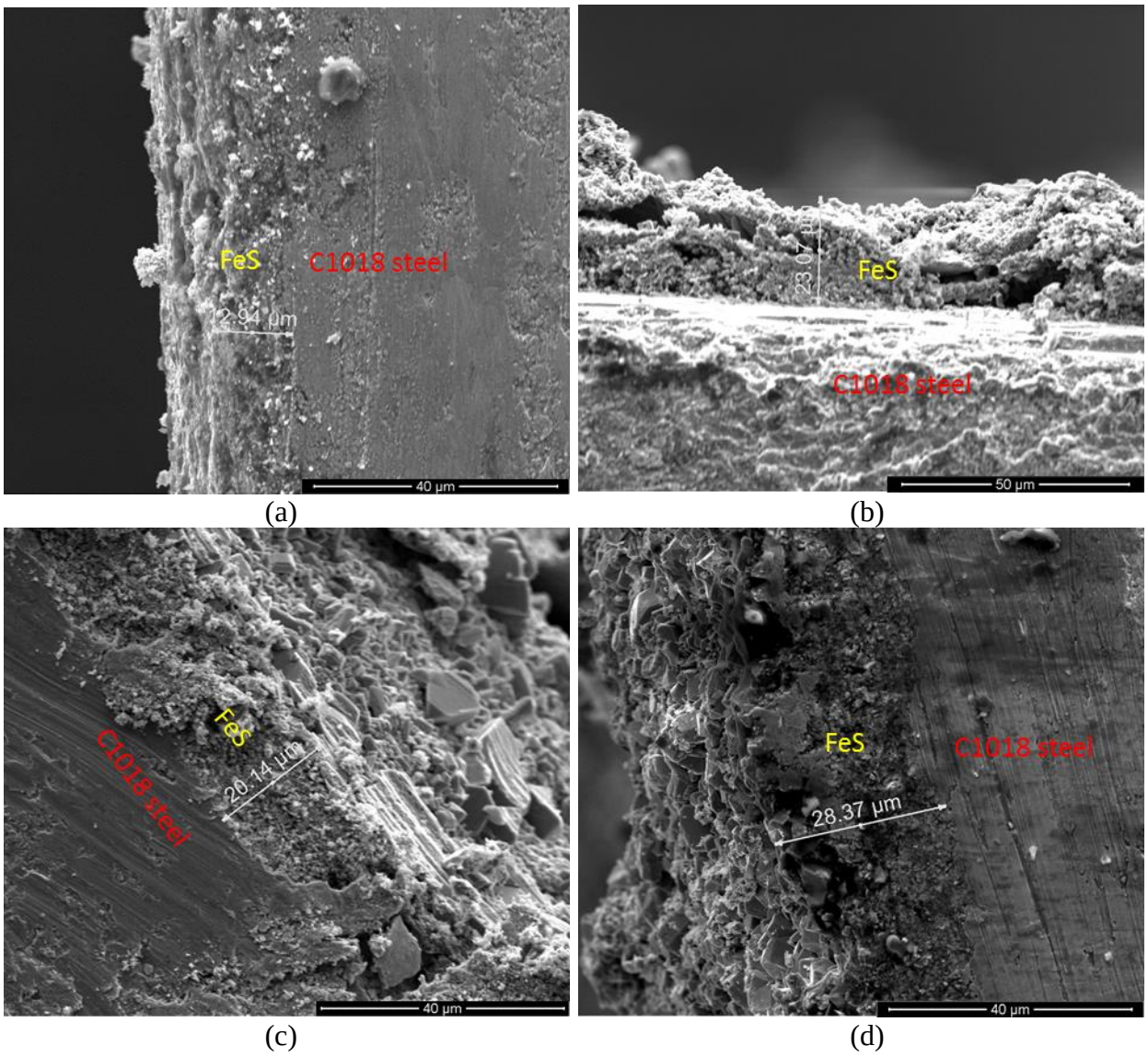

Figure 4.29. The thickness of the FeS layers formed at 23 °C (a), 50 °C (b), 60 °C (c), and 70 °C (d).

4.4.2. Effect of ionic strength

IS impact on H_2S corrosion and FeS scale retention were investigated at 0.00886, 0.193, 2.03, 4.03, 5.03 mol/kg, T = 70 °C and pH = 4.36 – 4.81, with experimental time of 45 hours, which refer to experiments 5 – 9. The minor pH change is mainly due to adjunct potential caused by IS. As displayed in Figure 4.30, CR and SR generally increase as IS increases from 0.00886 to 2.03

mol/kg, but then dramatically decrease as IS further increases to 4.03 and 5.03 mol/kg. The highest CR and SR values, 1.86 and 4.65 mm/year, were at IS = 2.03 mol/kg, and the lowest CR and SR values, 0.50 and 0.76 mm/year, were at IS = 5.03 mol/kg. The FeS layer thickness also shows the same change trend with SR values as IS increases (Figure 4.31).

From this result, it seems that moderately high IS (e.g. 2 mol/kg) can accelerate H_2S corrosion and FeS scale retention, but extra high IS (e.g. 4 or 5 mol/kg) can slow down H_2S corrosion and inhibit FeS scale retention. Previous researches showed that chloride plays an important role in H_2S corrosion mechanism and affects H_2S corrosion rate (Dougherty 2004; Smith 2006), but there are controversies on whether chloride promotes or inhibits H_2S corrosion (Criaud 1989; Dougherty 2004). In this study, chloride impact on H_2S corrosion rate depends on chloride concentration. Some other conditions, such as temperature and pH, may also affect chloride impact on H_2S corrosion (Dougherty 2004).

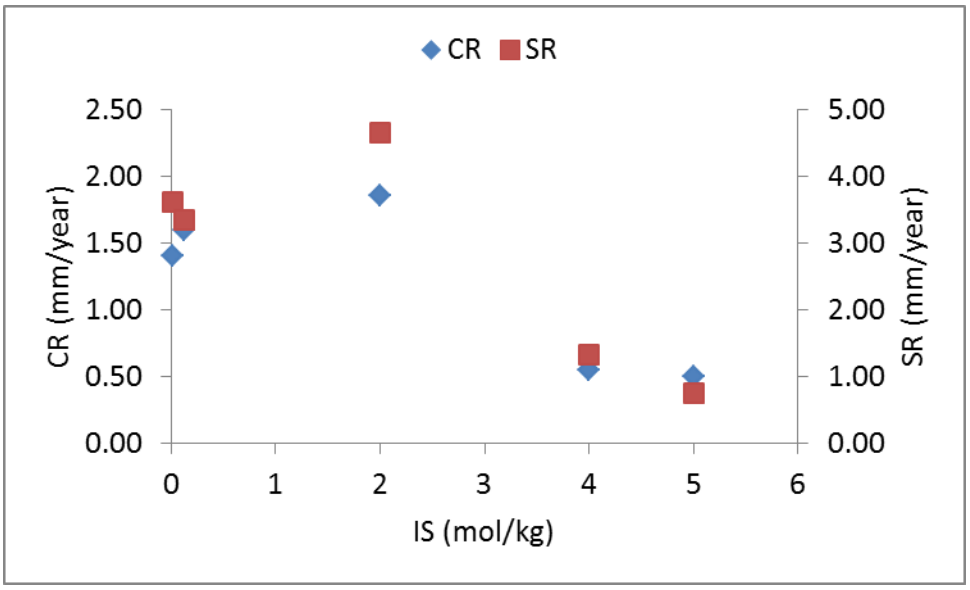

Figure 4.30. H_2S corrosion rate (CR) and FeS scale retention rate (SR) at different IS.

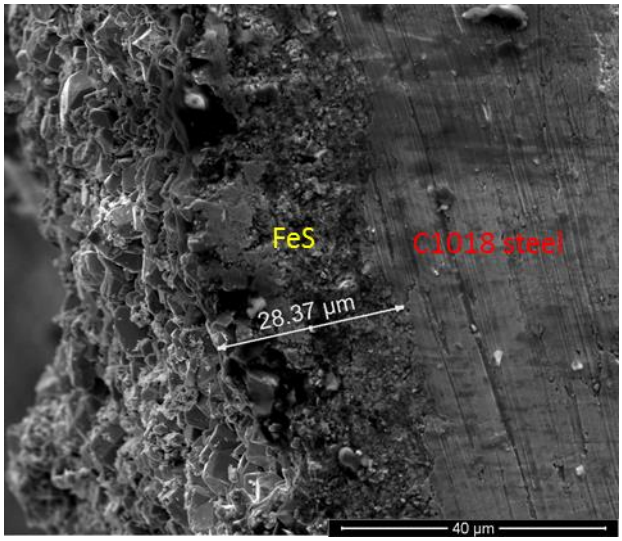
FeS
C1018 steel
28.37 µm
40 µm

(a)

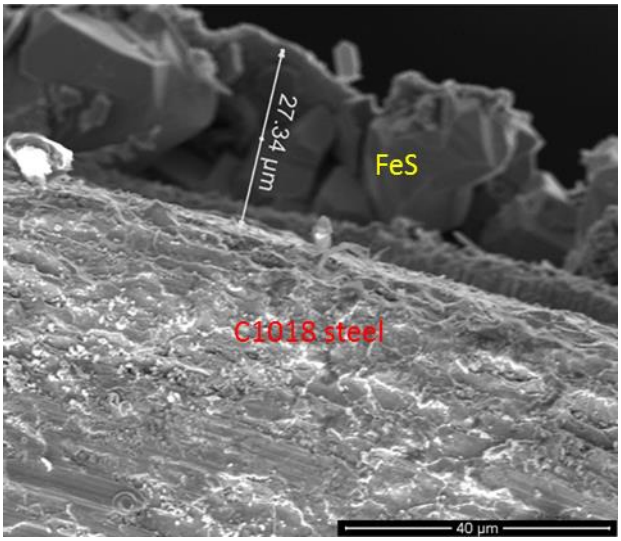
27.34 µm
FeS
C1018 steel
40 µm

(b)

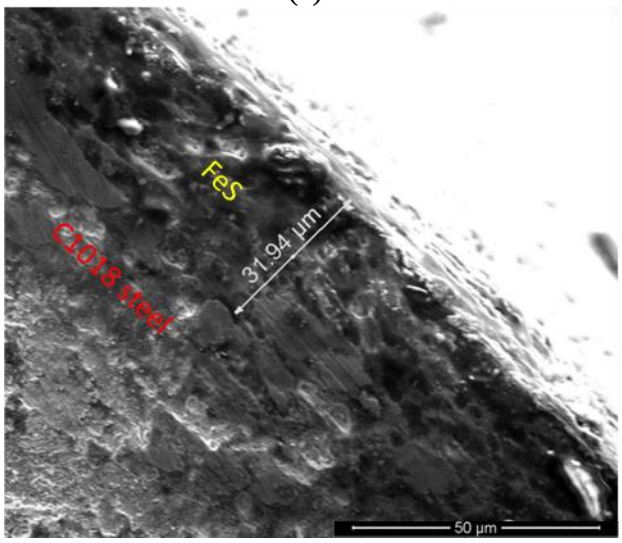
FeS
C1018 steel
31.94 µm
50 µm

(c)

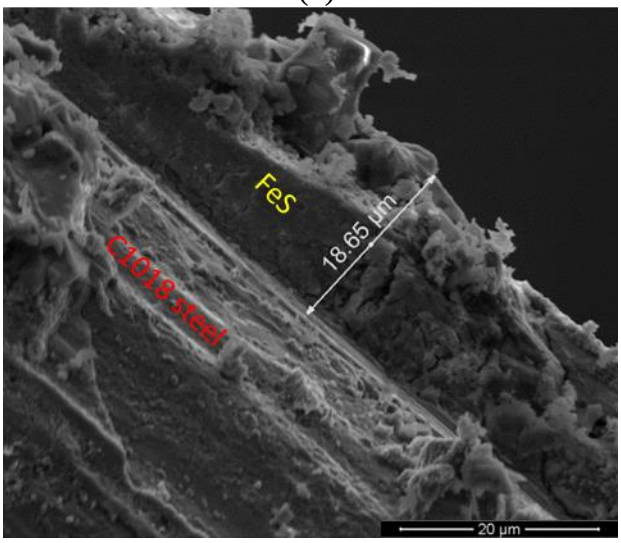
FeS
C1018 steel
18.65 µm
20 µm

(d)

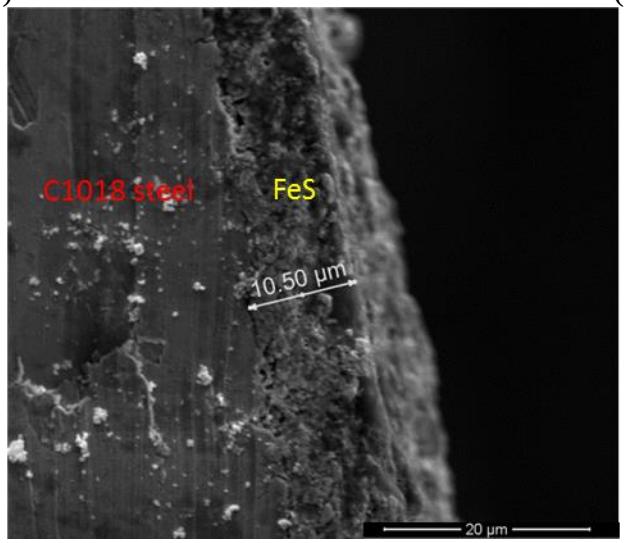
C1018 steel
FeS
10.50 µm
20 µm

(e)

Figure 4.31. The thickness of the FeS layers formed at IS = 0.00886 mol/kg (a), 0.118 mol/kg (b), 2.03 mol/kg (c), 4.03 mol/kg (d), and 5.03 mol/kg (e).

4.4.3. Effect of FeS dispersant

The effect of the FeS dispersant (Figure 4.23) on H2S corrosion and FeS scale retention were quantified by comparing CR and SR values of experiments 26 and 27. As shown in Figure 4.32, compared with the blank, dispersant treatment does not change CR, but dramatically decreased SR value from 4.74 mm/year to 2.67 mm/year. The SR value decrease is consistent with the observation that the top FeS layer was slough off, as mentioned in section 4.3.4. This results indicate that this dispersant does not affect H_2S corrosion on coupons, but effectively inhibit FeS scale retention on coupons

Moreover, this FeS dispersant significantly reduced FeS particle size. In the blank experiment, the suspended FeS particles in the effluent could be removed by 0.22 μm filters. However, under this dispersant treatment, 0.22 μm filters could not remove any suspended FeS particles in the effluent. Hence, this FeS dispersant not only can reduce FeS particle size to lower than 0.22 μm, but also prevent FeS particles from attaching to the preexisted FeS layer. The FeS dispersant will be of great potential for field application on inhibiting FeS accumulation on tubing and reservoir formation.

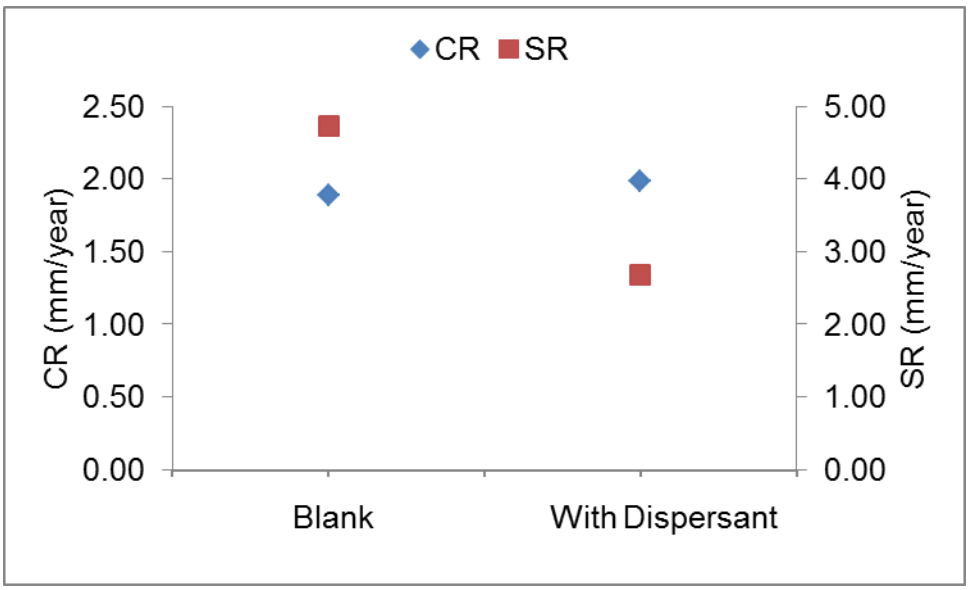

Figure 4.32. H_2S corrosion rate (CR) and FeS scale retention rate (SR) of coupons with and without dispersant treatment.

Chapter 5. Summary and Future Research

5.1 Summary

This study has developed a reliable anoxic apparatus by using argon gas to remove oxygen and acetic acid and sodium acetate to control solution pH. With this apparatus, we investigated FeS precipitation kinetics, mackinawite solubility, and FeS phase transformation simultaneously. The effects of temperature, IS, and [Fe(II)] / [S(-II)] ratio, and FeS source were investigated.

The kinetics of FeS precipitation was found to be a pseudo first order reaction with respect to Fe(II) concentration, when Fe(II) concentration is significantly lower than S(-II) concentration. FeS precipitation is probably diffusion controlled reaction based on its low activation energy, 15.12 kJ/mol. FeS precipitation kinetics can be accelerated by high temperature and high ionic strength, and is not significantly affected by reactor (apparatus) type or [Fe(II)] / [S(-II)] ratio, at least at ratios tested.

Mackinawite solubility was measured at temperature 23 – 125 °C, ionic strength 0.00886 – 5.03 mol/kg, and pH 4.27 – 5.05. A model based upon Pitzer theory specific ion interactions for predicting mackinawite solubility and precipitation has been developed by using FeS solubility data measured in this study and data from literature. A comparison on FeS solubility prediction was made among our model, Visual Minteq, and PHREEQC. Moreover, amorphous FeS was synthesized, but it transformed to mackinawite. It seems that highly supersaturated iron sulfide solution tends to form amorphous FeS, while relatively lowly supersaturated iron sulfide solution tends to form mackinawite.

Freshly precipitated FeS was found to be mackinawite at $T \leq 100$ °C. Mackinawite can transform to troilite at temperature ≥ 50 °C. High temperature and low ionic strength promote the phase

transformation. Once troilite formed, there was no evidence of further transformation to any other stable FeS phase. A semi-empirical model has been developed to predict the fraction of troilite formed versus temperature, ionic strength, and time. Mackinawite formed directly on the steel from corrosion is easier to transform to troilite than the mackinawite formed during aqueous precipitation. The FeS dispersant discovered by our research group is able to modify the FeS morphology and prevent mackinawite transformation to troilite.

Both H_2S corrosion and FeS scale retention on C1018 carbon steel can be significantly accelerated by high temperature and impeded by extra high ionic strength ($IS \geq 4$ mol/kg). The FeS dispersant can effectively reduce FeS particle size and inhibit FeS scale retaining on steel, so as to prevent FeS accumulation on steel. This implies that this dispersant has great potential on FeS control in the oilfield.

This study presented a new approach for iron sulfide study and contributed valuable data of FeS precipitation kinetics, mackinawite solubility, FeS phase transformation, H2S corrosion, and FeS scale retention at different operational and solution conditions. These data are essential for FeS prediction and control in industry.

5.2 Future research

There still remains a lot need to be investigated on FeS research, and a few directions are illustrated below.

First, investigate pH effect on FeS precipitation kinetics, solubility, phase transformation, scale retention, and H_2S corrosion. Fe(II) and S(-II) complexes, FeS^0 and $Fe(HS)_2$, may play important roles on FeS solubility at pH > 6 (Davison 1999; Rickard 2006). Our model for FeS solubility prediction at pH > 6 needs to be improved. Also, at pH < 7, H_2S is the predominant S(-II) species;

while at pH > 7, HS^- becomes the predominant S(-II) species. FeS precipitation kinetics may be affected as predominant S(-II) species changes caused by pH increase. S(-II) species change may also impact H_2S corrosion.

Second, measure FeS solubility and precipitation kinetics at T ≥ 130 °C, and investigate FeS phase transformation, FeS scale retention, and H_2S corrosion at T > 70 °C, considering that the temperature in oil wells is often ≥ 70 °C. The stability of FeS phase and phase transformation kinetics highly depend on temperature. As literature shows, mackinawite may not be able to form at T > 130 °C, and high temperature can accelerate pyrite formation (Rickard 2007). Our model for FeS prediction should be modified accordingly based on FeS phase stability at high temperature. Also, H_2S corrosion may be significantly accelerated by high temperature.

Third, study FeS in more complex water solutions and flow conditions. The composition of industry water (e.g. oil and gas produced water) is often complicated, typically including calcium (Ca^{2+}), magnesium (Mg^{2+}), carbonate (CO_3^{2-} and HCO_3^-), and even oil emulsions. These inorganics and organics may significantly affect FeS solubility, phase transformation, and H_2S corrosion. For examples, FeS is soluble in oil phase, and aldehydic carbonyls can inhibit mackinawite transformation to pyrite (Rickard 2001). Furthermore, the flow condition in this study is laminar, and turbulence flow may affect FeS precipitation kinetics, FeS scale retention, and H_2S corrosion.

Fourth, test the effects of the used FeS dispersant and other potential FeS inhibitors or dispersants on FeS solubility, precipitation kinetics, phase transformation, and scale retention. It would be of great value if a chemical is discovered to be able to inhibit FeS formation or prevent iron monosulfide transformation to hardly dissolvable pyrite. For future application of potential

chemicals in the oilfield, experimental conditions should be adjusted to oilfield conditions, such as high T, high IS, pH range of 6 – 8, and even the presence of oil phase.

Chapter 6. Reference

Al-Farawati, R. and van den Berg, C. M. 1999. Metal–sulfide complexation in seawater. *Marine Chemistry* **63**(3): 331-352.

Allison, J. B., David; Novo-Gradac, Kevin 1991. MINTEQA2/PRODEFA2, a geochemical assessment model for environmental systems: version 3.0 user's manual. United States Environmental Protection Agency, United States Environmental Protection Agency.

Arntz, D., Höpp, M., Jacobi, S., Sauer, J., Ohara, T., Sato, T., Shimizu, N., Prescher, G., Schwind, H. and Weiberg, O. 2012. Acrolein and methacrolein. *Ullmann's encyclopedia of industrial chemistry*.

Bågander, L. E. and Carman, R. 1994. In situ determination of the apparent solubility product of amorphous iron sulphide. *Applied geochemistry* **9**(4): 379-386.

Bai, P., Zhao, H., Zheng, S. and Chen, C. 2015. Initiation and developmental stages of steel corrosion in wet H_2S environments. *Corrosion Science* **93**: 109-119.

Bai, P., Zhao, H., Zheng, S. and Chen, C. 2015. Initiation and developmental stages of steel corrosion in wet H 2 S environments. *Corrosion Science* **93**: 109-119.

Bai, P., Zheng, S., Chen, C. and Zhao, H. 2014. Investigation of the iron–sulfide phase transformation in nanoscale. *Crystal Growth & Design* **14**(9): 4295-4302.

Benjamin, M. M. 2014. *Water chemistry*: Waveland Press.

Benning, L. G., Wilkin, R. T. and Barnes, H. 2000. Reaction pathways in the Fe–S system below 100 C. *Chemical Geology* **167**(1): 25-51.

Berner, R. A. 1967. Thermodynamic stability of sedimentary iron sulfides. *American Journal of Science* **265**(9): 773-785.

Bhandari, N., Kan, A., Ruan, G., Liu, Y., Zhang, F., Yan, F., Alsaiari, H., Zhang, Z., Dai, Z. and Lu, Y. 2016. Iron Sulfide Scale Control: A Novel Chemical for Growth Inhibition and Dispersion. SPE International Oilfield Scale Conference and Exhibition.

Bischoff, J. L. 1968. Kinetics of calcite nucleation: magnesium ion inhibition and ionic strength catalysis. *Journal of Geophysical Research* **73**(10): 3315-3322.

Bolarinwa, S. O., Leal, J., Ali, A.-B., Sadiq, M., Kharrat, W. and Kovalenko, K. 2012. Innovative Integrated Procedure for Scale Removal in Khuff Gas Wells in Saudi Arabia. SPE International Conference on Oilfield Scale.

Bronsted, J. 1928. Acid and Basic Catalysis. *Chemical Reviews* **5**(3): 231-338.

Butler, I. B., Böttcher, M. E., Rickard, D. and Oldroyd, A. 2004. Sulfur isotope partitioning during experimental formation of pyrite via the polysulfide and hydrogen sulfide pathways: implications for the interpretation of sedimentary and hydrothermal pyrite isotope records. *Earth and Planetary Science Letters* **228**(3): 495-509.

Canfield, D. E., Thamdrup, B. and Fleischer, S. 1998. Isotope fractionation and sulfur metabolism by pure and enrichment cultures of elemental sulfur-disproportionating bacteria. *Limnology and Oceanography* **43**(2): 253-264.

Criaud, A. and Fouillac, C. 1989. Sulfide scaling in low enthalpy geothermal environments: A survey. *Geothermics* **18**(1-2): 73-81.

Csákberényi-Malasics, D., Rodriguez-Blanco, J. D., Kis, V. K., Rečnik, A., Benning, L. G. and Pósfai, M. 2012. Structural properties and transformations of precipitated FeS. *Chemical Geology* **294**: 249-258.

Dai, Z., Kan, A. T., Shi, W., Zhang, N., Zhang, F., Yan, F., Bhandari, N., Zhang, Z., Liu, Y. and Ruan, G. 2017. Solubility Measurements and Predictions of Gypsum, Anhydrite, and Calcite Over Wide Ranges of Temperature, Pressure, and Ionic Strength with Mixed Electrolytes. *Rock Mechanics and Rock Engineering*: 1-13.

Dai, Z., Kan, A. T., Zhang, F., Yan, F., Ruan, G., Bhandari, N., Zhang, Z., Liu, Y., Al-Saiari, H. A. and Tomson, M. B. 2016. A Thermodynamic Model for The Solution Density and Mineral Solubility Predictions up to 250° C, 1,500 Bars for Na-K-Mg-Ca-Ba-Sr-Cl-CO 3-HCO 3-SO 4-CO 2 aq Systems. SPE International Oilfield Scale Conference and Exhibition.

Database, M. (2016). "Public database of mineral information http://www.mindat.org/."

Davison, W. 1991. The solubility of iron sulphides in synthetic and natural waters at ambient temperature. *Aquatic Sciences* **53**(4): 309-329.

Davison, W., Phillips, N. and Tabner, B. J. 1999. Soluble iron sulfide species in natural waters: reappraisal of their stoichiometry and stability constants. *Aquatic Sciences* **61**(1): 23-43.

Dekkers, M. J., Passier, H. F. and Schoonen, M. A. 2000. Magnetic properties of hydrothermally synthesized greigite (Fe3S4)—II. High-and low-temperature characteristics. *Geophysical Journal International* **141**(3): 809-819.

Dougherty, J. A. 2004. Aggressive agents as corrosion inhibitors in gas and oil production. CORROSION 2004, New Orleans, Louisiana, 28 March-1 April. NACE-04423.

Fogler, H. S. 2008. Diffusion and Reaction. In *Elements of chemical reaction engineering*. Chapter 12, New Jersey, Prentice-Hall
Hach, C. 2002. Water analysis handbook. *Loveland, Colorado, USA*: 61-62.
He, S., Oddo, J. E. and Tomson, M. B. 1995a. The nucleation kinetics of barium sulfate in NaCl solutions up to 6 m and 90 C. *Journal of colloid and interface science* **174**(2): 319-326.
He, S., Oddo, J. E. and Tomson, M. B. 1995b. The Nucleation kinetics of strontium sulfate in NaCl solutions up to 6 m and 90 C with or without inhibitors. *Journal of colloid and interface science* **174**(2): 327-335.
Heinrich, C. and Seward, T. 1990. A spectrophotometric study of aqueous iron (II) chloride complexing from 25 to 200 C. *Geochimica et Cosmochimica Acta* **54**(8): 2207-2221.
Hunger, S. and Benning, L. G. 2007. Greigite: a true intermediate on the polysulfide pathway to pyrite. *Geochemical transactions* **8**(1): 1.
HydroGeoLogic, I. A. G. C., Inc 1998. MINTEQA2 / PRODEFA2, A Geochemical Assessment Model for Environmental. United States Environmental Protection Agency, United States Environmental Protection Agency.
Jeong, H. Y., Lee, J. H. and Hayes, K. F. 2008. Characterization of synthetic nanocrystalline mackinawite: crystal structure, particle size, and specific surface area. *Geochimica et Cosmochimica Acta* **72**(2): 493-505.
Kelland, M. A. 2014. *Production chemicals for the oil and gas industry*, Second Edition. New York: CRC press.
Kharaka, Y. K., Gunter, W. D., Aggarwal, P. K., Perkins, E. H. and DeBraal, J. D. 1988. SOLMINEQ. 88: A computer program for geochemical modeling of water-rock interactions. *US geological survey water-resources investigation report* **88**: 4227.
Kocabag, D., Shergold, H. and Kelsall, G. 1990. Natural oleophilicity/hydrophobicity of sulphide minerals, II. Pyrite. *International Journal of Mineral Processing* **29**(3): 211-219.
Langmuir, D. 1997. *Aqueous Environmental Geochemistry*: Prentice Hall.
Lemire, R. J., Berner, U., Musikas, C., Palmer, D. A., Taylor, P., Tochiyama, O. and Perrone, J. 2013. Chemical thermodynamics of iron-Part 1-Chemical thermodynamics volume 13a, Data Bank.
Lind, C., Gates, S. D., Pedoussaut, N. M. and Baiz, T. I. 2010. Novel materials through non-hydrolytic sol-gel processing: Negative thermal expansion oxides and beyond. *Materials* **3**(4): 2567-2587.
Luther, G. W., Rickard, D. T., Theberge, S. and Olroyd, A. 1996. Determination of metal (bi) sulfide stability constants of Mn2+, Fe2+, Co2+, Ni2+, Cu2+, and Zn2+ by voltammetric methods. *Environmental Science & Technology* **30**(2): 671-679.
Luther III, G. W. and Ferdelman, T. G. 1993. Voltammetric characterization of iron (II) sulfide complexes in laboratory solutions and in marine waters and porewaters. *Environmental Science & Technology* **27**(6): 1154-1163.
Ma, H., Cheng, X., Li, G., Chen, S., Quan, Z., Zhao, S. and Niu, L. 2000. The influence of hydrogen sulfide on corrosion of iron under different conditions. *Corrosion Science* **42**(10): 1669-1683.
Menzel, D. 1973. A New Weighting Material for Drilling Fluids Based on Synthetic Iron Oxide. Fall Meeting of the Society of Petroleum Engineers of AIME.
Mineralogy. (2016). "Mineralogy Database http://www.webmineral.com/."
Moog, H. C., Hagemann, S. and Rumyantsev, A. V. 2004. Isopiestic Investigation of the Systems FeCl2–(Na, K, Mg, Ca) Cln–H2O at 298.15 K. *Zeitschrift für Physikalische Chemie/International journal of research in physical chemistry and chemical physics* **218**(9/2004): 1063-1087.
Morse, J. W., Millero, F. J., Cornwell, J. C. and Rickard, D. 1987. The chemistry of the hydrogen sulfide and iron sulfide systems in natural waters. *Earth-Science Reviews* **24**(1): 1-42.
Müller, C., Usbeck, R. and Miesner, F. 2016. Temperatures in shallow marine sediments: Influence of thermal properties, seasonal forcing, and man-made heat sources. *Applied Thermal Engineering* **108**: 20-29.
Mullin, J. W. 2001. *Crystallization*: Butterworth-Heinemann.
Murowchick, J. B. and Barnes, H. 1986. Formation of cubic FeS. *American Mineralogist* **71**(9-10): 1243-1246.
Nasr-El-Din, H. and Al-Humaidan, A. 2001. Iron sulfide scale: formation, removal and prevention. International Symposium on Oilfield Scale.
Nasr-El-Din, H., Rosser, H. and Al-Jawfi, M. 2000. Formation damage resulting from biocide/corrosion inhibitor squeeze treatments. SPE International Symposium on Formation Damage Control.
Naumov, G. B., Ryzhenko, B. N. and Khodakovsky, I. 1974. Handbook of thermodynamic data. *Transl. into ENGLISH of the publ."" Handbook of Thermodyanic Data" Moscow, Atomizdat., 1971*.
Nordstrom, D. K., Plummer, L. N., Langmuir, D., Busenberg, E., May, H. M., Jones, B. F. and Parkhurst, D. L. 1990. Revised chemical equilibrium data for major water-mineral reactions and their limitations. ACS symposium series.

Nordsveen, M., Nešic, S., Nyborg, R. and Stangeland, A. 2003. A mechanistic model for carbon dioxide corrosion of mild steel in the presence of protective iron carbonate films-Part 1: Theory and verification. *Corrosion* **59**(5): 443-456.
Ohfuji, H. and Rickard, D. 2006. High resolution transmission electron microscopic study of synthetic nanocrystalline mackinawite. *Earth and Planetary Science Letters* **241**(1): 227-233.
Olshanskii, Y. I. and Ivanenko, V. 1958. Mechanism of mass transfer in the formation of hydrothermal deposits of sulphides. *Tr. Inst. Geol. rudn. Mestorosh* **16**: 14-46.
OSHA. (2005). "Hydrogen Sulfide Health Hazards https://www.osha.gov/SLTC/hydrogensulfide/hazards.html."
Ramachandran, S., Al-Muntasheri, G., Leal, J. and Wang, Q. 2015. Corrosion and Scale Formation in High Temperature Sour Gas Wells: Chemistry and Field Practice. SPE International Symposium on Oilfield Chemistry.
Ray, J. D., Randall, B. and Parker, J. 1979. Use of reactive iron oxide to remove H2S from drilling fluid. *Journal of Petroleum Technology* **31**(06): 797-801.
Rickard, D. 1995. Kinetics of FeS precipitation: Part 1. Competing reaction mechanisms. *Geochimica et Cosmochimica Acta* **59**(21): 4367-4379.
Rickard, D. 2006. The solubility of FeS. *Geochimica et Cosmochimica Acta* **70**(23): 5779-5789.
Rickard, D., Butler, I. B. and Oldroyd, A. 2001. A novel iron sulphide mineral switch and its implications for Earth and planetary science. *Earth and Planetary Science Letters* **189**(1): 85-91.
Rickard, D., Griffith, A., Oldroyd, A., Butler, I., Lopez-Capel, E., Manning, D. and Apperley, D. 2006. The composition of nanoparticulate mackinawite, tetragonal iron (II) monosulfide. *Chemical Geology* **235**(3): 286-298.
Rickard, D., Grimes, S., Butler, I., Oldroyd, A. and Davies, K. L. 2007. Botanical constraints on pyrite formation. *Chemical Geology* **236**(3): 228-246.
Rickard, D. and Luther, G. W. 2007. Chemistry of iron sulfides. *Chemical reviews* **107**(2): 514-562.
Rickard, D. T. 1969. *The chemistry of iron sulphide formation at low temperatures*: Almgrist & Wiksell.
Rickard, D. T. 1975. Kinetics and mechanism of pyrite formation at low temperatures. *Am. J. Sci* **275**(6): 636-652.
RP, N. S. 2005. Preparation, installation, analysis, and interpretation of corrosion coupons in oilfield operations. *Houston, TX: NACE International*.
Salma, T. 2000. Cost effective removal of iron sulfide and hydrogen sulfide from water using acrolein. SPE Permian Basin Oil and Gas Recovery Conference.
Schieman, S. R. 1999. Solids-free H2S scavenger improves performance and operational flexibility. SPE international symposium on oilfield chemistry.
Schoonen, M. and Barnes, H. 1991. Reactions forming pyrite and marcasite from solution: I. Nucleation of FeS 2 below 100 C. *Geochimica et Cosmochimica Acta* **55**(6): 1495-1504.
Shoesmith, D. W. 1983. Formation, transformation and dissolution of phases formed on surfaces, Atomic Energy of Canada Ltd.
Shoesmith, D. W., Taylor, P., Bailey, M. G. and Owen, D. G. 1980. The formation of ferrous monosulfide polymorphs during the corrosion of iron by aqueous hydrogen sulfide at 21 C. *Journal of the Electrochemical Society* **127**(5): 1007-1015.
Smith, J. K., Wahus, D., Boyd, G. D., Fu, Q., Boyce, G., Firouzkouhi, F. and Deichert, D. 2010. Control and Removal of Downhole Interfacial Solids. SPE International Conference on Oilfield Scale.
Smith, S. N., Brown, B. and Sun, W. 2011. Corrosion at higher H2S concentrations and moderate temperatures. Corrosion Conference and Exposition, Houston, TX, 13 - 17 March. Paper No. 11081.
Smith, S. N., Brown, B. and Sun, W. 2011. Corrosion at higher H2S concentrations and moderate temperatures. NACE International 2011 Corrosion Conference & Expo.
Smith, S. N. and Joosten, M. W. 2006. Corrosion of carbon steel by H2S in CO2 containing oilfield environments. CORROSION 2006, San Diego, California, 12-16 March. NACE-06115.
Standard, A. 2004. Standard practice for preparing, cleaning, and evaluating corrosion test specimens. *American Society for Testing and Materials G1-03*.
Stumm, W. and Morgan, J. J. 1995. *Aquatic chemistry: chemical equilibria and rates in natural waters*: John Wiley & Sons.
Su, Y., Cheng, K. and Jean, Y. 1997. Amplified potentiometric determination of pK 00, pK 0, pK l, and pK 2 of hydrogen sulfides with Ag 2 S ISE. *Talanta* **44**(10): 1757-1763.
Suleimenov, O. and Krupp, R. 1994. Solubility of hydrogen sulfide in pure water and in NaCl solutions, from 20 to 320 C and at saturation pressures. *Geochimica et Cosmochimica Acta* **58**(11): 2433-2444.
Sumestry, M. and Tedjawidjaja, H. 2012. Case Study: Calcium Carbonate Scale Inhibitor Performance Degradation due to H2S Scavenger Injection in Semoga Field. North Africa Technical Conference and Exhibition.

Sun, W. 2006. Kinetics of iron carbonate and iron sulfide scale formation in CO2/H2S corrosion. Ph.D. Thesis, Ohio University.
Sun, W., Nešic, S., Young, D. and Woollam, R. C. 2008. Equilibrium expressions related to the solubility of the sour corrosion product mackinawite. *Industrial & Engineering Chemistry Research* **47**(5): 1738-1742.
Talbot, R. E., Larsen, J. and Sanders, P. F. 2000. Experience With the Use of Tetrakishydroxymethylphosphonium Sulfate (THPS) for the Control of Downhole Hydrogen Sulfide. CORROSION 2000.
USGS, P. (1999). "Frequently Asked Questions for PHREEQC and PhreeqcI. https://wwwbrr.cr.usgs.gov/projects/GWC_coupled/phreeqc/faq.html."
Vaughan, D. and Ridout, M. 1970. Mössbauer study of pyrrhotite. *Solid State Communications* **8**(24): 2165-2167.
Wang, Q., Ajwad, H., Shafai, T. and Lynn, J. D. 2013. Iron Sulfide Scale Dissolvers: How Effective Are They? SPE Saudi Arabia Section Technical Symposium and Exhibition, Al-Khobar, Saudi Arabia, 19-22 May. SPE-168063-MS. http://dx.doi.org/10.2118/168063-MS.
Webb, E. D., Schultz, R. L., Howard, R. G. and Tucker, J. C. 2006. Next generation fluidic oscillator. SPE/ICoTA Coiled Tubing Conference & Exhibition.
Wei, D. and Osseo-Asare, K. 1995. Formation of iron monosulfide: a spectrophotometric study of the reaction between ferrous and sulfide ions in aqueous solutions. *Journal of colloid and interface science* **174**(2): 273-282.
Weiss, R. 1970. The solubility of nitrogen, oxygen and argon in water and seawater. Deep Sea Research and Oceanographic Abstracts.
Wylde, J. J. 2014. Sulfide scale control in produced water handling and injection systems: Best practices and global experience overview. SPE International Oilfield Scale Conference and Exhibition, Aberdeen, Scotland, 14-15 May. SPE-169776-MS. http://dx.doi.org/10.2118/169776-MS.
Yagil, G. 1967. Effect of ionic hydration in equilibria and rates in concentrated electrolyte solutions. III. The H- scale in concentrated hydroxide solutions. *The Journal of Physical Chemistry* **71**(4): 1034-1044.
Yamaguchi, S. and Wada, H. 1972. Aging of colloidal iron sulfide. *Journal of colloid and interface science* **40**(3): 477-478.
Zhang, J.-Z. and Millero, F. J. 1994. Investigation of metal sulfide complexes in sea water using cathodic stripping square wave voltammetry. *Analytica Chimica Acta* **284**(3): 497-504.

Curriculum Vitae

Ya LIU, EIT

6100 Main St. MS-519, Houston, TX. 77005. (713)647-1090. yaliu2012@gmail.com.

EDUCATION

Rice University, Houston, TX. (GPA: 3.7 / 4.0)

Ph.D. in Civil and Environmental Engineering — Expected 05/2017

M.S. in Civil and Environmental Engineering — 05/2014

Nankai University, Tianjin, China. (GPA: 3.6 / 4.0)

B.S. in Environmental Engineering — 06/2012

WORK EXPERIMENCE

Seismic Image Analyst, CGG — Start at 05/30/2017

RESEARCH and TEACHING EXPERIENCE

Research Assistant, Rice University — 08/2012 – Present

1. Iron Sulfide (FeS) Precipitation Kinetics, Solubility, Phase Transformation, Corrosion and Scale Retention
   - Designed and built a convenient and reliable anoxic plug flow reactor for this study.
   - Measured FeS solubility, precipitation kinetics, phase transformation, H2S corrosion, and FeS scale retention under different operation and solution conditions (e.g. temperature, ionic strength, and iron to sulfide concentration ratio).
   - Developed a FeS solubility and precipitation risk model.
   - Discovered chemicals that prevents FeS accumulation on pipeline for cost effective FeS scale control.
   - Presented this work on Rice University *Brine Chemistry Consortium* conference to 25 member companies in the oil industry in Dec 2016, and on *SPE International Conference on Oilfield Chemistry* in Apr 2017.

2. A Novel Method for Mineral Scale Inhibitor Detection in the Oil and Gas Produced Water
   - Invented a cost-effective method for various commercial scale inhibitor detection and validated it with oil field water samples; Developed a VBA program to provide full guidance and calculation for the method.
   - Invited to demonstrate this method to BWA Water Additives Company, UK. The VBA program is adopted by BWA company.
   - Presented this work on Rice University *Brine Chemistry Consortium* conference in Dec 2013, and on the *SPE International Oilfield Scale Conference and Exhibition* in May 2014.

Teaching Assistant, Rice University — Each fall semester of 2013 - 2016

- Led, organized and taught Environmental Chemistry Lab course attended by over 30 students.
- Provided one-on-one tutoring and graded assignments in Environmental Chemistry course.

Undergraduate Research Assistant, Nankai University — 02/2010 – 03/2012

1. Spearheaded and collaborated with 4 teammates on research project of biochar's effect on crop growth and production, and published three highly cited journal papers as a coauthor.
2. Studied the exposure routes of Chinese residents to perflurionated compounds and the associated health risks at different regions of China, and published a highly cited journal paper as a coauthor.

AWARDS

First Place in student paper contest in Chinese America Petroleum Association (CAPA) technical symposium in Sep 2014.
Second Class Award in National University Student Innovation Program in Mar 2012.
Merit Student Award in both Sep 2009 and Sep 2010.

REFEREED JOURNAL PAPERS

Liu, Y., Kan, A., Zhang, Z., Yan, C., Yan, F., Zhang, F., Bhandari, N., Dai, Z., Ruan, G., Wang, L., Greenberg, J., Tomson, M.B. 2016. An assay method to determine mineral scale inhibitor efficiency in produced water. [J] *Journal of Petroleum Science and Engineering.* 143: 103-112.

Liu, Y., Zhang, Z., Bhandari, N., Dai, Z., Yan, F., Ruan, G., Lu, A., Deng, G., Kan, A., Tomson, M.B. 2017. A new approach to study iron sulfide precipitation kinetics, solubility and phase transformation. (submitted)

Yan, F., Dai, Z., Ruan, G., Alsaiari, H., Bhandari, N., Zhang, F., **Liu, Y.**, Zhang, Z., Kan, A. and Tomson, M., 2016. Barite scale formation and inhibition in laminar and turbulent flow: a rotating cylinder approach. [J] *Journal of Petroleum Science and Engineering* (Available online).

Zhang, F., Dai, Z., Yan, C., Bhandari, N., Yan, F., **Liu, Y.**, Zhang, Z., Ruan, G., Kan, A. T. and Tomson, M. B. 2016. Barite-scaling risk and inhibition at high temperature. [J] *SPE Journal*. 1086-055X.

Bhandari, N., Kan, A., Zhang, F., Dai, Z., Yan, F., Ruan, G., Zhang, Z., **Liu, Y.**, Eldik, R.V. and Tomson, M.B. 2016. Mineral precipitation kinetics: assessing the effect of hydrostatic pressure and its implication on the nucleation mechanism. [J] *Crystal Growth & Design.* 16(9): 4846-4854.

Yan, C., Kan, A., Zhang, F., **Liu, Y.**, Tomson, R. C., Tomson, M.B. 2015. Systematic study of barite nucleation and inhibition with various polymeric scale inhibitors by novel laser apparatus. [J] *SPE Journal*. 20(03), 642-651.

Yan, F., Zhang, F., Bhandari, N., Wang, L., Dai, Z., Zhang, Z., **Liu, Y.**, Ruan, G., Kan, A., Tomson, M.B. 2015. Adsorption and precipitation of scale inhibitors on shale formations. [J] *Journal of Petroleum Science and Engineering*. 136: 32-40. 0920-4105.

Yan, F., Chu, Y., Zhang, K., Zhang, F., Bhandari, N., Ruan, G., Dai, Z., **Liu, Y.**, Zhang, Z., Kan, A., Tomson, M.B. 2015. Determination of adsorption isotherm parameters with correlated errors by measurement error models. [J] *Chemical Engineering Journal.* 281, 921-930.

Zhang, F., Dai, Z., Yan, F., Ruan, G., Bhandari, N., Zhang, Z., **Liu, Y.**, Kan, A. and Tomson, M.B. 2017. Acid/base and metal complex solution chemistry of sulfonated polyacrylate copolymer versus temperature and ionic strength. [J] *Applied Geochemistry.* 76, pp.1-8.

Dai, Z., Kan, A., Shi, W., Zhang, N., Zhang, F., Yan, F., Bhandari, N., Zhang, Z., **Liu, Y.**, Ruan, G. and Tomson, M.B. 2017. Solubility measurements and predictions of gypsum, anhydrite, and calcite over wide ranges of temperature, pressure, and ionic strength with mixed electrolytes. [J] *Rock Mechanics and Rock Engineering* (Available online).

Li, L.; **Liu, Y.**; Lu, Y.; Liang Z.; Zhang, P.; Sun, H. 2011. Review on Environmental Effects and Applications of Biochar [J]. *Environmental Chemistry* (in Chinese). 30(8): 1411-1421.

Li, L., Lu, Y., **Liu, Y.**, Sun, H., Liang, Z. 2012. Adsorption mechanisms of cadmium(ii) on biochars derived from corn straw. *Journal of Agro-Environmental Science* (in Chinese). 31(11): 2277-2283.

Zhang, P., Wu, J., Li, L., **Liu, Y.**, Sun, H., Sun, T. 2012. Sorption and catalytic hydrolysis of carbaryl on pig-manure-derived biochars. *Journal of Agro-Environmental Science* (in Chinese). 31(2): 416-421

Zhang, T., Sun, H., Lin, Y., Wang, L., Zhang, X., **Liu, Y.**, Geng, X., Zhao, L., Li, F. and Kannan, K. 2011. Perfluorinated compounds in human blood, water, edible freshwater fish, and seafood in China: daily intake and regional differences in human exposures [J]. *J. Agric. Food. Chem.* 59(20): 11168-11176. 0021-8561.

REFEREED CONFERENCE PAPPERS

Liu, Y., Zhang, Z., Bhandari, N., Yan, F., Zhang, F., Dai, Z., Ruan, R., Alsaiari, H.A., Lu, Y., Deng, G., Kan, A., Tomson, M.B. 2017. Iron Sulfide Precipitation and Deposition under Different Impact Factors. *SPE International Conference on Oilfield Chemistry,* 3-5 April, Montgomery, Texas, USA. SPE-184546.

Liu, Y., Kan, A. T., Yan, C., Wang, F., Wang, L. and Tomson, M. B. 2014. An assay method for the detection of all scale inhibitors at extremely low concentration. *SPE International Oilfield Scale Conference and Exhibition*, 14-15 May, Aberdeen, Scotland, UK. SPE-169762.

Bhandari, N., Ruan, G. **Liu, Y.**, Zhang, F., Yan, F., Saiari, H.A., Zhang, Z., Dai, Z., Lu, Y., Deng, G., Kan, A., Tomson, M.B. 2017. Identification of New Chemical Formulation for Control of Metal Sulfides (FeS, ZnS and PbS) Scale Deposition. *SPE International Conference on Oilfield Chemistry*, 3-5 April, Montgomery, Texas, USA. SPE-184526.

Dai, Z., Zhang, F., Yan, F., Ruan, G., Bhandari, N., **Liu, Y.**, Zhang, Z., Alsaiari, H., Lu, Y., Deng G., Kan, A., Tomson, M. 2017. A new theoretical model for the induction time and scale inhibitor dosage predictions for calcite and barite over wide ranges of temperature, inhibition concentration and saturation index. *SPE International Conference on Oilfield Chemistry*, 3-5 April, Montgomery, Texas, USA. SPE-184547.

Kan, A., Garcia, M., Dai., Z., Tatavalli, N., Frech, R., **Liu, Y.**, Lu, Y., Bhandari, N., Vargas, F., Tomson, M.B. 2017. Modeling H_2S in deep water production. *SPE International Conference on Oilfield Chemistry*, 3-5 April, Montgomery, Texas, USA. SPE-184517.

Yan, F., Bhandari, N., Ruan, G., Alsaiari, H., Dai, Z., **Liu, Y.**, Zhang, Z., Lu, Y., Deng G., Kan, A., Tomson, M. 2017. The Effect Of Turbulence On Mineral Scale Control In Oilfield. *SPE International Conference on Oilfield Chemistry*, 3-5 April, Montgomery, Texas, USA. SPE-184524.

Ruan, G., Kan, A., Dai, Z., Yan, F., Zhang, F., Bhandari, N., Alsaiari, H., **Liu, Y.**, Zhang, Z., Lu, Y., Deng G., Tomson, M. 2017. Fast and Accurate Screening and Evaluation of Halite Scale Inhibitors by Two Novel Static Bottle Testing Methods. *SPE International Conference on Oilfield Chemistry,* 3-5 April, Montgomery, Texas, USA. SPE-184593.

Zhang, Z., **Liu, Y.**, Dai, Z., Bhandari, N., Zhang, F., Yan, F., Ruan, G., et al. 2016. Impact of FeIII/FeII on scale inhibition. *SPE International Oilfield Scale Conference and Exhibition,* 11-12 May, Aberdeen, Scotland, UK. SPE-179905.

Bhandari, N., Kan, A., Ruan, G., **Liu, Y.**, Zhang, F., Yan, F. et al. 2016. Iron sulfide scale control: a novel chemical for growth inhibition and dispersion. *SPE International Oilfield Scale Conference and Exhibition*, 11-12 May, Aberdeen, Scotland, UK. SPE-179872.

Yan, F., Bhandari, N., Zhang, F., Ruan, G., Dai, Z., **Liu, Y.**, Zhang, Z., Alsaiari, H., Kan, A. and Tomson, M. 2016. Scale formation and control under turbulent conditions. *SPE International Oilfield Scale Conference and Exhibition*, 11-12 May, Aberdeen, Scotland, UK. SPE-179863.

Zhang, F., Wang, W., Kan, A. T., Hinrichsen, C. J., Wei, W., Dai, Z., **Liu, Y.**, Yan, F., et al. 2016. Calcium sulfate scale formation and inhibitor selection for a steamflood project. *CORROSION* 2016. NACE-2016-7848.

Dai, Z., Kan, A., Zhang, F., Yan, F., Ruan, G., Bhandari, N., Zhang, Z., **Liu, Y.**, Al-Saiari, H.A. and Tomson, M.B. 2016, May. A thermodynamic model for the solution density and mineral solubility predictions up to 250° C, 1,500 Bars for Na-K-Mg-Ca-Ba-Sr-Cl-CO_3-HCO_3-SO_4-CO_2 aq systems. *SPE International Oilfield Scale Conference and Exhibition*, 11-12 May, Aberdeen, Scotland, UK. SPE-179892.

Zhang, F., Hinrichsen, C.J., Kan, A., Wang, W., Wei, W., Dai, Z., Yan, F., **Liu, Y.**, Bhandari, N., Zhang, Z., Ruan, G., Tomson, M.B. 2016. Calcium sulfate scaling risk and inhibition for a steamflood project. *SPE International Oilfield Scale Conference and Exhibition*, 11-12 May, Aberdeen, Scotland, UK. SPE-179875.

Ruan, G., Kan, A., Yan, F., Zhang, F., Bhandari, N., Alsaiari, H.A., Dai, Z., **Liu, Y.**, Zhang, Z., Tomson, M.B. 2016. Citrate assisted metal phosphonate colloidal scale inhibitors for long-term squeeze treatments. *SPE International Oilfield Scale Conference and Exhibition*, 11-12 May, Aberdeen, Scotland, UK. SPE-179898.

Bhandari, N., Kan, A., Dai, Z., Zhang, F., Yan, F., Ruan, G.G., Alsaiari, H.A., Zhang, Z., **Liu, Y.**, Lu, Y., Deng, G., Tomson, M.B. 2016. Effect of hydrodynamic pressure on mineral precipitation kinetics and scaling risk at HPHT. *SPE International Oilfield Scale Conference and Exhibition*, 11-12 May, Aberdeen, Scotland, UK. SPE-179873.

Alsaiari, H.A., Al-Khaldi, M., Al-Taie, I., Wang, Q., Alabedi, G., Zhang, F., Zhang, Z., Bhandari, N., Ruan, G., Yan, F., **Liu, Y.**, Kan, A. Tomson, M.B. 2016. Effect of crosslinkers on the performance of calcium sulfate scale inhibitors at high temperature: impact of zirconium. *SPE International Oilfield Scale Conference and Exhibition*, 11-12 May, Aberdeen, Scotland, UK. SPE-179878.

Yan, F., Zhang, F., Bhandari, N., **Liu, Y.**, Wang, L., Dai, Z., et al. 2015. Interaction between scale inhibitors and shale and sandstone formations. *SPE International Symposium on Oilfield Chemistry*, 13-15 April, The Woodlands, Texas, USA. SPE-173769.

Bhandari, N., Kan, A.T., Zhang, F., Dai, Z., Yan, F., **Liu, Y.**, Zhang, Z., Bolanos, V., et al. 2015. The effect of pressure and TDS on barite scaling kinetics. *SPE International Symposium on Oilfield Chemistry*, 13-15 April, The Woodlands, Texas, USA. SPE-173790.

Zhang, Z., Zhang, F., Wang, Q. L., Bhandari, N., Yan, F., **Liu, Y.**, Dai, Z., et al. 2015. Ferrous iron impact on phosphonate and polymeric scale inhibitors at temperature ranging from 25 to 70 ^{0}C. *SPE International Symposium on Oilfield Chemistry*, 13-15 April, The Woodlands, Texas, USA. SPE-173770.

Kan, A., Dai, Z., Zhang, F., Bhandari, N., Yan, F., Zhang, Z., **Liu, Y.**, Tomson, M.B. 2015. Scale prediction and control at ultra HTHP. *SPE International Symposium on Oilfield Chemistry*, 13-15 April, The Woodlands, Texas, USA. SPE-173803.

Yan, C., Kan, A., Zhang, F., **Liu, Y.**, Tomson, R. C., Tomson, M.B. 2014. Systematic study of barite nucleation and inhibition with various polymeric scale inhibitors by novel laser apparatus. *SPE International Oilfield Scale Conference and Exhibition*, 14-15 May, Aberdeen, Scotland, UK. SPE-169787.

Wang, L., Kan, A.T., Zhang, Z., Yan, F., **Liu, Y.,** Dai, Z., Tomson, M. B. 2014. Field method for determination of bicarbonate alkalinity. *SPE International Oilfield Scale Conference and Exhibition*, 14-15 May, Aberdeen, Scotland, UK. SPE-169758.

Yan, F., Kan, A.T., Yan, C., Wang, L., **Liu, Y.**, Tomson, M. B. 2014. Experimental and modeling study on enhancement of squeeze treatment in sandstone by the addition of zinc ion. *SPE International Oilfield Scale Conference and Exhibition*, 14-15 May, Aberdeen, Scotland, UK. SPE-169753.

Paper Citations: 278

Google Scholar link: https://scholar.google.com/citations?user=OcQrxCUAAAAJ&hl=en

PROFESSIONAL AFFILIATIONS

Society of Petroleum Engineering (**SPE**)
National Association of Corrosion Engineers (**NACE**)
Chinese America Petroleum Association (**CAPA**)